CHAPTER 6
TABLES

Note on Qualification Status

"Q-Status" designators in the tables in Appendix D indicate the current Quality Assurance (QA) status of the software or data used in or resulting from analyses or models. Causes for a particular data set being considered as "non-Q" include: (1) some of the input values to the model are derived from literature or other sources that are considered "existing," but unqualified, data; (2) the model used in the generation of the data has not been validated; or (3) the software used in the application of the model has not been qualified. The data, models, and software that are expected to be used in future performance assessments for the site suitability, site recommendation, and license application will be appropriately qualified in accordance with applicable procedures.

INTENTIONALLY LEFT BLANK

Table 6-1. Summary of Waste Form Degradation Models, Radionuclide Mobilization Models, and EBS Transport Models for the TSPA-VA Calculations

Model	Section Reference	Role in TSPA-VA
Waste Form Degradation:		
Cladding Response for Commercial Spent Nuclear Fuel	6.3.1.1	The response of Zircaloy cladding is represented within the TSPA-VA base case as the fraction of SNF fuel exposed as a function of time. The cladding performance includes models for general corrosion, localized corrosion, creep rupture, mechanical failure, and juvenile failure.
- Generalized Corrosion	6.3.1.1.4	WAPDEG was used to calculate the time-dependent generalized corrosion of Zircaloy cladding. The WAPDEG results for generalized corrosion are combined with results for localized corrosion to determine the fraction of exposed fuel (due to corrosion). The RIP input variable CLAD2 represents the fraction of exposed fuel for localized and general corrosion as a function of time. CLAD2 depends, in part, on look-up tables defined within the RIP input deck for the upper and lower bounds of cladding failures due to corrosion.
- Localized Corrosion	6.3.1.1.4.2	WAPDEG was used to calculate the long term localized corrosion of Zircaloy cladding. The RIP input variable CLAD2 represents the fraction of exposed fuel for both localized and general corrosion as a function of time. CLAD2 depends on look-up tables, as noted above.
- Creep Rupture	6.3.1.1.5	Creep rupture is modeled external to RIP and combined with stainless steel cladding failures in the source term definition for each commercial spent fuel region (denoted as SF1 through SF6 in the RIP input deck). Note that creep rupture/stainless steel cladding failure is defined as a constant fraction (0.0125) and occurs concurrently with waste package failure. Failures due to corrosion and mechanical response occur after waste package failure.
- Hydride Failures	6.3.1.1.6	Cladding failure from hydride embrittlement, delayed hydride cracking and hydrite reorientation are not expected to occur at repository conditions. These failure mechanisms are therefore not included in the TSPA-VA model.
- Mechanical Failures	6.3.1.1.7	Mechanical failure of Zircaloy is modeled external to RIP to determine the fraction of fuel expos ed as a function of time. The RIP input variable CLAD1 represents the fraction of exposed fuel for mechanical failures. CLAD1 depends in part on time-dependent look-up tables defined within the RIP input deck for the upper and lower bounds of mechanical failures.
- Stress Corrosion Cracking	6.3.1.1.8	Stress corrosion cracking is not expected to occur at repository conditions. This failure mechanism is therefore not included in the TSPA-VA model.
- Cladding Unzipping	6.3.1.1.9 & 6.3.1.2	Clad unzipping driven by fuel oxidation is unlikely to occur given the long time to failure of the waste packages. This cladding failure mechanism is therefore not included in the RIP base case analyses.

Table 6-1. Summary of Waste Form Degradation Models, Radionuclide Mobilization Models, and EBS Transport Models for the TSPA-VA Calculations (Continued)

Model	Section Reference	Role in TSPA-VA
Aqueous Dissolution of Spent Fuel	6.3.1.3	The gap-inventory species (C-14, I-129, Se-79, Tc-99) and their gap fractions are defined through the source term inventory for commercial and DOE spent fuel in the RIP input deck. The forward dissolution rate for spent fuel is based on an empirical fit to rate data as a function of the chemical environment for the base case. This empirical fit is defined as an external function for the RIP input deck.
Dissolution of DOE Spent Fuel	6.3.2.1	The dissolution rate equations for oxide, ceramic and metallic fuel are based on the response of metallic spent fuel because N-Reactor fuel represents the major portion of DOE spent fuel. The dissolution rate for metallic spent fuel is defined by the parameter METDR within the RIP input deck.
Dissolution of Navy Fuel	6.3.2.2	Navy fuel was not included in the base case for the TSPA-VA because the cladding is expected to remain intact. For sensitivity studies, the release rate at the waste package surface was provided as an external function for RIP because of the confidentiality of the Navy fuel.
Dissolution of Pu Disposition Wastes	6.3.2.3	Pu waste forms were not included in the base case for the TSPA-VA analyses but were included in the sensitivity studies.
Dissolution of HLW (Glass)	6.3.3	The forward dissolution rate for vitrified waste (glass) is based directly on an empirical fit to rate data as a function of the chemical environment. This empirical fit is defined as an external function for the RIP input deck.
Radionuclide Mobilization:		
Radionuclide Aqueous Solubility	6.4.1	Solubility for the 9 radionuclides in the TSPA-VA base case model are defined in the RIP input deck. The input variables for solubility parameters and distributions are labeled as "SOLXX" in the RIP input deck, with XX representing the radioisotope. Note that Pu-239 and Pu-242 have the same solubility limit. Up to 39 radionuclides are used for sensitivity analyses.
Colloidal Mobilization	6.4.2	The concentrations of Pu-colloidal particles are defined directly in the RIP input deck through the input parameter CONCOL.
Secondary Phase Formation and Radionuclide Retention	6.4.3	The effects of secondary phase formation and the associated potential for radionuclide retention are not included in the TSPA-VA base case, but are included in a sensitivity calculation by reducing the solubility of Np-237. The experimental and analytical studies presented in this section are preliminary results that may ultimately provide a basis for substantial reduction in aqueous solubility and for substantial increases in radionuclide retention for the License Application. Additional experimental and analytical work is required to develop and verify new models for the LA.
EBS Transport:		
Flow and Transport Through the EBS	6.5	The flow through the EBS is based on UZ flow fields and the waste package degradation model. Retardation parameters are defined as input variables in the RIP input deck. The EBS transport model is directly represented within the RIP input deck, using mixing cells with diffusive and advective pathways. The assumptions, discretization, flow connections, and retardation parameters for this transport model are described in Section 6.5.

Table 6-2. List of Waste Form Issues as Agreed Upon by Participants at Waste Form Degradation and Radionuclide Mobilization Abstraction/Testing Workshop (CRWMS M&O 1997b)

Session I Issues as Ranked	
1.1.1	Inventory of SNF
1.1.2	Distribution of radionuclides
1.2.1	Cladding degradation model
1.2.2	SNF Oxidation model
1.2.3	SNF Dissolution model
1.2.4	Time dependent evolution of solution and alteration layer
1.3	Representation of evolution of the near-field environment
1.4	Representation of data uncertainty/variability
1.5	Exposed SNF surface area
Session II Issues as Ranked	
2.1	Inventory of glass waste
2.2	Distribution of radionuclides
2.3	Canister degradation
2.4	Vapor hydration
2.5	Dissolution rate
2.6	Time dependent evolution of solution and alteration layer
2.7	Evolution of NFE
2.8	Representation of data uncertainty/variability
2.9	Exposed glass waste surface area
Other DOE Fuels Breakout Issues	
2B1	Cladding and Canister Credit
2B2	Evolution of NFE
2B3	Dissolution
Session III Issues as Ranked	
3.1	Physical processes - water contact mode
3.2	Physical processes - transport paths
3.3	Chemical processes - mobilization temp dependence
3.4	Chemical processes - mobilization - solid dependence
3.5	Chemical processes - mobilization - fluid dependence
3.6	Mobilization - Colloids
3.7	EBS transport aqueous through WP (includes corrosion products)
3.8	EBS transport aqueous - through other EBS (invert)
3.9	EBS transport - colloid - through WP (includes corrosion products)
3.10	EBS transport - colloid - through other EBS (invert)

Table 6-3. Final Ranked Scores of Sub-Issues from Waste Form Degradation and Radionuclide Mobilization Abstraction/Testing Workshop (CRWMS M&O 1997b)

#	Sub-Issue	Numerical Score
	SESSION I --Spent Nuclear Fuel	
1.2.3	Dissolution rate (includes issue 2B3)	62
1.2.4	Time dependent evolution of solution and alteration layer	62
1.3	Representation of evolution of the near field	56
1.5	Exposed SNF surface area	48
1.2.1	Cladding degradation model (includes issue 2B1)	46
	Priority Cut-Off Point	
1.4	Representation of data uncertainty/variability	38
1.1.1	Inventory of SNF	36
1.2.2	Oxidation model	34
1.1.2	Distribution of radio nuclides	32
	SESSION II -- DHLW (Glass) and Other Wastes	
2.6	Time dependent evolution of solution and alteration layer	66
2.4	Vapor hydration	60
2.7	Evolution of NFE (includes issue 2B2)	60
2.5	Dissolution rate	56
	Priority Cut-Off Point	
2.1	Inventory of glass waste	36
2.8	Representation of data uncertainty/variability	36
2.9	Exposed glass waste surface area	30
2.3	Canister degradation	26
2.2	Distribution of radionuclides	22
	SESSION III -- Solubilities and EBS Transport	
3.1	Physical processes - water contact mode	64
3.6	Mobilization - Colloids	64
3.5	Chemical processes - mobilization - fluid dependence	62
3.2	Physical processes - transport paths	56
3.4	Chemical processes - mobilization - solid dependence	50
	Priority Cut-Off Point	
3.9	EBS transport - colloid - through WP (includes corrosion products)	48
3.10	EBS transport - colloid - through other EBS (invert)	48
3.7	EBS transport aqueous through WP (includes corrosion products)	44
3.8	EBS transport aqueous - through other EBS (invert)	44
3.3	Chemical processes - mobilization temp dependence	34

Table 6-4. Base-Case Waste Inventory Packaging

	Assemblies/Canisters		Casks			Waste Packages			
	CSNF Assemblies	HLW/DSNF Canisters	CSNF	HLW/ DSNF	Total	DPC*	CSNF	HLW/ DSNF	Total
Baseline	220,290	12,020	11,820	2,860	14,680	3,490	7,760	2,546	10,306

* Dual-Purpose Canister

Table 6-5. DOE SNF in Each Category for the Total and Base Case Inventories

Category	Spent Fuel Type	Representative Fuel	Total Inventory (MTHM)	Base Case[1] Inventory (MTHM)
1	Uranium Metal	N-Reactor	2122.26	1979.88
2	Uranium-Zirconium alloy	Heavy Water Component Test Reactor (HWCTR)	0.04	0.04
3	Uranium-Molybdenum alloy	FERMI (Enrico Fermi Reactor)	3.77	3.51
4	Uranium oxide	Commercial Pressurized Water Reactor (PWR)	98.68	92.06
5	Uranium oxide (disrupted clad)	Three Mile Island (TMI) core debris	87.02	81.18
6	Uranium-Aluminum alloy	Advanced Test Reactor (ATR)	8.74	8.15
7	Uranium silicide	Foreign Research Reactor-Materials Test Reactor (FRR MTR)	11.55	10.78
8	Uranium-Thorium carbide (high integrity)	Fort St. Vrain	24.67	23.01
9	Uranium-Thorium carbide (low integrity)	Peach Bottom	1.66	1.55
10	Uranium and Uranium Plutonium carbide	Fast Flux Test Facility (FFTF) Carbide	0.15	0.14
11	Mixed oxide	Fast Flux Test Facility (FFTF) Oxide	12.32	11.49
12	Uranium-Thorium oxide	Shippingport Light Water Breeder Reactor (LWBR)	49.63	46.30
13	Uranium-Zirconium hydride	Training Research Isotopes-General Atomics (TRIGA)	2.03	1.89
14	Sodium Bonded	FERMI Blanket	NA	NA
15	Navy Fuel	Navy Fuel	63.00	63.00
16	Miscellaneous	FFTF, MURR, RINSC, ORR, N, FERMI, ATR etc.	10.73	10.01
Total			**2496.25**	**2332.99**

[1]Total Inventory reduced by approximately 7 percent, except for Category 15, to obtain the base case inventory of approximately 2,333 MTHM.

Table 6-6. Radionuclide Inventory in Curies per Waste Package (Average)

	Isotope	Half-Life (years)	CSNF Average Activity(Ci)/WP	HLW Average Activity(Ci)/WP	DOE SNF Average Activity(Ci)/WP
1	Ac-227	2.16E+01	1.51E-04	2.64E-03	2.35E-05
2	Am-241	4.32E+02	3.15E+04	9.72E+02	4.04E+02
3	Am-242m	1.52E+02	1.84E+02	9.28E-02	3.56E-01
4	Am-243	7.38E+03	2.14E+02	2.30E-01	8.28E-01
5	C-14	5.73E+03	1.17E+01	0.00E+00	3.10E-01
6	Cl-36	3.01E+05	9.30E-02	0.00E+00	5.67E-04
7	Cm-244	1.81E+01	1.01E+04	5.86E+01	3.43E+01
8	Cm-245	8.50E+03	2.96E+00	2.48E-04	1.40E-02
9	Cm-246	4.73E+03	6.17E-01	2.81E-05	2.36E-03
10	Cs-135	2.30E+06	4.35E+00	8.67E-01	6.60E-02
11	I-129	1.57E+07	2.90E-01	4.17E-05	5.67E-03
12	Nb-93m	1.36E+01	1.54E+01	4.36E+00	2.13E-01
13	Nb-94	2.03E+04	6.88E+00	1.49E-04	6.98E-04
14	Ni-59	8.00E+04	1.98E+01	4.19E-01	2.66E-02
15	Ni-63	9.20E+01	2.60E+03	3.66E+01	2.91E+01
16	Np-237	2.14E+06	3.69E+00	5.34E-01	5.46E-02
17	Pa-231	3.28E+04	2.78E-04	4.28E-03	3.69E-03
18	Pb-210	2.23E+01	5.64E-06	1.28E-07	9.05E-07
19	Pd-107	6.50E+06	1.07E+00	1.24E-01	1.10E-02
20	Pu-238	8.77E+01	2.61E+04	1.82E+03	1.81E+02
21	Pu-239	2.41E+04	2.99E+03	2.43E+01	1.55E+02
22	Pu-240	6.54E+03	4.44E+03	1.54E+01	1.16E+02
23	Pu-241	1.44E+01	2.86E+05	6.31E+02	2.40E+03
24	Pu-242	3.87E+05	1.70E+01	2.00E-02	1.14E-01
25	Ra-226	1.60E+03	2.08E-05	4.47E-07	1.80E-06
26	Ra-228	6.70E+00	2.61E-09	4.61E-04	1.29E-03
27	Se-79	6.50E+04	3.72E+00	2.86E-01	8.85E-02
28	Sm-151	9.00E+01	2.98E+03	2.14E+03	1.68E+02
29	Sn-126	1.00E+05	7.19E+00	1.90E+00	9.48E-02
30	Tc-99	2.13E+05	1.18E+02	2.95E+01	2.55E+00
31	Th-229	7.34E+03	3.06E-06	6.63E-05	5.47E-03
32	Th-230	7.70E+04	3.00E-03	6.01E-05	3.77E-04
33	Th-232	1.41E+10	3.66E-09	4.63E-04	1.01E-03
34	U-233	1.59E+05	5.94E-04	2.62E-03	1.36E+00
35	U-234	2.45E+05	1.12E+01	2.44E-01	4.76E-01
36	U-235	7.04E+08	1.39E-01	8.88E-04	2.59E-02
37	U-236	2.34E+07	2.28E+00	3.20E-03	8.93E-02
38	U-238	4.47E+09	2.56E+00	2.78E-02	2.97E-01
39	Zr-93	1.53E+06	2.01E+01	5.26E+00	5.18E-01

Table 6-7. Composition of Cladding

	Zircaloy - 2	Zircaloy - 4
Tin	1.20 to 1.70%	1.20 to 1.70%
Iron	0.07 to 0.20%	0.18 to 0.24%
Chromium	0.05 to 0.15%	0.07 to 0.13%
Nickel	0.03 to 0.08%	<0.0070 %
Oxygen	0.09 to 0.16%	0.09 to 0.16%

Table 6-8. Design Characteristics of the Assembly (Westinghouse W1717WL, Base Case Fuel Assembly)

Clad OD	0.950 cm	Irradiation time	4.5 yrs
Clad thickness	0.057 cm	Primary pressure	15 MPa
Clad Idqq	0.836 cm	Coolant Tem.	280–330°C
Rod length	384.96 cm	Clad ID Temp.	340–370°C
Active core length	365.76 cm	Burnup	40 MWd/kgU
Plenum length	16.00 cm	Oxide thickness	28 µm
Plenum volume/Pin	8.77 cc	Fission Gas Rel.	6%
Effective gas volume/Pin	13.16 cc	Plenum P.(27°C)	4 MPa
Active fuel volume/Pin	200.61 cc	Stress (27°C)	32 MPa
Initial fill pressure	2.8 MPa	Stress(350°C)	66 MPa
Pins/Assembly	264	Fuel Volume/WP*	1.112 m^3

*21 PWR assemblies/WP

Table 6-9. Cladding Oxide Thickness, Wall Thickness, and Fission Gas Release and Hydrogen Content vs. Burnup**

Fuel Burn-up MWd/kgU	Cladding Oxide Thickness, µm	Clad Thickness *cm	Fission Gas Release Fraction %	Fission Gas Production cc (STP)	Average Hydrogen Content ppm
25	15	0.056	5.34	1373	173
30	16	0.056	5.75	1648	221
35	21	0.055	6.23	1922	273
40	28	0.054	6.80	2200	330
45	38	0.053	7.45	2470	391
50	51	0.052	8.17	2750	456
55	67	0.050	8.98	3020	526
60	85	0.049	9.86	3300	600

*excluding oxide thickness
**Values Calculated Herein

Table 6-10. Concentration of Hydrogen in PPM as a Function of Burn-up and Depth into Cladding Surface**

Distance from Outer Surface µm	Burn-up 25MWd/ kgU	Burn-up 30MWd/ kgU	Burn-up 35MWd/ kgU	Burn-up 40MWd/ kgU	Burn-up 45MWd/ kgU	Burn-up 50MWd/ kgU	Burn-up 55MWd/ kgU	Burn-up 60MWd/ kgU
	PPM Hydrogen							
0	585	747	923	1114	1320	1540	1775	2020
40	585	747	923	1114	1320	1540	1775	2020
50	527	672	831	1003	1188	1386	1598	1823
100	263	336	415	501	594	693	799	911
150	187	239	295	356	422	493	568	648
200	135	172	212	256	304	354	408	466
250	100	127	157	189	224	262	302	344
300	76	97	120	145	172	200	231	263
570	76	97	120	145	172	200	231	263

**Values Calculated Herein

Table 6-11. Saturation Limits for Hydrogen in Zirconium as a Function of Temperature

Temperature °C	PPM
40	0.1
50	0.2
60	0.3
70	0.4
80	0.6
90	0.9
100	1.2
110	1.6
120	2.1
130	2.8
140	3.6
150	4.6
160	5.8
170	7.3
180	9.0
190	11
200	13
210	16
220	19
230	23
240	27
250	32
260	38
270	44
280	50
290	58
300	66

Temperature °C	PPM
300	66
310	75
320	85
330	96
340	108
350	120
360	134
370	149
380	165
390	182
400	201
410	221
420	242
430	264
440	288
450	313
460	339
470	367
480	396
490	427
500	459
510	493
520	529
530	565
540	604
550	644
560	686

(Ref. Pescatore et al. 1989, eq. 6)

Table 6-12. Causes of Fuel Failures in PWRs*

	Number of Assemblies							
Failure Cause	**1989**	**1990**	**1991**	**1992**	**1993**	**1994**	**1995**	**1996 (Partial)**
Handling Damage		6	2			1	1	1
Debris	146	11	67	20	13	6	10	1
Baffle Jetting								
Grid Fretting	14	18	9	33	36	9	33	19
Primary Hydriding		1		4				
Crudding/Corrosion							4	1
Cladding Creep Collapse							1	
Other Fabrication	1	15	1	5	3	1	15	3
Other Hydraulic					1			
Inspected/Unknown					36	36	13	2
Uninspected	43	58	35	61	14	3	12	1
Totals	204	109	114	123	103	56	89	27
Total Discharged	2196	3461	2937	3302	3612	2636	3666	

*Source R. L. Yang 1997

Table 6-13. Pin Crack Size Probability Distribution**

F(w) * 1	w, Microns 0	F(w) 1.000	w, Microns 0.0	F(w) 0.577	w, Microns 10.0
0.5769814	10	0.973	0.5	0.561	10.5
0.3329075	20	0.946	1.0	0.546	11.0
0.1920814	30	0.921	1.5	0.531	11.5
1.11E-01	40	0.896	2.0	0.517	12.0
6.39E-02	50	0.872	2.5	0.503	12.5
3.69E-02	60	0.848	3.0	0.489	13.0
2.13E-02	70	0.825	3.5	0.476	13.5
1.23E-02	80	0.803	4.0	0.463	14.0
7.09E-03	90	0.781	4.5	0.450	14.5
4.09E-03	100	0.760	5.0	0.438	15.0
2.36E-03	110	0.739	5.5	0.426	15.5
1.36E-03	120	0.719	6.0	0.415	16.0
7.85E-04	130	0.699	6.5	0.404	16.5
4.53E-04	140	0.680	7.0	0.393	17.0
2.61E-04	150	0.662	7.5	0.382	17.5
1.51E-04	160	0.644	8.0	0.372	18.0
8.70E-05	170	0.627	8.5	0.362	18.5
5.02E-05	180	0.610	9.0	0.352	19.0
2.09E-05	190	0.593	9.5	0.342	19.5
1.67E-05	200	0.577	10.0	0.333	20.0

*F(w) = Probability that pin has a crack larger than depth w
**Values Calculated Herein

Table 6-14. Fission Gas Pressure, and Stress vs. Burn-up (27°C Temperature)**

Fuel Burn-up MWd/kgU	Clad Thickness* cm	Plenum Pressure MPa	Median Crack Stress, MPa	Maximum Crack Stress, MPa
25	0.056	3.41	26.2	35.6
30	0.056	3.59	27.6	37.5
35	0.055	3.80	29.4	40.0
40	0.054	4.05	31.8	43.2
45	0.053	4.34	34.7	47.2
50	0.052	4.67	38.3	52.1
55	0.050	5.06	42.8	58.2
60	0.049	5.51	48.4	65.8

*excluding oxide thickness; includes crack depth
**Values Calculated Herein

Table 6-15. General Corrosion of Zircaloy as a Function of WP Failure Time**

WP Failure Time, Years	Peak Pin in Average WP Oxide Thickness µm	Peak Pin in Average WP Hydrogen Pickup ppm	Peak Pin in Design (Hot) WP Oxide Thickness µm	Peak Pin in Design (Hot) WP Hydrogen Pickup ppm
0	10	132	186	2400
1	10	132	178	2300
10	8	111	112	1500
100	1.3	16	10	130
1000	0.9	11	3	41
10,000	0.3	4	0.3	4

**Values Calculated Herein

Table 6-16. Comparison of Zr702 and C-276 Corrosion Rates

T °C	Solution Chemistry	Zr702 Corrosion Rate µm/yr	C-276 Corrosion Rate µm/yr	Ratio C-276/Zr
102	10% H_2SO_4	2.5	180	72
108	30% H_2SO_4	2.5	1,400	560
132	55% H_2SO_4	2.5	7,500	3,000
168	55% H_2SO_4	500	5,400	11
232	5% H_2SO_4	2.5	3,900	1,560
225	10% H_2SO_4	18	16,800	933
Boil.	20% HCl	18	6,900	383
204	65% HNO_3	8	660,000	82,500
150	20% H_3PO_4	23	990	43
			Average →	9,896

Yau, T.L. and Webster, R.T. 1987. "Corrosion of Zirconium and Hafnium," in *Metals Handbook. Ninth Edition, Volume 13: Corrosion*, ASM International, Metals Park, Ohio, USA, 707-721.

Table 6-17. Experimental Measurements of Zircaloy Creep

Condition	Einziger 1982	Einziger 1984	Matsuo 1987	Mayuzumi 1990	Peehs 1986
Lowest Temperature °C.	482	323	330	300	400
Highest Temperature °C.	571	323	420	420	400
Temperature Range	89	0	90	120	0
Lowest Stress, MPa	32	146	49	51	100
Highest Stress, MPa	50	157	314	126	120
Irradiated Mat	y	y	n	n	
Max Time, Hrs	7,680	2,100	3,000	7,400	6,000
Measured Strains, %	1.7 - 7	.004 - 0.16	0.4 - 0.92	0.3 - 6.8	0.19 - 0.30

Table 6-18. Temperature Dependency of the Matsuo Creep Correlation**

Temperature,°C	Hoop Stress,* MPa	Strain Rate, %/Yr
400	72	2.7
350	67	0.26
300	62	0.018
250	56	6.1E-4
200	51	9.8E-6

*Room Temperature Stress Fixed at 32 MPa
**Values Calculated Herein

Table 6-19. Measured Strain Limits for Zircaloy with Hydrides

Source	Temp °C	Ultimate Tensile Stress, MPa	Uniform Elongation Strain %	Number of Tests	Notes
Van Swam, 97	25	910	1.5	1	Irrad
Van Swam, 97	25	775-883	2	2	Irrad
Van Swam, 97	25	660-956	4	3	Irrad
Van Swam, 97	25	710-878	5	3	Irrad
Van Swam, 97	25	840	6	1	Irrad
Van Swam, 97	350	602	3	1	Irrad
Van Swam, 97	350	586-666	4	7	Irrad
Van Swam, 97	350	376-417	4.5	2	Irrad
Puls, 88	25	625-1079	4.1	3	Unirr, hydrides added
Puls, 88	25	659-689	4.7	6	Unirr, hydrides added
Puls, 88	25	689-730	6	2	Unirr, hydrides added
Einziger, 82	482	43[a]	1.7	2	Irrad, no failure
Einziger, 82	510	39[a]	3.4	5	Irrad, no failure
Einziger, 82	571	23-50[a]	5	3	Irrad, no failure
Einziger, 82	571	33-39[a]	7	5	Irrad, no failure
Chung, 87	325	337	0.4	1	Irrad
Chung, 87	325	344	0.8	1	Irrad
Chung, 87	325	384-498	1	3	Irrad
Chung, 87	325	469-545	2	2	Irrad
Chung, 87	325	552	11	1	Irrad
Number of Tests				54	
Average Strain			4.1		
Stand. Dev.			2.1		
Variance			4.2		

[a]: Stress at which creep test was performed, no pin failure observed.

Table 6-20. Pressure Effect from Helium Production

Time(yrs)	Temperature °C	Helium Pres. MPa	Fis. Gas Pres. MPa	Total Pressure MPa
1	210	0.03	6.68	6.7
10	240	0.11	7.10	7.2
100	150	0.32	5.85	6.2
1,000	104	1.03	5.22	6.2
10,000	79	3.44	4.87	8.3
100,000	27	4.96	4.15	9.1
1,000,000	27	8.41	4.15	12.6
Fission gas pressure (27°C) = 4.15 MPa Time < 10,000, p (MPa) = 0.0222 t^0.5537 Time > = 10,000, p (MPa) = 0.422 t^0.229				

Table 6-21. Stress and Stress Intensity Factors vs. Burn-up at 350°C**

Fuel Burn-up MWd/kgU	Median Crack Stress MPa	Median Crack Stress Intensity Factor K_I, MPa-m$^{0.5}$	Maximum Crack Stress MPa	Maximum Crack Stress Intensity Factor K_I, MPa-m$^{0.5}$
25	54.3	0.233	73.9	1.156
30	57.3	0.245	78.0	1.218
35	61.2	0.261	83.2	1.294
40	66.0	0.279	89.8	1.388
45	72.0	0.302	98.0	1.501
50	79.6	0.330	108.2	1.637
55	88.9	0.363	120.9	1.801
60	100.4	0.402	136.6	1.998

**Values Calculated Herein

Table 6-22. Threshold to Stress Intensity Factors for Two Burn-ups

Temperature °C	40 MWd/kgU Median Crack K_I, MPa-m$^{0.5}$	40 MWd/kgU Maximum Crack K_I, MPa-m$^{0.5}$	60 MWd/kgU Median Crack K_I, MPa-m$^{0.5}$	60 MWd/kgU Maximum Crack K_I, MPa-m$^{0.5}$
50	0.14	0.72	0.21	1.04
100	0.17	0.83	0.24	1.20
150	0.19	0.94	0.27	1.36
200	0.21	1.05	0.31	1.52
250	0.23	1.17	0.34	1.68
300	0.26	1.28	0.37	1.84
350	0.28	1.39	0.40	2.00

The threshold stress intensity factor is K_{IH} = 6.7 MPa - m$^{0.5}$

Table 6-23. Puls' Zircaloy-2 Strain Tests on Zirconium with Reoriented Hydrides

Hydride Length µm	Type*	Stress σ_y (0.2%) MPa	Ult. σ MPa	Uniform/Total Strain %
Initial Material		627	650	
7-20		632	678	4.7/15.8
7-20	y	627	675	4.7/15.8
7-20		612	659	4.7/15.8
7-20	n	783	885	
7-20	n,y	774	882	
7-20	n	933	1095	
7-20	n	766	858	
7-20	a	628	698	6 / 9
30-60		627	689	4.7/14.3
30-60	y	605	661	4.7/14.3
30-60	n	861	958	
30-60	n,y	776	921	
50-90		1079	1160	4.1/13.6
50-90	y	689	741	4.1/13.6
50-90		625	647	4.1/13.6
50-90	n	721	803	
50-90	n,y	923	1032	
50-90	n	811	936	
50-90	a	633	701	- / 6
50-90	a	643	730	- / 6

*Type, y= hydride reoriented near yield stress, n - notched, a = arrested (test terminated before failure)

Source: M.P. Puls, "The influence of hydride size and matrix strength on fracture initiation at hydrides in zirconium alloys," Met. Trans. A 19A:1507-1522 (1988), Tables 1,3,6

Table 6-24. Amount of Fuel Damage as a Function of the Focusing Parameter for Fuel Struck by Blocks with a Circular Punch

Focusing Param.	Average Number of Breaks Per Rod			Fraction of Rods Broken			Fraction of Fuel Exposed			Punch Aspect Ratio	
	Typical	Hi-burn	95% typ. + 5% Hi-burn	Typical	Hi-burn	95% typ. + 5% Hi-burn	Typical	Hi-burn	95% typ. + 5% Hi-burn	Typical	Hi-burn
1.0	0.0325	0.6145	0.0616	0.0142	0.1799	0.0225	0.0060	0.1055	0.0110	0.006	0.045
0.9	0.0386	0.6446	0.0689	0.0175	0.2050	0.0268	0.0064	0.0997	0.0111	0.008	0.058
0.8	0.0463	0.6831	0.0782	0.0217	0.2383	0.0325	0.0068	0.0941	0.0112	0.010	0.077
0.7	0.0568	0.7339	0.0906	0.0273	0.2830	0.0401	0.0073	0.0886	0.0113	0.013	0.106
0.6	0.0700	0.8073	0.1069	0.0345	0.3481	0.0501	0.0076	0.0839	0.0114	0.020	0.156
0.5	0.0853	0.9058	0.1263	0.0441	0.4343	0.0636	0.0076	0.0785	0.0112	0.033	0.248
0.4	0.1032	1.0390	0.1500	0.0576	0.5490	0.0822	0.0073	0.0716	0.0105	0.059	0.440
0.3	0.1264	1.1410	0.1771	0.0784	0.6482	0.1069	0.0067	0.0576	0.0092	0.122	0.868
0.2	0.1650	0.9978	0.2066	0.1174	0.6276	0.1429	0.0058	0.0323	0.0071	0.329	1.77
0.1	0.2682	0.5934	0.2845	0.2229	0.4467	0.2341	0.0046	0.0090	0.0049	1.92	4.62

Table 6-25. Amount of Fuel Damage as a Function of the Focusing Parameter for Fuel Struck by Blocks with a Linear Punch (Composite of Eight Punch Orientations)

Focusing Param.	Average Number of Breaks Per Rod			Fraction of Rods Broken			Fraction of Fuel Exposed		
	Typical	Hi-burn	95% typ. + 5% Hi-burn	Typical	Hi-burn	95% typ. + 5% Hi-burn	Typical	Hi-burn	95% typ. + 5% Hi-burn
1	0.0325	0.6145	0.0616	0.0142	0.1799	0.0225	0.0060	0.1055	0.0110
0.9	0.0348	0.6258	0.0643	0.0154	0.1893	0.0241	0.0062	0.1032	0.0110
0.8	0.0377	0.6402	0.0678	0.0170	0.2018	0.0262	0.0063	0.0990	0.0109
0.7	0.0416	0.6593	0.0725	0.0191	0.2186	0.0291	0.0064	0.0940	0.0108
0.6	0.0467	0.6875	0.0787	0.0219	0.2436	0.0329	0.0065	0.0892	0.0106
0.5	0.0528	0.7261	0.0864	0.0257	0.2773	0.0382	0.0066	0.0845	0.0105
0.4	0.0600	0.7787	0.0959	0.0310	0.3225	0.0456	0.0067	0.0797	0.0103
0.3	0.0695	0.8209	0.1071	0.0392	0.3630	0.0554	0.0068	0.0713	0.0100
0.2	0.0852	0.7731	0.1196	0.0545	0.3603	0.0698	0.0072	0.0526	0.0095
0.1	0.1255	0.6296	0.1507	0.0950	0.2995	0.1052	0.0092	0.0267	0.0101

Table 6-26. Total Measured Release Fraction from Wilson Series 1 Tests

Fraction of Inventory × 10^5 [a]				
Component	**Bare Fuel**	**Slit Defect**	**Holes Defect**	**Undefected**
Uranium (μg)	28.0 (9510)	0.078 (28)	<0.041 (<14)	<0.018 (<6.6)
239Pu + 240Pu (nCi)	28.0 (7940)	0.341 (104)	0.069 (20)	0.027 (8)
241Am (nCi)	21.7 (12,604)	0.208 (130)	<0.030 (<18.6)	<0.011 (<6.4)
244Cm (nCi)	30.0 (13,300)	0.76 (362)	0.039 (18.1)	0.008 (<3.9)
237Np[b] (nCi)	54 (4.73)	2.2 (0.2)		
137Cs (nCi)	300[c] (1.94 x 10^6)	142.1 (3.94 x 10^6)	85.6 (2.33 x 10^6)	0.041 (1.1 x 10^3)
99Tc[d] (nCi)	230 (900)	12.1 (51)	<6.7 (<28)	

[a]Total measured release given in parentheses.

[b]^{237}Np includes only vessel strip from initial and second runs and final solution from second run.

[c]Estimate based on maximum ^{137}Cs activities measured in solution.

[d]^{99}Tc includes only final solution and vessel strip from initial and second runs.

* Ref: Wilson 1985 (HEDL-TME 84-30, Table 15)

Table 6-27. Fractional Distribution of Gap Inventory Species Used in TSPA-1995

Nuclide	Spent Fuel Matrix	Gap Inventory[1]
^{14}C	U(0.94, 0.99)[2]	U(0.0125, 0.0575)[2]
^{135}Cs	0.98	0.02
^{129}I	0.98	0.02
^{79}Se	0.98	0.02
^{99}Tc	0.98	0.02

[1]Includes the inventory in grain boundary.

[2]Uniformly distributed with the minimum and maximum given.

Table 6-28. Regression Analysis

(a) Regression Analysis Results Using all Data

	Mean
1/Temp	0.00313
Log(CO3)	-2.56
Log(O2)	0.59
pH	9.00
Log(Burnup)	0.82
(LCO3)2	0.73

SUMMARY OUTPUT All data

Regression Statistics	
Multiple R	0.927097
R Square	0.859510
Adjusted R Square	0.817742
Standard Error	0.239941
Observations	49

ANOVA

	df	SS	MS	F	Significance F
Regression	11	13.032133	1.184739	20.578456	1.59E-12
Residual	37	2.130158	0.057572		
Total	48	15.162291			

	Coefficients	Standard Error	t Stat	P-value	Lower 95%	Upper 95%
Intercept	0.5105	0.0356	14.3430	0.0000	0.4383	0.5826
1/Temp	-1173.7842	158.5203	-7.4046	0.0000	-1494.9765	-852.5919
Log(CO3)	0.0767	0.0454	1.6910	0.0993	-0.0152	0.1686
Log(O2)	0.3242	0.0458	7.0777	0.0000	0.2314	0.4170
pH	0.0531	0.0492	1.0788	0.2877	-0.0466	0.1528
Log(Burnup)	-0.1042	0.0482	-2.1627	0.0371	-0.2018	-0.0066
(1/T)LB	561.3420	214.9952	2.6110	0.0130	125.7208	996.9633
(LCO3)LB	-0.1092	0.0547	-1.9954	0.0534	-0.2200	0.0017
(LO2)LB	-0.1440	0.0610	-2.3621	0.0235	-0.2675	-0.0205
(pH)LB	-0.3091	0.0688	-4.4950	0.0001	-0.4484	-0.1698
(LCO3)2-M()	-0.3531	0.0827	-4.2679	0.0001	-0.5207	-0.1854
(1/T)(LO2)	-369.2896	196.1581	-1.8826	0.0676	-766.7432	28.1640

Table 6-28. Regression Analysis (Continued)

(b) Preliminary Regression Analysis Results Using Spent Fuel Data at Burnups of >= 30 MW-days/kgU, and the Mean Values of the Parameters used in the Regression Analysis

Coefficient	Actual Mean Value; used in later predictive equation	Mean Value Used in Regression Analysis for Coefficients
1/Temp	0.00316	0.00311
Log(CO3)	-2.51	-2.51
Log(O2)	0.71	0.71
pH	8.89	8.89
(LCO3)2-M()	0.74	0.74

SUMMARY OUTPUT

High-BU data

Regression Statistics	
Multiple R	0.9218
R Square	0.8498
Adjusted R Square	0.8047
Standard Error	0.1660
Observations	27

	Coefficients	*Standard Error*	*t Stat*	*P-value*	*Lower 95%*	*Upper 95%*
Intercept	0.5083	0.0327	15.5515	0.0000	0.4401	0.5764
1/Temp	-862.3339	142.3854	-6.0563	0.0000	-1,159.3446	-565.3233
Log(CO3)	0.0527	0.0457	1.1517	0.2630	-0.0427	0.1481
Log(O2)	0.2915	0.0471	6.1858	0.0000	0.1932	0.3899
pH	-0.1307	0.0385	-3.3954	0.0029	-0.2109	-0.0504
(LCO3)2-M()	-0.1381	0.0818	-1.6885	0.1069	-0.3088	0.0325
(1/T)(LO2)	-781.7371	189.3113	-4.1294	0.0005	-1,176.6335	-386.8408

Table 6-29. Physical Characteristics of DOE SNF

Category	Air Alteration Rate (fraction/yr)	Matrix Dissolution Rate ($g/m^2/yr$)	Matrix Surface Area (m^2/g)	Failed Cladding (%)	Free Radionuclide Inventory (fraction)	Gap Radionuclide Inventory (fraction)	Fuel Area (m^2/pkg)	Fuel Volume (m^3/pkg)
1	0	metal model	7.0E-05	100	0.001	0	1.4E+03	1.1E+00
2	0	metal model	6.5E-03	10	0.00001	0	3.7E+01	8.6E-03
3	0	metal model x 10	4.0E-04	10	0.00001	0	2.1E+01	5.5E-02
4	0	oxide model	9.5E-04	100	0	.01-.02	5.0E+02	5.3E-02
5	0	oxide model	9.5E-02	100	0	0.0001	1.4E+04	1.4E-02
6	0	metal model x 0.1	7.4E-03	100	0.0001	0	1.2E+02	8.2E-03
7	0	metal model x 0.1	1.4E-02	100	0.0001	0	8.5E+01	1.5E-02
8	0	Si carbide model	2.2E-02	1	0.00001	0	1.1E+03	6.6E-03
9	0	metal model x 10	2.2E-02	60	0.1	0.001	6.1E+02	3.6E-03
10	0	metal model x 100	2.6E-03	10	0	.01-.02	8.6E+01	3.3E-03
11	0	oxide model	9.5E-04	10	0	.01-.02	3.6E+01	4.0E-03
12	0	Ceramic model	5.0E-04	10	0	.01-.02	3.5E+02	8.8E-02
13	0	oxide model x 0.1	1.0E-04	10	0.00001	0.00001	2.0E+00	4.4E-02
15	N/A[1]	N/A	N/A	N/A	N/A	N/A	N/A	N/A
16	0	metal model	7.0E-05	100	0.001	0	1.7E+01	2.8E-02

[1]Navy SNF is analyzed using a release source term at the boundary of the waste package.

Table 6-30. Log_{10} Glass Dissolution Rate in $g/m^2/day$ (from Knauss et al. 1990)

pH	T = 25°C	50°C	70°C
1	-1.25	0.02	0.51
2	-1.73	-0.68	-0.18
3	-2.21	-1.38	-0.87
4	-2.69	-2.08	-1.56
5	-3.17	-2.78	-2.25
6	-	-	-2.94
7	-4.53	-3.43	-2.3
8	-4.02	-2.92	-1.9
9	-3.51	-2.41	-1.5
10	-3	-1.9	-1.1
12	-1.98	-0.88	-0.3

Table 6-31. Amorphous Silica Solubilities (Log_{10} [molality]) (from Johnson et al. 1992)

Temperature, °C	0	25	60	90	100	150
Amorphous Silica, K	-2.99	-2.71	-2.43	-2.26	-2.20	-1.98
Christobalite, Q	-3.89	-3.45	-3.02	-2.75	-2.68	-2.36

Table 6-32. Distributions of Solubility-Limited Aqueous Radionuclide Concentrations for Base Case

RN	Distribution Type	Distribution Variable	Minimum Value g/m^3 & [mol/l]	Maximum Value g/m^3 & [mol/l]	Mean or Peak g/m^3 & [mol/l]	C.V.	Source
Ac	Uniform	Concentration	2.3E-5 [1.0E-10]	2.3E-1 [1.0E-6]	1.2E-1 [5E-7]	—	Project Elicitation
Am	Uniform	Concentration	2.4E-5 [1.0E-10]	2.4E-1 [1.0E-6]	1.2E-1 [5E-7]	—	Project Elicitation
Cm	Triangular (two temperature ranges)	log (Concen.)	T < 55°C: log(1.2E-6) [log(4.9E-12)] T > 55°C: log(2.4E-10) [log(9.7E-16)]	T < 55°C: log(1.2E-4) [log(4.9E-10)] T > 55°C: log(2.4E-8) [log(9.7E-14)]	T < 55°C: log(1.2E-5) [log(4.9E-11)] T > 55°C: log(2.4E-9) [log(9.7E-15)]	—	Wilson (1987; 1990a; 1990b)
Cs	Triangular	log (Concen.)	log(1.2) [log(9.0E-6)]	log(2.1E+3) [log(1.6E-2)]	log(3.9E+2) [log(2.9E-3)]	—	Golder Assoc. (1993), Shaw (1992)
Nb	Uniform	log (Concen.)	log(9.3E-5) [log(1.0E-9)]	log(9.3E-3) [log(1.0E-7)]	log(9.3E-4) [log(1.0E-8)]	—	Project Elicitation
Ni	Beta	log (Concen.)	log(5.9E-2) [log(1.0E-6)]	log(5.9E+3) [log(1.0E-1)]	log(1.1E+2) [log(1.8E-3)]	0.34 [0.25]	Project Elicitation
Np	Beta	log (Concen.)	log(1.2E-2) [log(5E-8)]	log(2.4E+1) [log(1.0E-4)]	log(3.4E-1) [log(1.4E-6)]	1.20 [0.099]	CRWMS M&O (1998a)*
Pa	Uniform	log (Concen.)	log(2.3E-5) [log(1.0E-10)]	log(2.3) [log(1.0E-5)]	log(7.3E-3) [log(3.2E-8)]	—	Project Elicitation
Pb	Beta	log (Concen.)	log(2.1E-3) [log(1.0E-8)]	log(2.1) [log(1.0E-5)]	log(6.6E-2) [log(3.2E-7)]	0.44 [0.08]	Project Elicitation
Pd	Uniform	log (Concen.)	log(1.0) [log(9.4E-6)]	log(1.0E+4) [log(9.4E-2)]	log(1.0E+2) [log(9.4E-4)]	—	Golder Assoc. (1993)*
Pu	Uniform	Concentration	2.4E-3 [1.0E-8]	2.4E-1 [1.0E-6]	1.2E-1 [5.1E-7]	•••	Project Elicitation*
Ra	Beta	log (Concen.)	log(2.3E-4) [log(1.0E-9)]	log(2.3) [log(1.0E-5)]	log(2.3E-2) [log(1.0E-7)]	0.10 [0.43]	Project Elicitation
Se	Triangular	log (Concen.)	log(7.9E+2) [log(1.0E-2)]	log(5.5E+5) [log(7.0)]	log(7.9E+3) [log(1.0E-1)]	—	Golder Assoc. (1993), Shaw (1992)

Table 6-32. Distributions of Solubility-Limited Aqueous Radionuclide Concentrations for Base Case (Continued)

RN	Distribution Type	Distribution Variable	Minimum Value g/m^3 & [mol/l]	Maximum Value g/m^3 & [mol/l]	Mean or Peak g/m^3 & [mol/l]	C.V.	Source
Sm	Uniform	Concentration	1.5E-5 [1.0E-10]	1.5E-1 [1.0E-6]	7.5E-2 [5.0E-7]	—	Project Elicitation
Sn	Uniform	Concentration	1.2E-6 [1.0E-11]	1.2E-2 [1.0E-7]	6.0E-3 [5.0E-8]	—	Project Elicitation
Tc	Triangular	log (Concen.)	log(3.5E-2) [log(3.6E-7)]	log(9.9E+5) [log(1.0E+1)]	log(1.0E+2) [log(1.0E-3)]	—	Golder Assoc. (1993), Shaw (1992)
Th	Uniform	log (Concen.)	log(2.3E-5) [log(1.0E-10)]	log(2.3E-2) [log(1.0E-7)]	log(7.3E-4) [log(3.2E-9)]	—	Project Elicitation
U	Beta	log (Concen.)	log(2.4E-3) [log(1.0E-8)]	log(2.4E+3) [log(1.0E-2)]	log(7.6) [log(3.2E-5)]	1.02 [0.2]	Project Elicitation
Zr	Uniform	log (Concen.)	log(9.1E-8) [log(1.0E-12)]	log(9.1E-3) [log(1.0E-7)]	log(2.9E-5) [log(3.2E-10)]	—	Project Elicitation

log: refers everywhere in the table to the base 10 logarithm.

RN: stands for radionuclide.

Mean or Peak: The values listed are the Arithmetic Mean for all distributions *except* log triangular distributions where the values listed correspond to the Peak of the distributions. *NOTE*: For any Distribution of log(Concen.), the value of the Mean is *not equivalent* to the log(Mean) for the corresponding Distribution of Concentration.

C.V.: stands for Coefficient of Variation which equals the absolute value of the ratio of the Standard Deviation to the Mean. Values given only for log beta distributions.

e+: represents positive power(s) of ten.

e•: represents negative power(s) of ten.

Project Elicitation: Conducted at Sandia National Laboratory on April 13, 1993. Documented in Wilson et al. (1994).

*: indicates modifications to original source information • • see text for discussion

Table 6-33. Table 3-1 from CRWMS M&O (1998a)–Summary of Np concentrations determined from spent fuel alteration/dissolution rate studies compared to the range of values provided by project-expert elicitation, which are based on the data of Nitsche et al. (1993, 1994).

Study	C_{Np}, M	Flow Rate, L/d	Notes
Wilson 1990a	2.3×10^{-9}	0 (batch)	25 °C Series #2, last cycle average
Wilson 1990b	1.4×10^{-9}	0 (batch)	25 °C Series #3, last cycle HBR
Wilson 1990b	5.4×10^{-10}	0 (batch)	85 °C Series #3, last cycle average
Wilson 1990a; 1990b	5.9×10^{-9}	0 (batch)	85 °C high value of Wilson (1990a,b)
Finn et al. 1995 ATM-106	1.6×10^{-10}	2.14×10^{-4}	90 °C, ATM-106 last cycle, J-13 water, logf_{O2} = atm
Finn et al. 1995 ATM-103	9.9×10^{-10}	2.14×10^{-4}	90 °C, ATM-103 last cycle, J-13 water, logf_{O2} = atm
Gray and Wilson 1995	2.3×10^{-10}	1.44×10^{-1}	22 °C, J-13 water, log f_{O2} = atm (assumes congruent dissolution)
Gray and Wilson 1995	6.1×10^{-10}	1.44×10^{-1}	90°C, J-13 water, log f_{O2} = atm (extrapolation of 22°C value using temperature dependence of Gray and Wilson, 1995see text for discussion)
Project-expert elicitation* Range (based primarily on Nitsche et al. 1993, 1994)	5×10^{-6} to 1×10^{-2}	0 (batch)	Oversaturation values, initial J-13 with added NaOH and HClO4, metastable Na-NpO2-CO3-Hydrate and Np2O5 phases observed, 25, 60, & 90 °C
Nitsche et al. 1993 Table VI	4.4×10^{-5} to 6.4×10^{-3}	0 (batch)	Oversaturation values, initial J-13 with added NaOH and HClO4, metastable Na-NpO2-CO3-Hydrate and Np2O5 phases observed, 25, 60, & 90 °C
Nitsche et al. 1994 Table VI	7.0×10^{-6} to 2.9×10^{-3}	0 (batch)	Oversaturation values, initial UE-25p#1 with added NaOH and HClO4, metastable Na-NpO2-CO3-Hydrate observed, 25 & 60 °C

*-Elicitation values given by project experts modified as recommended by the Solubility Working Group (see text for discussion).

Table 6-34. Preliminary results of calculated solubility limits for Np, Pu, and U

Calculated Molalities				Phase Constraint	Comment
31°C	60°C	90°C			
			Neptunium		
8.76E-07	6.69E-07	7.60E-07		NpO_2	Most stable at all three temperatures
2.06E-04	1.97E-04	2.64E-04		$NpO_2OH(am)$	1st metastable at all three temperatures
6.96E-04	5.53E-04	3.96E-04		Np_2O_5	3rd metastable at 31°C, 2nd at 60 and 90°C
3.50E-04	7.07E-03	0.242		$NaNpO_2CO_3{:}3.5H_2O$	2nd metastable at 31°C, 3rd at 60 and 90°C
			Plutonium		
7.78E-13	4.80E-13	4.78E-13		PuO_2	Most stable at all three temperatures
3.41E-08	3.76E-08	6.46E-08		$PuO_2(OH)_2$	1st metastable at all three temperatures
3.38E-05	3.18E-05	2.25E-05		$Pu(OH)_4$	2nd metastable at all three temperatures
			Uranium		
3.22E-09	7.53E-10	4.30E-10		Haiweeite	Most stable at all three temperatures
1.48E-06	5.68E-08	4.56E-09		$CaUO_4$	2nd metastable at 31°C, 1st at 60 and 90°C
1.45E-07	2.02E-07	3.85E-07		Soddyite	1st metastable at 31°C, 2nd at 60 and 90°C
1.21E-04	3.33E-05	2.02E-05		Schoepite	Highly metastable

Table 6-35. Summary of UO_2 Alteration Phases

Uranyl-Oxide Hydrates	
Schoepite (meta-schoepite)	$UO_3 \cdot nH_2O$ ($n < 2$)
Dehydrated Schoepite	$UO_3 \cdot (0.8\text{-}1.0H_2O)$
Compreignacite	$(Na, K)_2 [(UO_2)_6O_4(OH)_6] \cdot 8H_2O$
Becquerelite	$Ca[(UO_2)_6O_4(OH)_6] \cdot 8H_2O$
Uranyl Silicate Hydrate	
Soddyite	$(UO_2)_2 SiO_4 \cdot 2H_2O$
Uranyl Alkaline Silicate Hydrates	
Uranophane	$Ca(UO_2)(SiO_3)(OH)_2 \cdot 5H_2O$
Boltwoodite	$K2(UO_2)_2 (SiO_4)_2 (H_3O)_2 H_2O$
Na-Boltwoodite	$(Na,K)(UO_2)(SiO_4)(H_3O) H_2O$
Sklodowskite	$Mg(UO_2)_2(SiO_4)_2(H_3O)_2 \cdot 2H_2O$
Non-Uranyl Phases	
Palygorskite	$(Mg,Al_{0.12\text{-}0.66})_5(Si,Al_{0.12\text{-}0.66})_8O_{20}(OH)_5 \cdot 4H_2O$
Fe-Oxides	
Ti-Oxides	
Amorphous Silica	

Table 6-36. Spent Fuel Transformation Mineral Phases in Vapor and Drip Tests

Time Level	Dominant Mineral Phases in Vapor & Drip Tests		
	Vapor Test	**Low-drip Test**	**High-drip Test**
1	Spent Fuel (UO_2)	Spent Fuel (UO_2)	Spent Fuel (UO_2)
2	Higher Oxides	Higher Oxides	Higher Oxides
3	Schoepite	Schoepite	Schoepite
4	—	—	Compreignacite Bequerelite
5	—	—	Soddyite
6	—	—	Boltwoodite

Table 6-37. Equilibrium Film Mass Concentrations Fitted to ATM-103 Spent Fuel Vapor Test and Low-Drip Test Data Using the Advective Transport Limited Model

Fitted Vapor Water Recirculation Velocity = 2.666E-06 cm/d									
Time Interval	Fitted Equilibrium Mass Concentrations g/ml								
	Pu	U	Cs	Tc	Sr	Mo	Am	Np	I
	0.00E+00	0.00E+00	0.00E+00	0.00E+00	0.00E+00	0.00E+00	0.00E+00	0.00E+00	0.00E+00
1	5.343E-07	1.599E-05	5.349E-08	1.700E-07	2.899E-13	1.317E-07	1.216E-06	8.333E-08	2.117E-04
2	1.201E-08	1.499E-06	4.263E-09	1.171E-08	4.701E-09	2.899E-08	2.279E-09	6.481E-10	1.560E-07
3	7.979E-10	1.397E-07	1.920E-10	2.514E-09	3.032E-10	1.853E-09	3.873E-10	8.059E-11	1.168E-07
4	1.531E-11	2.937E-07	5.126E-10	3.969E-08	6.121E-10	4.832E-10	9.704E-11	3.835E-12	6.983E-08
5	4.456E-12	1.814E-09	2.463E-11	8.203E-10	8.284E-10	1.464E-09	3.030E-12	1.054E-12	1.262E-08
6	2.605E-11	5.536E-09	2.219E-10	1.112E-08	2.160E-09	2.704E-10	7.932E-12	6.361E-12	7.155E-09
7	3.386E-12	4.963E-09	3.132E-10	3.407E-09	6.617E-10	8.341E-11	1.579E-11	2.692E-12	2.201E-09

Table 6-38. Equilibrium Film Mass Concentrations Fitted to ATM-106 Spent Fuel Vapor Test and Low-Drip Test Data Using the Advective Transport Limited Model

Fitted Vapor-Water Recirculation Velocity = 2.014E-05 cm/d									
Time Interval	Fitted Equilibrium Mass Concentrations g/ml								
	Pu	U	Cs	Tc	Sr	Mo	Am	Np	I
	0.00E+00	0.00E+00	0.00E+00	0.00E+00	0.00E+00	0.00E+00	0.00E+00	0.00E+00	0.00E+00
1	4.366E-07	6.025E-05	1.515E-10	2.662E-07	1.445E-10	2.330E-07	3.632E-07	1.067E-07	6.026E-04
2	4.959E-09	1.014E-06	1.822E-09	2.901E-09	1.245E-08	1.705E-07	6.001E-10	5.934E-10	1.585E-06
3	7.444E-11	3.065E-08	4.400E-10	6.844E-10	5.952E-10	2.421E-08	8.322E-11	1.950E-11	1.826E-06
4	2.992E-11	4.625E-08	8.306E-10	1.771E-08	7.612E-09	1.888E-09	5.797E-12	3.734E-11	4.080E-07
5	5.811E-12	4.886E-10	1.454E-10	7.647E-10	1.140E-09	2.181E-09	1.190E-12	1.104E-12	3.349E-08
6	3.758E-12	9.465E-10	1.097E-09	5.164E-09	3.411E-10	1.373E-10	2.504E-12	3.514E-13	4.013E-08
7	1.915E-07	2.704E-05	1.128E-07	2.024E-09	1.334E-10	5.248E-11	4.468E-08	1.349E-08	1.508E-08

Table 6-39. Comparison of Long-Term Equilibrium Film Mass Concentrations Fitted to Spent Fuel Vapor Test and Low-Drip Test Data Against TSPA (CRWMS M&O 1995) Recommended Solubility Limits

Equilibrium Concentration Or Solubility Limit g/ml	Pu	U	Cs	Tc	Am	Np
ATM-103 Equilib.Conc@925 day	2.605E-11	5.536E-09	2.219E-10	8.203E-10	3.030E-12	1.054E-12
ATM-106 Equilib.Conc@926 day	5.811E-12	4.886E-10	1.454E-10	7.647E-10	1.190E-12	1.104E-12
TSPA 1995 - Solubility Average	1.200E-07	7.600E-06	3.900E-04	1.000E-04	1.200E-07	3.400E-05
TSPA 1995 - Solubility Min	2.400E-09	2.400E-09	1.200E-06	3.500E-08	2.400E-11	1.200E-06
TSPA 1995 - Solubility Max	2.400E-07	2.400E-03	2.100E-03	9.900E-01	2.400E-07	2.400E-03

Table 6-40. Temperature, Incoming Water Composition, and Gas Fugacities

Parameters	Scenario 1 (Period E)	Scenario 2 (Period F)
T (°C)	70	30
pH	8.2	8.12
Si (molality)	1.36E-3	4.42E-4
Na (molality)	1.99E-3	1.99E-3
Cl (molality)	2.01E-4	2.01E-4
Ca (molality)	9.44E-5	3.18E-4
$\log f_{CO2}$ (atm.)	-3.0	-3.0
$\log f_{O2}$ (atm.)	-0.7	-0.7
U (molality)[1]	1.0E-10	1.0E-10
Np (molality)[1]	1.0E-14	1.0E-14

[1] U and Np concentrations are arbitrarily assumed.

Table 6-41. Equilibrium Reactions Considered in the Step-1 Simulations

Aqueous Equilibrium Reactions	* Log K^{eq}
$H_2O = H^+ + OH^-$	-0.1494E+02 0.4171E-01 -0.1917E-03 0.4950E-06 -0.6159E-09
$CO_2(aq) + H_2O = H^+ + HCO_3^-$	-0.6576E+01 0.1198E-01 -0.1362E-03 0.4131E-06 -0.5483E-09
$HCO_3^- = H^+ + CO_3^{--}$	0.1062E+02 -0.1397E-01 0.1143E-03 -0.3352E-06 0.4687E-09
$HSiO_3^- + H^+ = SiO_2(aq) + H_2O$	0.1033E+02 -0.1707E-01 0.4438E-04 0.3611E-07 -0.9495E-10
$CaCO_3(aq) + H^+ = Ca^{++} + HCO_3^-$	0.7500E+01 -0.2156E-01 0.7888E-04 -0.1821E-06 0.8651E-10
$CaHCO_3^+ = Ca^{++} + HCO_3^-$	-0.1091E+01 0.3525E-02 -0.9368E-04 0.3085E-06 -0.4615E-09
$NaCO_3^- + H^+ = Na^+ + HCO_3^-$	0.9810E+01 -0.2859E-02 0.1433E-03 -0.3573E-06 0.3362E-09
$NaHCO_3(aq) = Na^+ + HCO_3^-$	-0.3675E+00 0.8192E-02 -0.9257E-06 -0.4679E-07 0.2168E-09
$NaCl = Na^+ + Cl^-$	0.8298E+00 -0.1559E-02 -0.2947E-04 0.1183E-06 -0.2367E-09
$NaHSiO_3(aq) + H^+ = Na^+ + SiO_2(aq) + H_2O$	0.8425E+01 -0.5331E-02 -0.2584E-04 0.2532E-06 -0.4395E-09

Table 6-41. Equilibrium Reactions Considered in the Step-1 Simulations (Continued)

Aqueous Equilibrium Reactions	* Log K^{eq}
$UO_2(CO_3)_3^{----} + 3H^+ = UO_2^{++} + 3\ HCO_3^-$	0.9493E+01 -0.4015E-03 -0.5581E-04 0.1200E-06 -0.2995E-09
$UO_2(CO_3)_2^{--} + 2H^+ = UO_2^{++} + 2\ HCO_3^-$	0.4492E+01 -0.3047E-01 0.4683E-04 -0.7901E-07 -0.7331E-10
$UO_2(CO_3)\ (aq) + H^+ = UO_2^{++} + HCO_3^-$	0.9531E+00 -0.1163E-01 -0.3975E-08 0.8229E-07 -0.3169E-09
$UO_2(OH)_3^- + 3H^+ = UO_2^{++} + 3H_2O$	19.2227
$UO_2(OH)_2\ (aq) + 2H^+ = UO_2^{++} + 2H_2O$	10.3155
$UO_2(OH)^+ + H^+ = UO_2^{++} + H_2O$	0.5910E+01 -0.3035E-01 0.1067E-03 -0.2529E-06 0.2606E-09
Gaseous-Aqueous Equilibrium Reactions	
$CO_2(g) + H_2O = H^+ + HCO_3^-$	-0.7676E+01 -0.4984E-02 -0.2707E-04 0.1083E-06 -0.2044E-09
$O_2(g) = O_2(aq)$	2.660 0.1142E-1 -0.9291E-4 0.2735E-6 -0.3402E-9

*The numbers under the column of log K^{eq} are the polynomial coefficients of equilibrium constants as a function of temperature. Please see the footnote of Table 6-42.

Table 6-42. Solid Reactions

Solid	Reaction	*Log K^{eq}	Source
Spent Fuel UO_2	$UO_2 + 2\ H^+ + 0.5\ O_2(g) = UO_2^{++} + H_2O$	0.3118E+02 -.1516E+00 0.4863E-03 -0.1077E-05 0.1083E-08	(Uraninite) EQ3/6
Uranophane $Ca(UO_2)_2(SiO_3)_2(OH)_2$	Uranophane + 6 H^+ = Ca^{++} + 2 $SiO_2(aq)$ + 2 UO_2^{++} + 4 H_2O	9.42	Nguyen et al. 1992
Schoepite $UO_3{:}2H_2O$	(Schoepite) + 2 H^+ = UO_2^{++} 3 H_2O	0.5656E+01 -0.3578E-01 0.1328E-03 -0.3213E-06 0.3379E-09	EQ3/6
Soddyite: $(UO_2)_2(SiO_4){:}2H_2O$	Soddyite + 4 H^+ = $SiO_2(aq)$ + 2 UO_2^{++} + 4 H_2O	5.74	Nguyen et al. 1992
Na-Boltwoodite $NaH_3OUO_2SiO_4{:}H_2O$	Na-Boltwoodite + 3 H^+ = Na^+ + $SiO_2(aq)$ + UO_2^{++} + $4H_2O$	5.82	Nguyen et al. 1992

*For spent fuel and schoepite, the listed numbers are the coefficients of the polynomial functions of temperature dependency. For example, log K^{eq} (schoepite) = 0.5656E+01 + (-0.3578E-01)*T + (0.1328E-03)*T^2 + (-0.3213E-06)*T^3 + (0.3379E-09) *T^4, where T is temperature in °C.

Table 6-43. Rate Constants of Solid Dissolution

	Spent Fuel	Schoepite	Soddyite	Uranophane	Na-boltwoodite*
K_0 (mol/m2-sec)	0.00137	6.3E+6	6.8E+8	5.56E+35	2.0E+12
E_a (J)	29697	0	0	0	0
K_1 (m/sec)	3.555E-8	416.94	8.93E+4	1.25E+32	1.94E+8
$\ln(K_1)$	-17.1537	6.033	49.989	73.905	19.08

*The rate constant for Na-boltwoodite is estimated from uranophane data.

Table 6-44. Equilibrium Reactions Considered in the Simulations

Aqueous Equilibrium Reactions	* Log K^{eq}
$H_2O = H^+ + OH^-$	-0.1494E+02 0.4171E-01 -0.1917E-03 0.4950E-06 -0.6159E-09
$CO_2(aq) + H_2O = H^+ + HCO_3^-$	-0.6576E+01 0.1198E-01 -0.1362E-03 0.4131E-06 -0.5483E-09
$HCO_3^- = H^+ + CO_3^{--}$	0.1062E+02 -0.1397E-01 0.1143E-03 -0.3352E-06 0.4687E-09
$HSiO_3^- + H^+ = SiO_2(aq) + H_2O$	0.1033E+02 -0.1707E-01 0.4438E-04 0.3611E-07 -0.9495E-10
$CaCO_3(aq) + H^+ = Ca^{++} + HCO_3^-$	0.7500E+01 -0.2156E-01 0.7888E-04 -0.1821E-06 0.8651E-10
$CaHCO_3^+ = Ca^{++} + HCO_3^-$	-0.1091E+01 0.3525E-02 -0.9368E-04 0.3085E-06 -0.4615E-09
$NaCO_3^- + H^+ = Na^+ + HCO_3^-$	0.9810E+01 -0.2859E-02 0.1433E-03 -0.3573E-06 0.3362E-09
$NaHCO_3(aq) = Na^+ + HCO_3^-$	-0.3675E+00 0.8192E-02 -0.9257E-06 -0.4679E-07 0.2168E-09
$NaCl = Na^+ + Cl^-$	0.8298E+00 -0.1559E-02 -0.2947E-04 0.1183E-06 -0.2367E-09
$NaHSiO_3(aq) + H^+ = Na^+ + SiO_2(aq) + H_2O$	0.8425E+01 -0.5331E-02 -0.2584E-04 0.2532E-06 -0.4395E-09
$UO_2(CO_3)_3^{----} + 3H^+ = UO_2^{++} + 3\ HCO_3^-$	0.9493E+01 -0.4015E-03 -0.5581E-04 0.1200E-06 -0.2995E-09

Table 6-44. Equilibrium Reactions Considered in the Simulations (Continued)

Aqueous Equilibrium Reactions	* Log K^{eq}
$UO_2(CO_3)_2^{--} + 2H^+ = UO_2^{++} + 2\ HCO_3^-$	0.4492E+01 -0.3047E-01 0.4683E-04 -0.7901E-07 -0.7331E-10
$UO_2(CO_3)\ (aq) + H^+ = UO_2^{++} + HCO_3^-$	0.9531E+00 -0.1163E-01 -0.3975E-08 0.8229E-07 -0.3169E-09
$UO_2(OH)_3^- + 3H^+ = UO_2^{++} + 3H_2O$	19.2227
$UO_2(OH)_2\ (aq) + 2H^+ = UO_2^{++} + 2H_2O$	10.3155
$UO_2(OH)^+ + H^+ = UO_2^{++} + H_2O$	0.5910E+01 -0.3035E-01 0.1067E-03 -0.2529E-06 0.2606E-09
$Np(OH)_{4(aq)} + H^+ = Np(OH)_3^+ + H_2O$	3.8000
$Np(OH)_5^- + H^+ = Np(OH)_{4(aq)} + H_2O$	4.7000
$NpO_2^{++} + 4\ H_2O = Np(OH)_5^- + 3H^+ + 0.5O_2(aq)$	-24.0615
$NpO_2(OH)^+ + H^+ = NpO_2^{++} + H_2O$	5.2000
$NpO_2(CO_3)_2^{--} + 2H^+ = NpO_2^{++} + 2\ HCO_3^-$	6.6576
$NpO_2(CO_3)_3^{----} + 3H^+ = NpO_2^{++} + 3\ HCO_3^-$	10.5864
$NpO_2(OH)\ (aq) + H^+ = NpO_2^+ + H_2O$	8.9000
$NpO_2(CO_3)^- + H^+ = NpO_2^+ + HCO_3^-$	5.7288
$NpO_2(CO_3)_2^{---} + 2H^+ = NpO_2^+ + 2\ HCO_3^-$	13.6576
$NpO_2^+ + 3.5\ H_2O = Np(OH)_5^- + 2H^+ + 0.25O_2(aq)$	-24.1683
$NpO_2(CO_3)_3^{----} + 3H^+ = NpO_2^+ + 3\ HCO_3^-$	22.4864
Gaseous-Aqueous Equilibrium Reactions	
$CO_2(g) + H_2O = H^+ + HCO_3^-$	-0.7676E+01 -0.4984E-02 -0.2707E-04 0.1083E-06 -0.2044E-09
$O_2(g) = O_2(aq)$	2.660 0.1142E-1 -0.9291E-4 0.2735E-6 -0.3402E-9

*The numbers under the column of log K^{eq} are the polynomial coefficients of equilibrium constants as a function of temperature. Please see the footnote of Table 6-42.

Table 6-45. Inventory and U:Np Ratio

	Grams/MTIHM*	Moles/MTIHM
^{237}Np	4.18E+2	1.764
^{241}Pu	7.097E+2	2.945
^{241}Am	4.701E+2	1.951
U	9.598E+5	4032.20
237Np (Lumped)		6.66
U:237Np	4032.2 :6.66 = 1 : 0.0016	

*MTIHM = metric tons initial heavy metal

Table 6-46. Eight Cases of Simulation from the Possible Combinations of Scenarios, Hypotheses, and Conditions

Conditions	Initial Amount of Schoepite (Cladding Failure)	Scenario-1 (Np not into tertiary minerals)	Scenario-2 (Np into tertiary minerals)
Condition-1	4.13% (11%)	Case-1	Case-5
(Period E)	0.38% (1%)	Case-2	Case-6
Condition-2	4.13% (11%)	Case-3	Case-7
(Period-F)	0.38% (1%)	Case-4	Case-8

Table 6-47. Base Case Parameters for EBS Transport Model

Process	Parameter	Values/Variable name	Implementation/Reference
WP/EBS design	WP length	5.335 m (SF), 5.37 m (HLW)	WP design/ Table 3-26
	WP diameter	1.664 m (SF), 1 m (HLW)	WP design/ Table 3-26
	WP inner barrier thickness	2 cm	WP design/ Table 5-1
	WP outer barrier thickness	10 cm	WP design/ Table 5-1
	Invert thickness	0.855 m	Repository design/ Table 3-24
WP/EBS materials	WP inner barrier material	Alloy-22	WP design/Section 5.1.2
	WP outer barrier material	Carbon steel	WP design/Section 5.1.2
	Invert material	Precast concrete	Repository design/ Section 4.3.1.2
In-drift water dripping	Volume of water dripping on a single package, f(t, r,e,perc)*	QDRIP#	Drift-scale UZ-flow seepage abstraction/ Table 2-40 for percolation flux, Tables 2-55 and 2-56 for seepage volume
	Fraction of packages in given dripping environment, f(t, r,e, perc)	Mean = FMN$# S.D. = FSD$#	Drift-scale UZ-flow seepage abstraction/ Table 2-40 for percolation flux, Tables 2-55 and 2-56 for seepage fraction
Dripping through WP	WP failure history, f(t, r,e)	WPFAIL	WP degradation abstraction/ DTN MO9810SAP00013.000
	WP average number of patch penetrations per failed waste package, f(t, r,e)	PATNUM	WP degradation abstraction/ DTN MO9810SAP00013.000
	WP average number of pit perforations per failed waste package, f(t, r,e)	PITNUM	WP degradation abstraction/ DTN MO9810SAP00013.000
	Fraction of in-drift drips entering package f(t, r,e)	QPAT#, QPIT#	Function of number of patches and pits through package from WP degradation abstraction, Section 6.5.2.2
	Volume of water in WF cell	vwdsf,vwhlw,vwsf	WF degradation abstraction, (see note 1)
Chemistry of incoming water	pH, CO_3, ionic strength f(t)	PH&, C&, ICOL&	NFGE abstraction/Table 4-44
Waste form degradation	SF degradation rate, f(T, pH, CO_3)	SF degradation model	WF abstraction/Section 6.3.1.3.2

Table 6-47. Base Case Parameters for EBS Transport Model (Continued)

Process	Parameter	Values/Variable name	Implementation/Reference
	DHLW degradation rate, f(T, pH, SiO_2)	DHLW degradation model	WF abstraction/Section 6.3.3.3
Diffusive transport from waste form through corrosion products and degraded concrete in the vicinity of the WP	RN concentrations at WF surface	Calculated by RIP (solubility limited RNs; alteration-limited RNs)	RIP Output
	Sorption of RNs in degraded WF and WP basket materials	Not included	EBS transport abstraction conservative assumption
	Pit radius	.00035m	WP degradation abstraction assumption
	Patch area	310 cm^2	WP degradation abstraction/Section 5.12.2.3
	Liquid saturation of corrosion products in perforations	0.998	Drift-scale T-H model/Figure 3-50f
	Diffusion coefficient in corrosion products	Fitted to Conca's data f(porcor,satcor)	EBS transport abstraction, CRWMS M&O 1998e
	Porosity of corrosion products	0.4	EBS transport abstraction assumption
	Sorption of RNs in corrosion products	Not included	EBS transport abstraction conservative assumption
Diffusive transport through invert	Porosity of degrading precast concrete	Porinv=0.1	Drift-scale T-H model/Table 3-20
	Liquid saturation of degrading precast concrete	0.998	Drift-scale T-H model/Figure 3-50f
	Diffusion coefficient of RNs in degrading precast concrete	Fitted to Conca's data f(satinv, porinv)	EBS transport abstraction, CRWMS M&O 1998e
	Sorption of RNs in degrading precast concrete	KDRNIN, where RN is radioactive element	EBS transport abstraction, Section 6.5.2.2

* f(t,r,e, perc) function of time, region, environment, and percolation

is **1..6** for 6 regions,

$ is **D**, **L**, or **S** the three dripping environments: D for dripping during the dry climate and all wetter climates, L for dripping during the long term average and wetter climates, and S for dripping only during the super pluvial climate.

& is for the 7 time periods (in years): **1)** 0–200, **2)** 200–1,000, **3)** 1,000–2,000, **4)** 2,000–4,000, **5)** 4,000–10,000, **6)** 10,000–100,000, **7)** 100,000–1,000,000.

1 Volume of water in WF cell calculated using: initial volume of WF * WF degradation rate * time * saturation of rind * porosity of rind, where saturation was assumed 1.0, and porosity was assumed 0.4.

CHAPTER 6
FIGURES

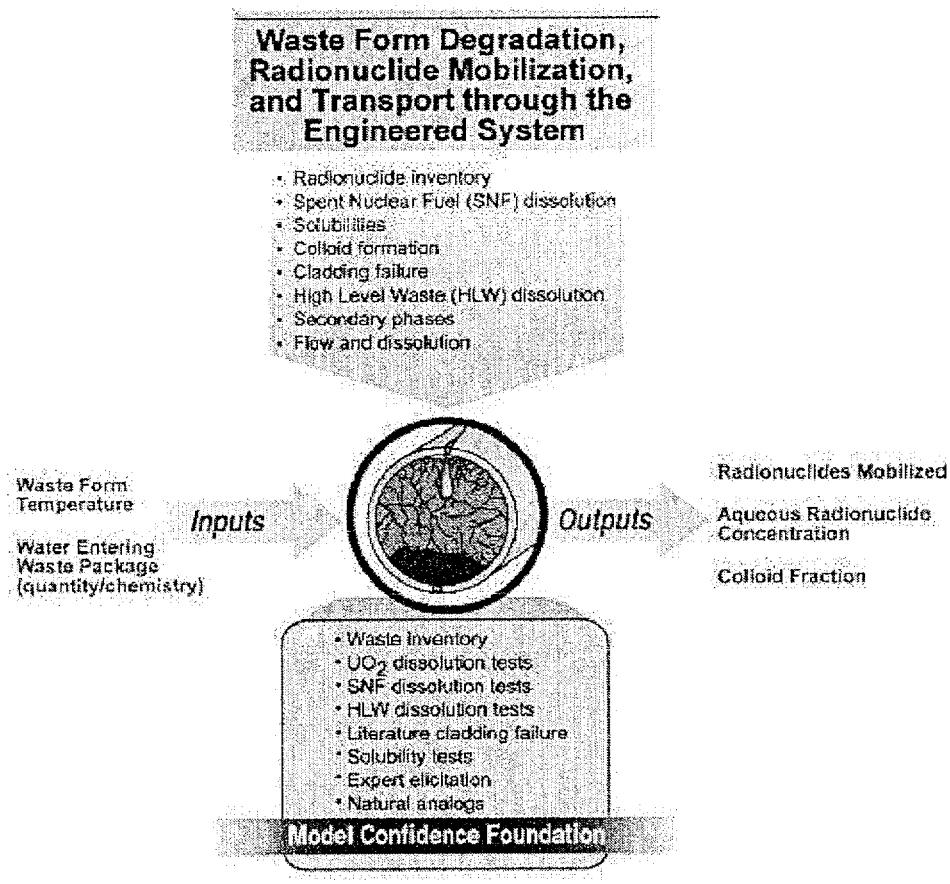

Figure 6-1. Waste Form Degradation, Radionuclide Mobilization and Transport Through the Engineered Barrier System

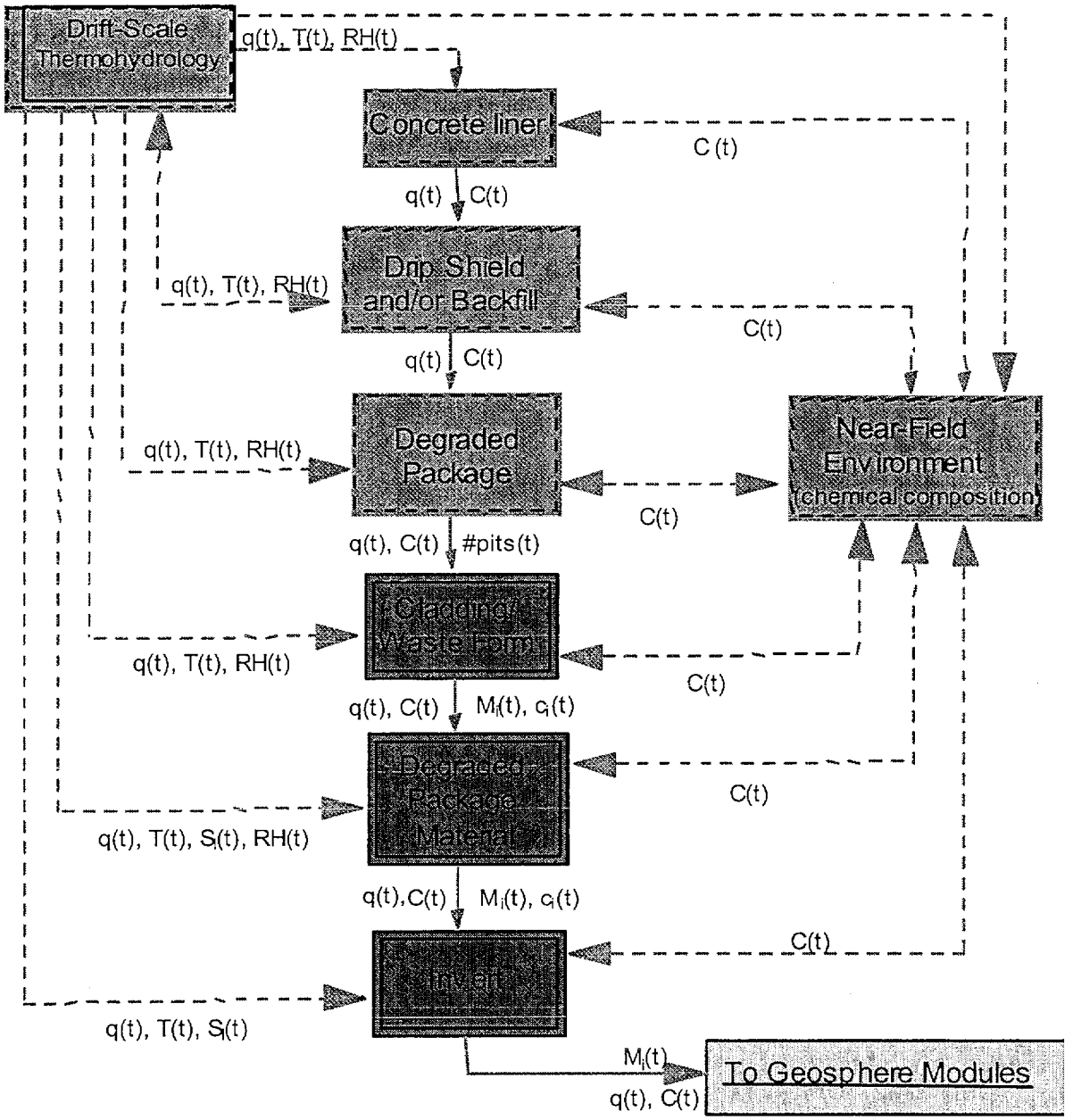

Figure 6-2. EBS Model Architecture

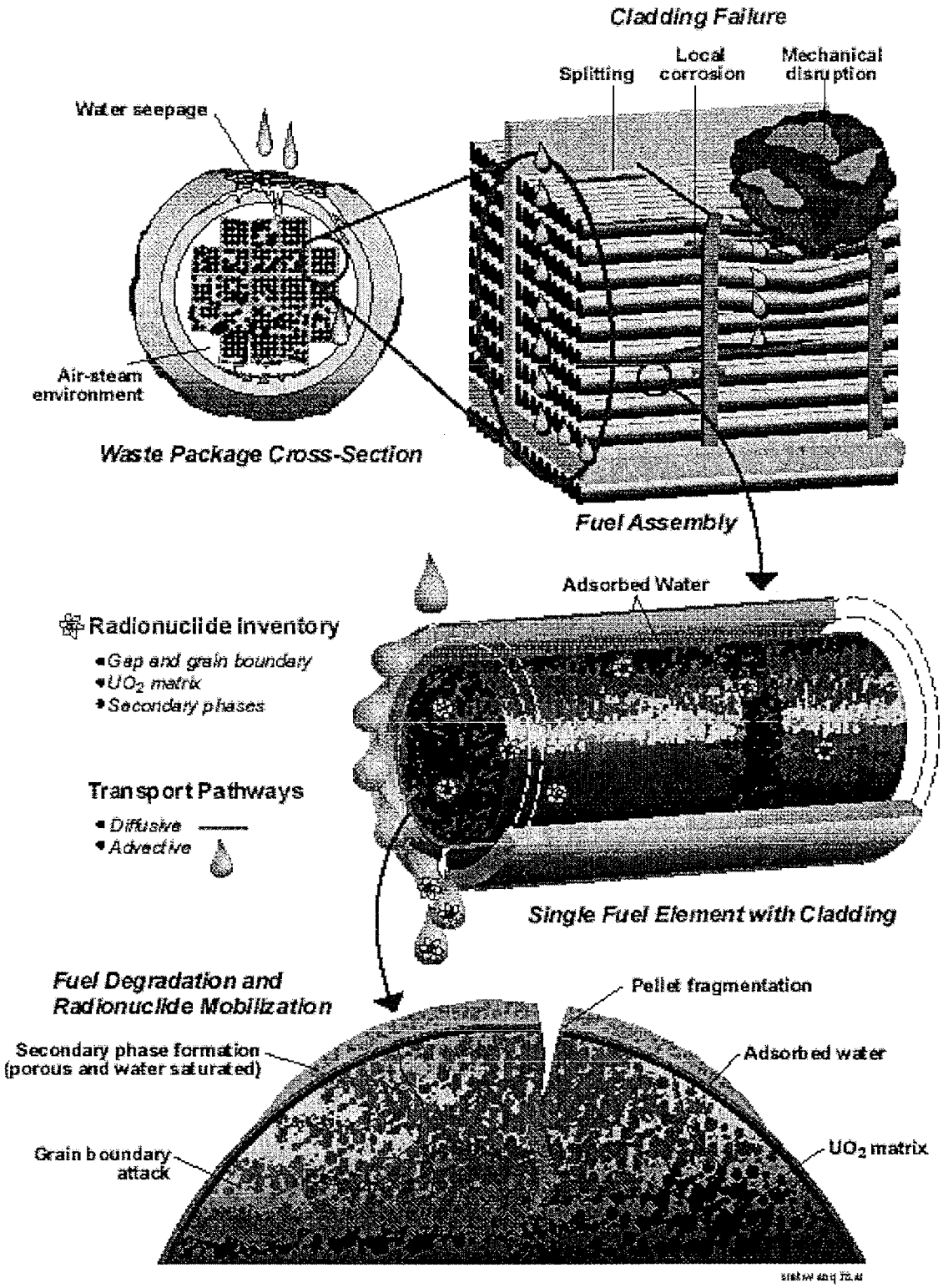

Figure 6-3. Schematic of Waste Form/Waste Package/Engineering Barrier System

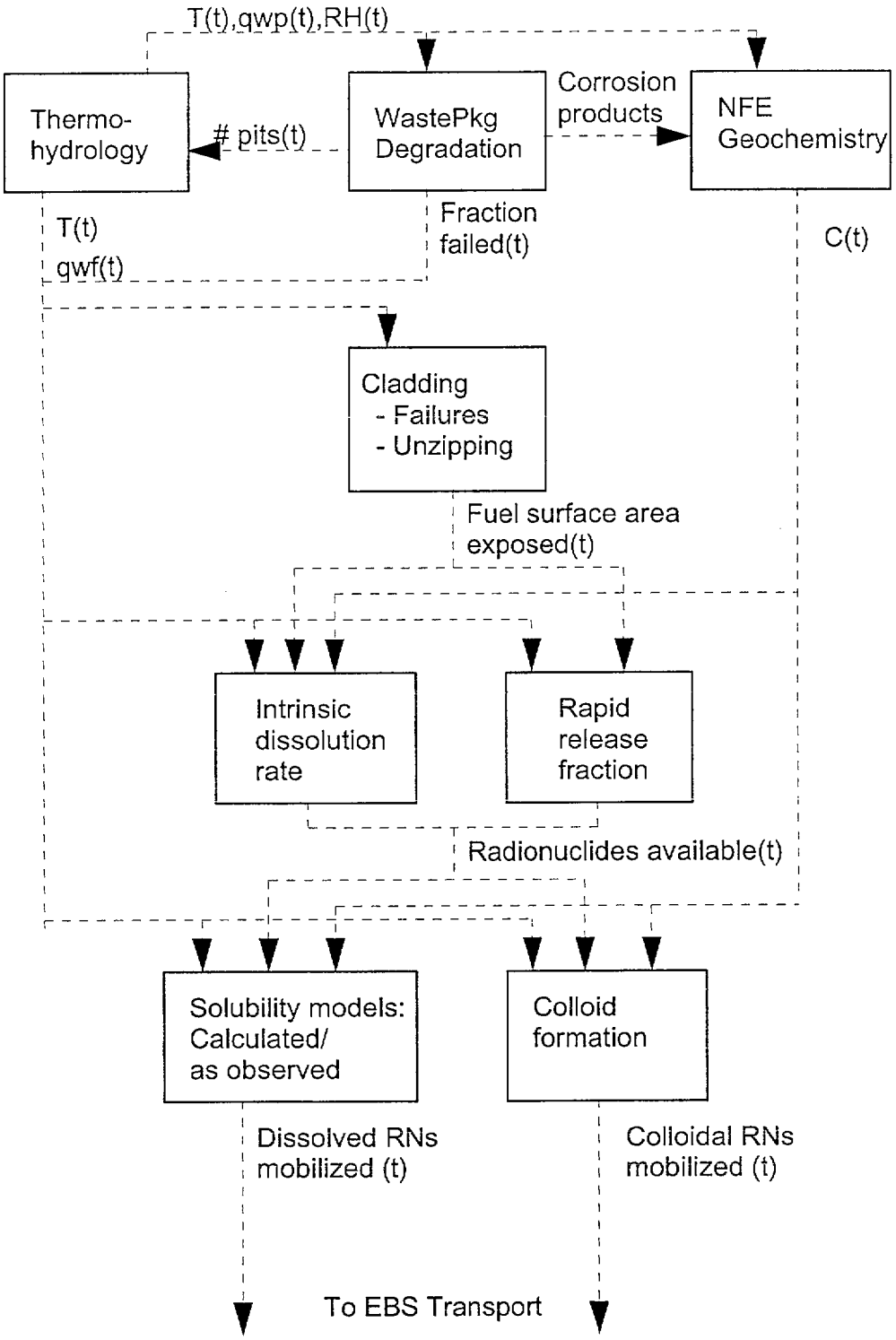

Figure 6-4. CSNF Degradation/Radionuclide Mobilization Process Flow

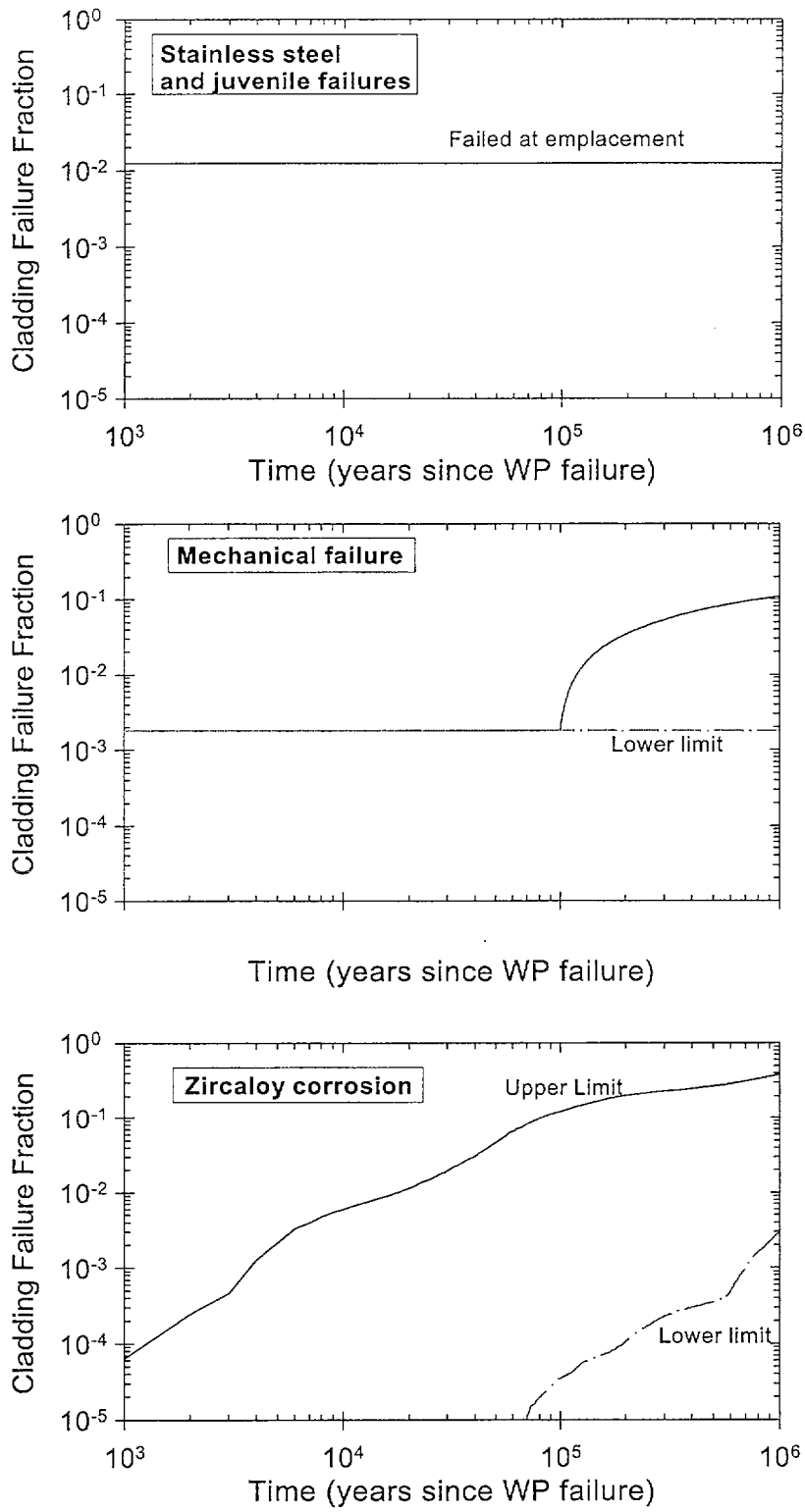

Figure 6-5. TSPA-VA Cladding Abstraction

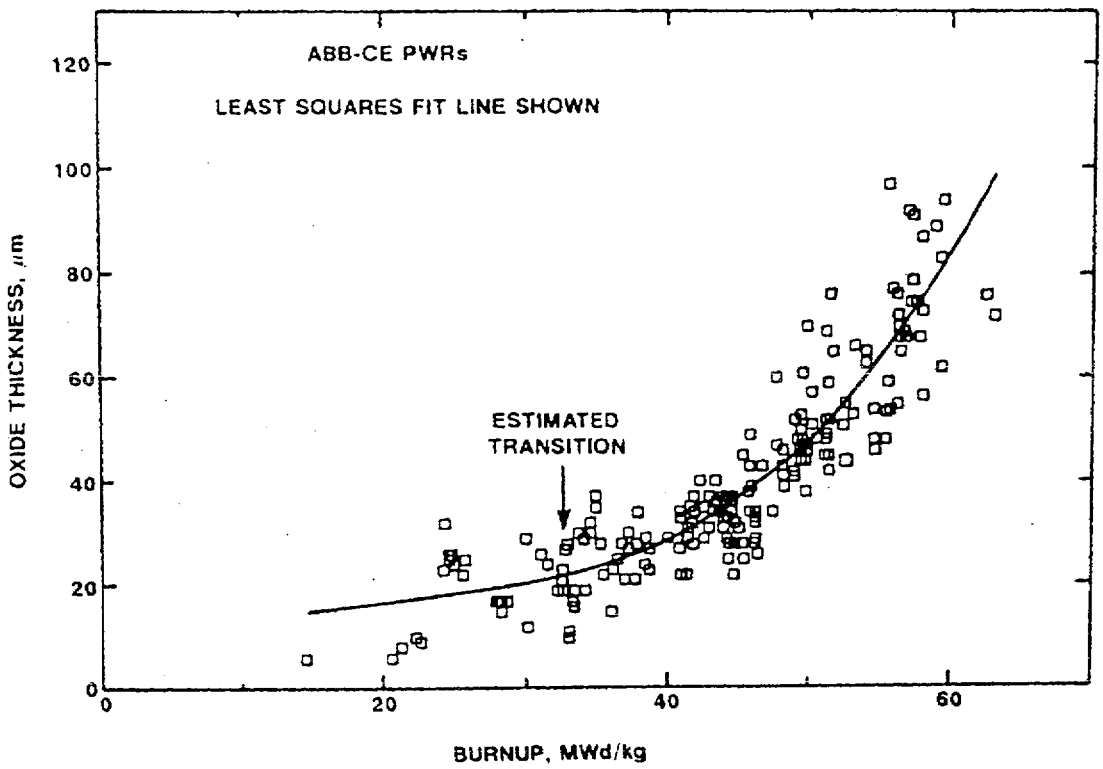

Figure 6-6. Cladding Oxide Thickness vs. Burnup
From: A.M. Garde, "Enhancement of Aqueous Corrosion of Zircaloy-4 due ot Hydride Precipitation at Metal-Oxide Interface," ASTM STP 1132, 1991, p. 583.

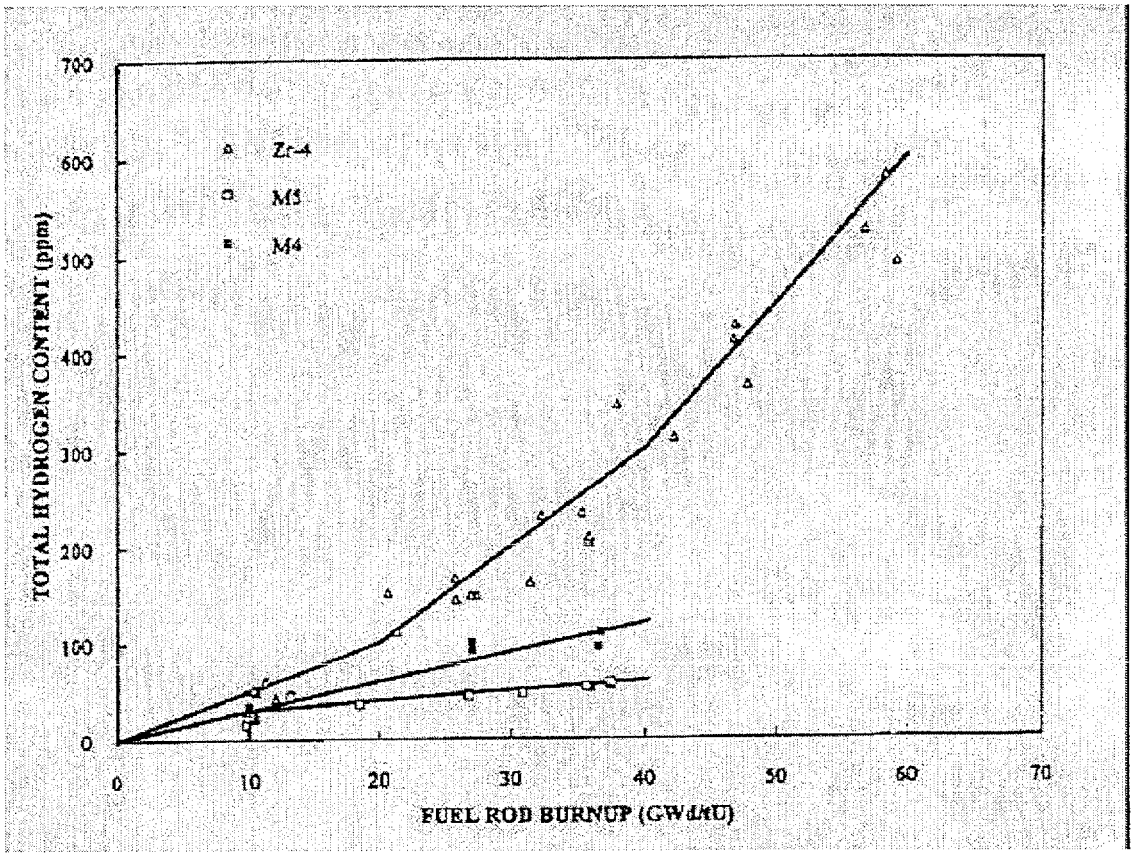

Figure 6-7. Total Hydrogen Content for Cladding vs. Burnup
From J. P. Mardon et al. "Update on the Development of Advanced Zirconium Alloys for PWR Rod Claddings," ANS Proceedings, 1997 Topical meeting on LWR Fuel Performance, Portland, OR, March 2-6, 1997, p. 408.

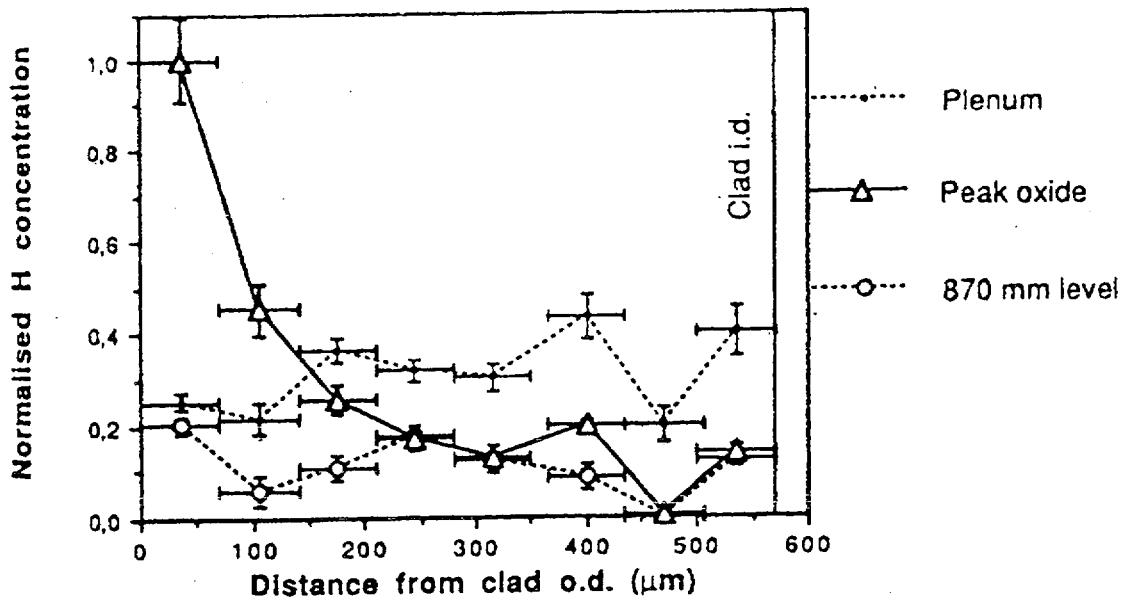

Figure 6-8. Cladding Radial Hydrogen Profiles
From: D.I. Schrire, J.H. Pearce, "Scanning Electron Micropscope Techniques for Studying Zircaloy Corrosion and Hydriding," Zirconium in the Nuclear Industry: Tenth International Symposium, ASTM STP 1245, A.M. Garde and E.R. Bradley, Eds, American Society for Testing and Materials, Philadelphia, 1994, pp. 98-115.

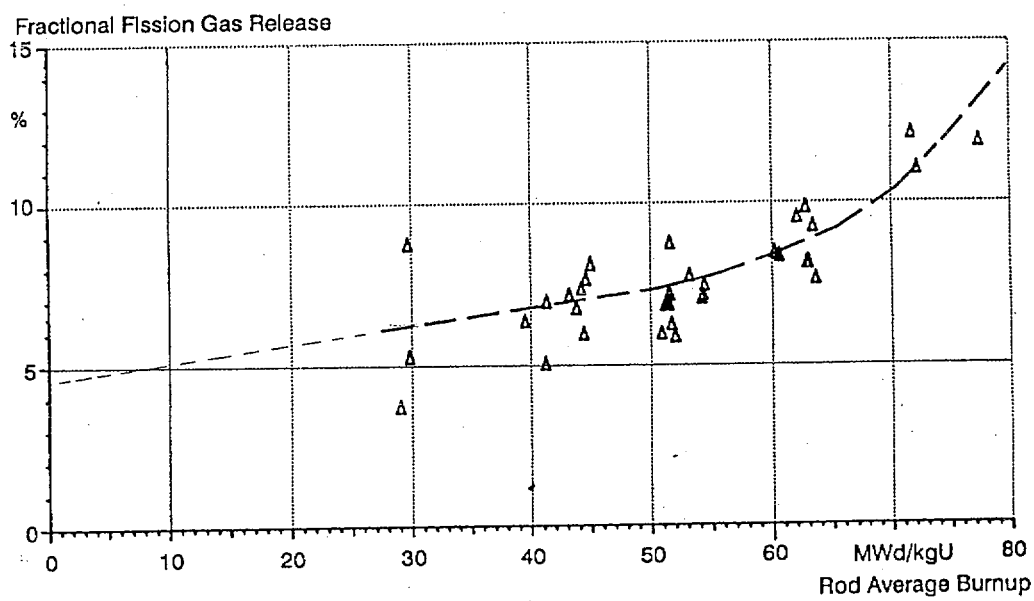

Figure 6-9. Fractional Fission Gas Release for PWR Fuel as a Function of Burnup
From: R. Manzel, M. Coquerelle, "Fission Gas Release and Pellet Structure at Extended Burnup," ANS Proceedings, 1997 International Topical Meeting on LWR Fuel Performance, Portland, OR, March 2-6, 1997, pp. 465.

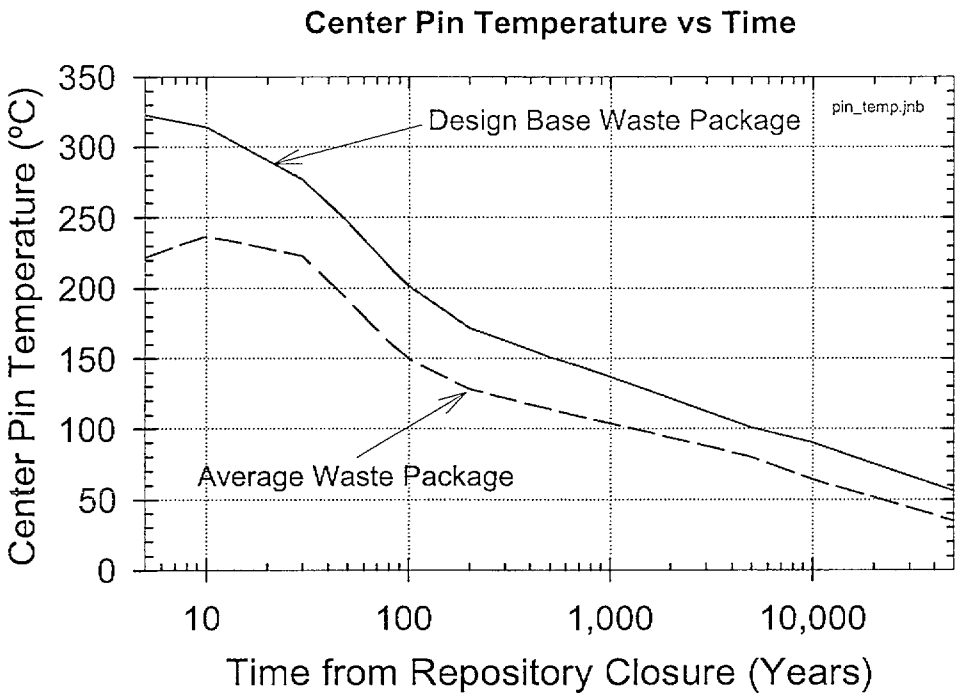

Figure 6-10. Center Pin Temperature vs. Time

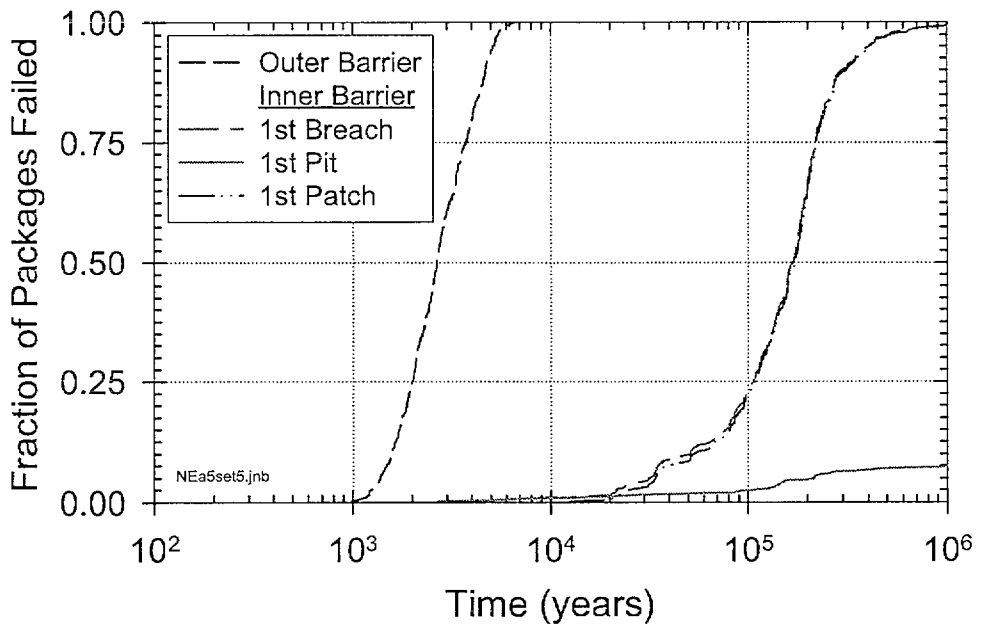

Figure 6-11. Base-Case Waste Package Failure

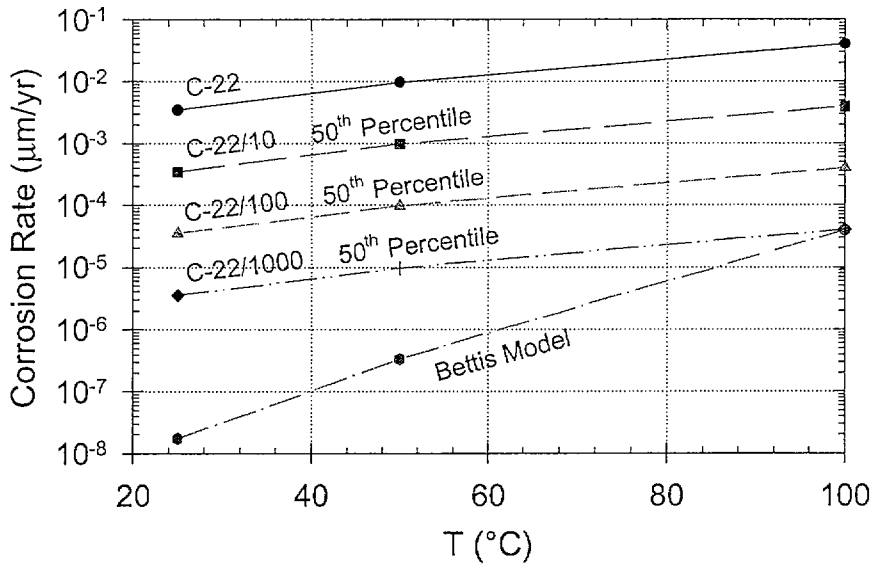

Figure 6-12. WAPDEG Corrosion Rate Used for Cladding Corrosion
Calculated using 1/10, 1/100 and 1/1000 of the corrosion rate of Alloy C-22 as surrogate Zircaloy corrosion rates.

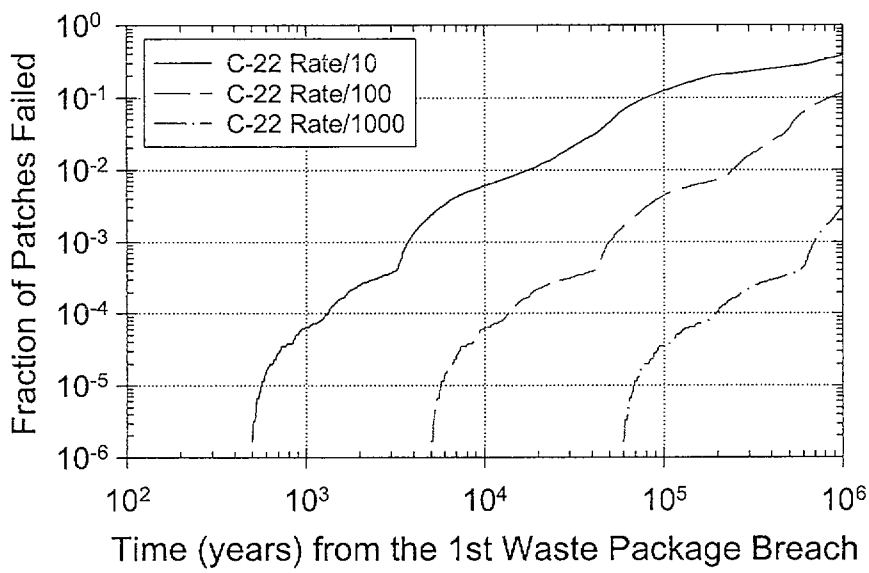

Figure 6-13. Fraction of Fuel Exposed from Zircaloy Clad Corrosion

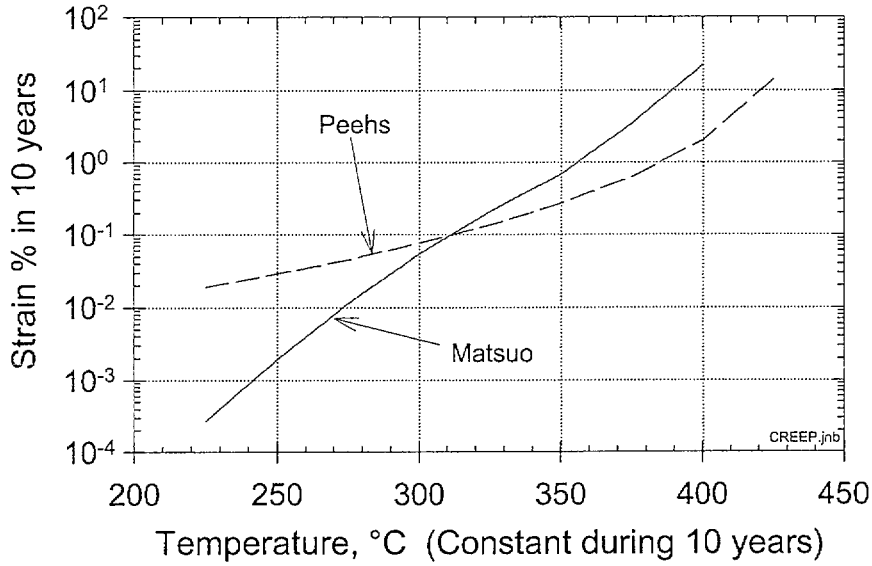

Figure 6-14. Comparison of Creep Correlations from Peehs and Fleisch 1986 and Matsuo 1987 at Constant Temperature

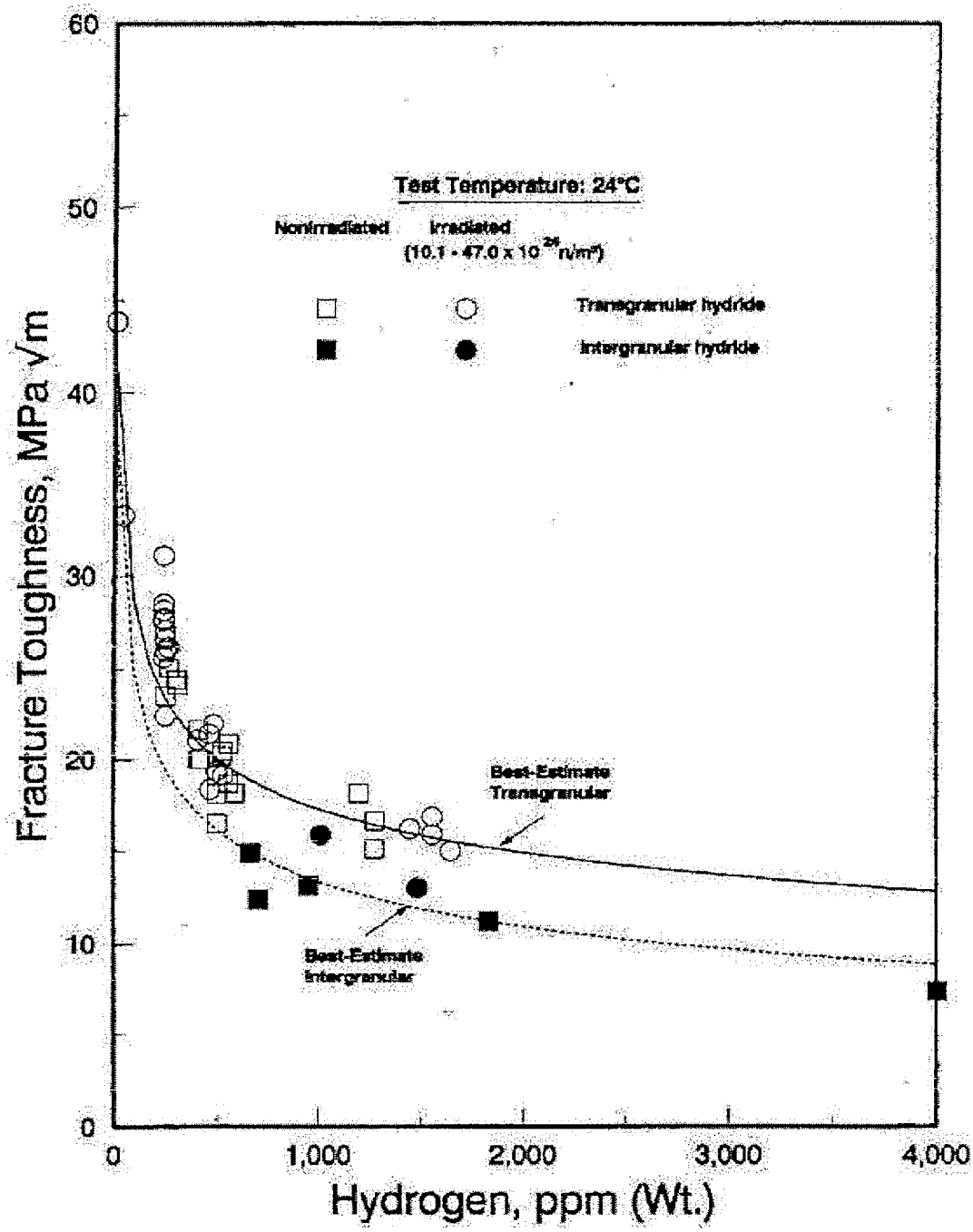

Figure 6-15. Fracture Toughness vs. Hydrogen Content of Zircaloy-4 from Kreyns et al. 1996

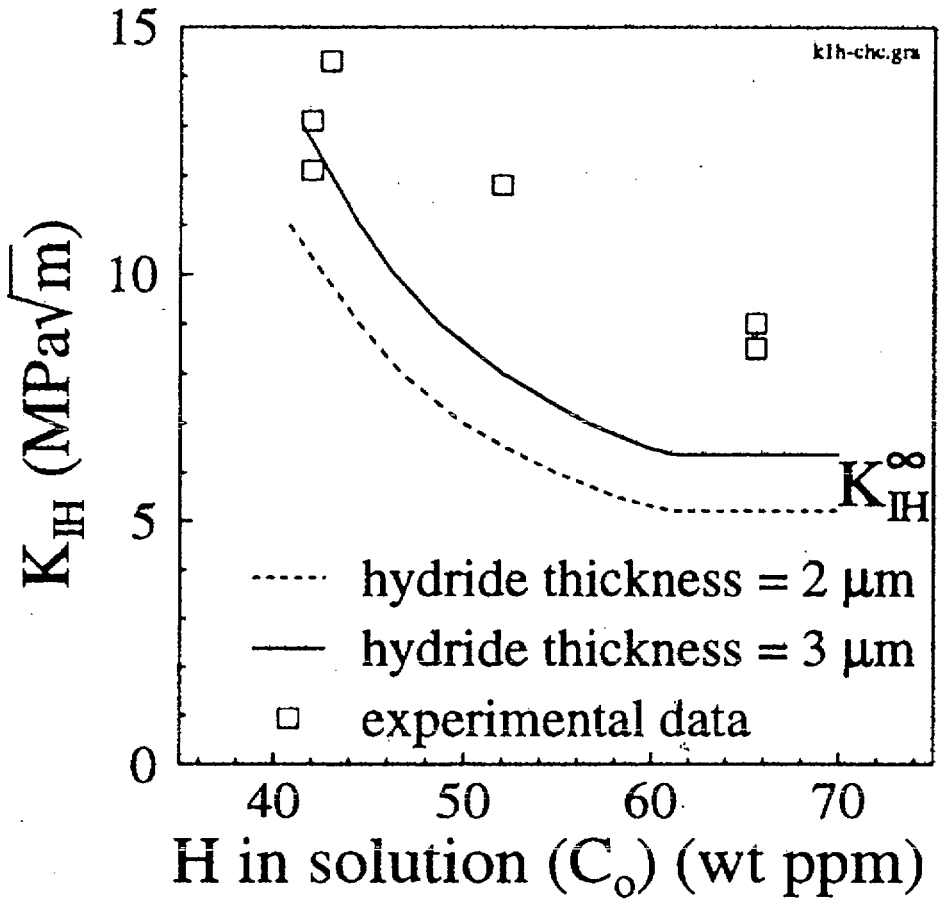

Figure 6-16. K_{IH} as a Function of Hydrogen in Solution
Lines: theory predictions from Shi and Puls 1996.

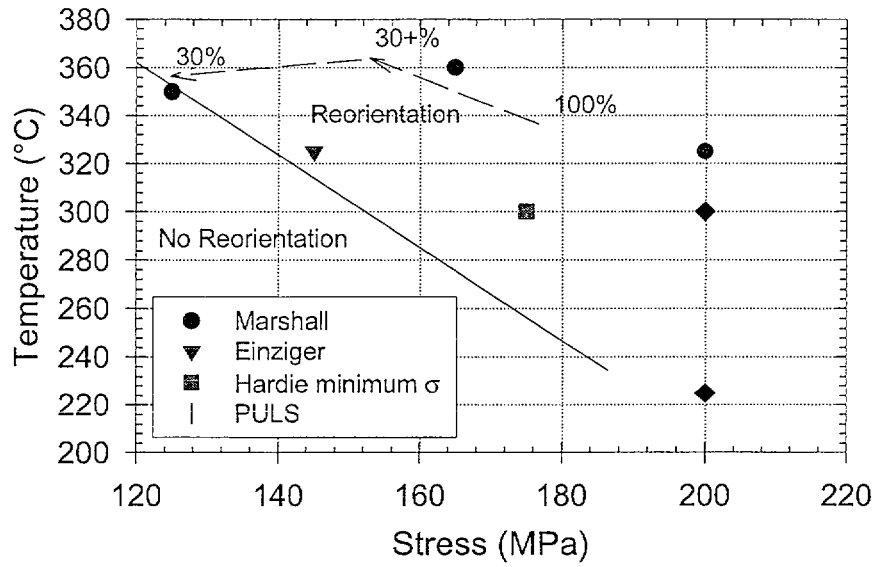

Figure 6-17. Temperature and Stress at Which Hydrogen Reorientation was Observed for Cold Worked Zirc-2, 4
[Pescatore et al. 1989].

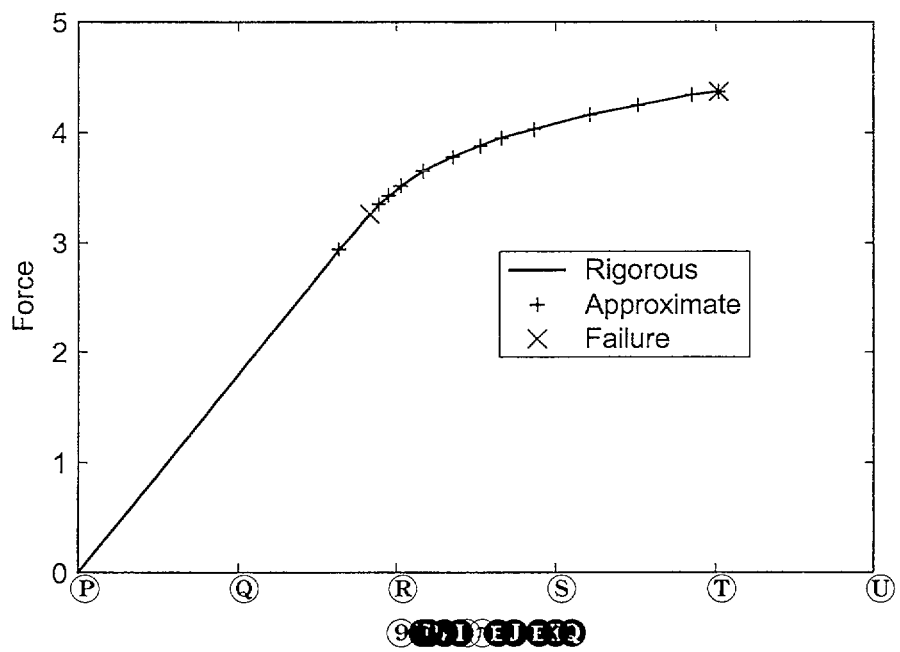

Figure 6-18. A Comparison of the Empirical Equation, Equations 6-10 and 6-11, and the Exact Treatment for the Force-Displacement Relationship Using Standard Elastic-Plastic Beam Theory (see Text)

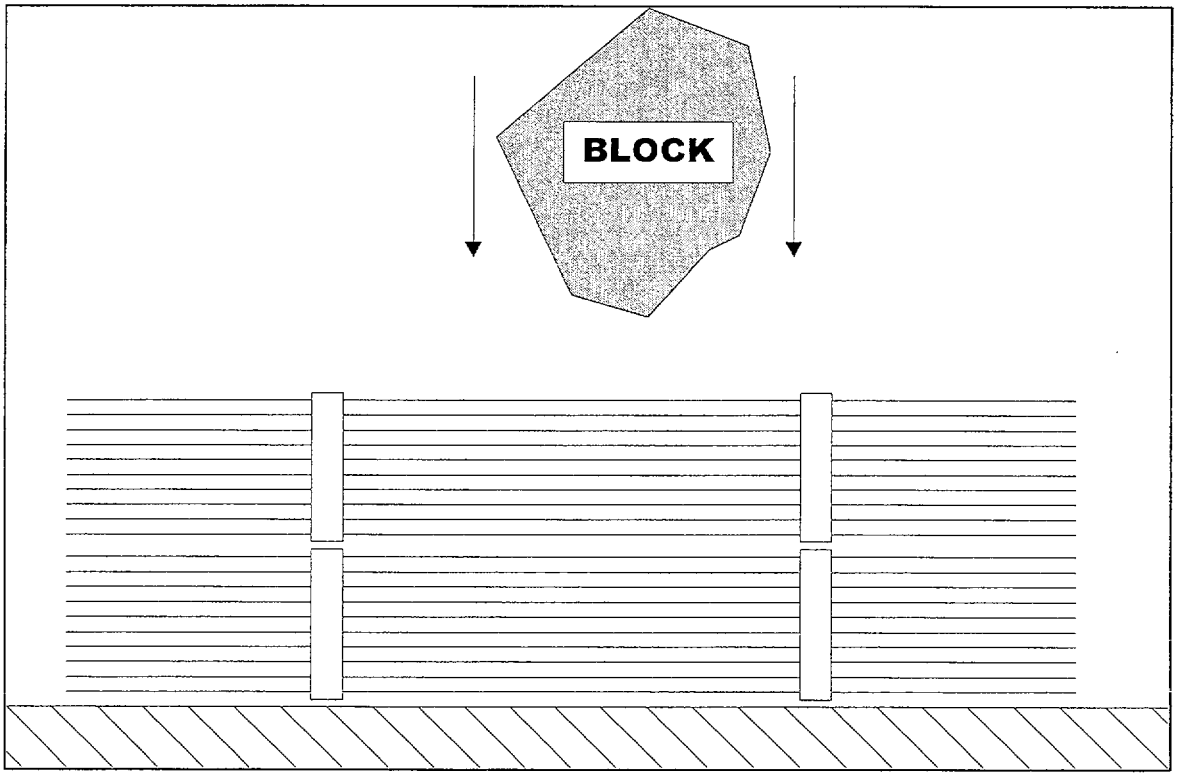

Figure 6-19. A Sketch of the Simplified Conceptual Model of the Mechanical Damage Process
Due to ultimate failure of a waste package, a rock block falls on the center of an assembly of rods, which is modeled as a continuum in its force-displacement and energy absorption behavior. The shape of the block is idealized later. The distribution of possible block sizes is discussed in the text.

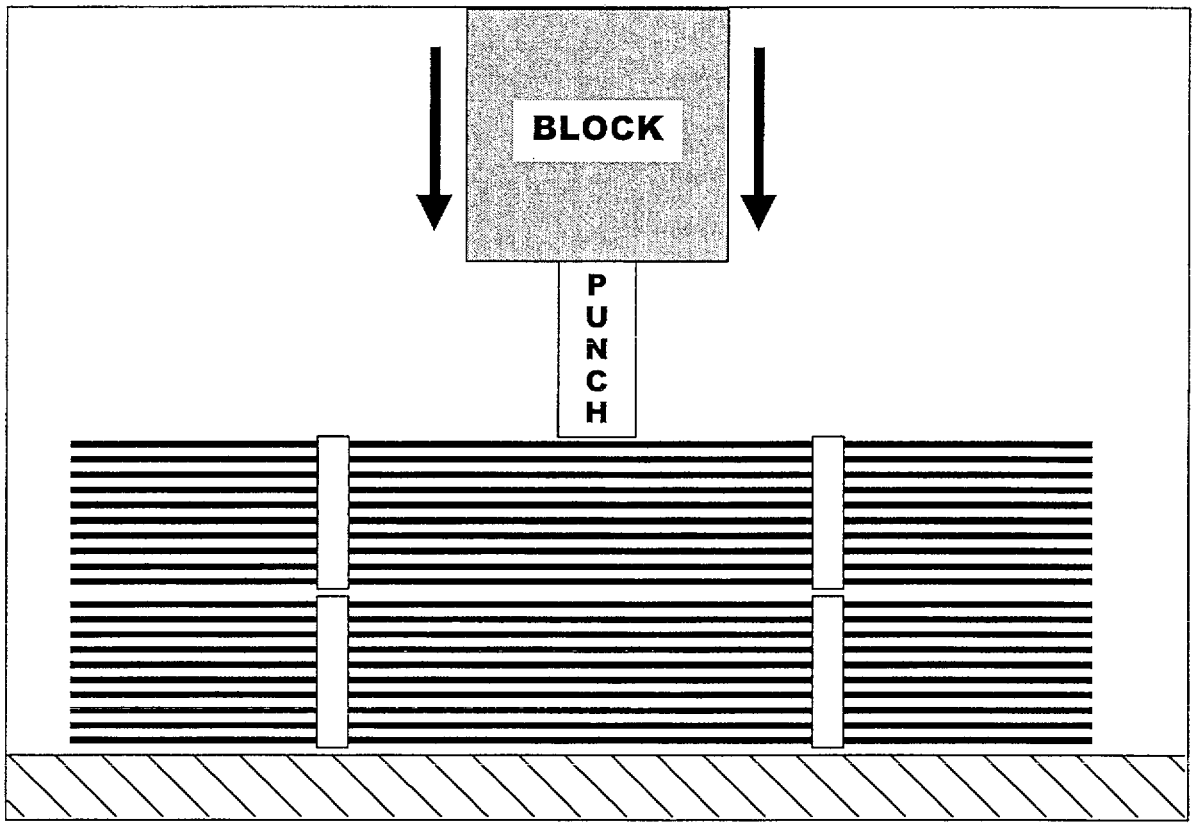

Figure 6-20. Schematized Geometry of a Block and its Impact
The axes of the blocks are taken to be vertical, and the blocks are assumed to fall freely from the former waste package surface onto the fuel assemblies. See Fig. 6-21 for more detail on the punch shapes.

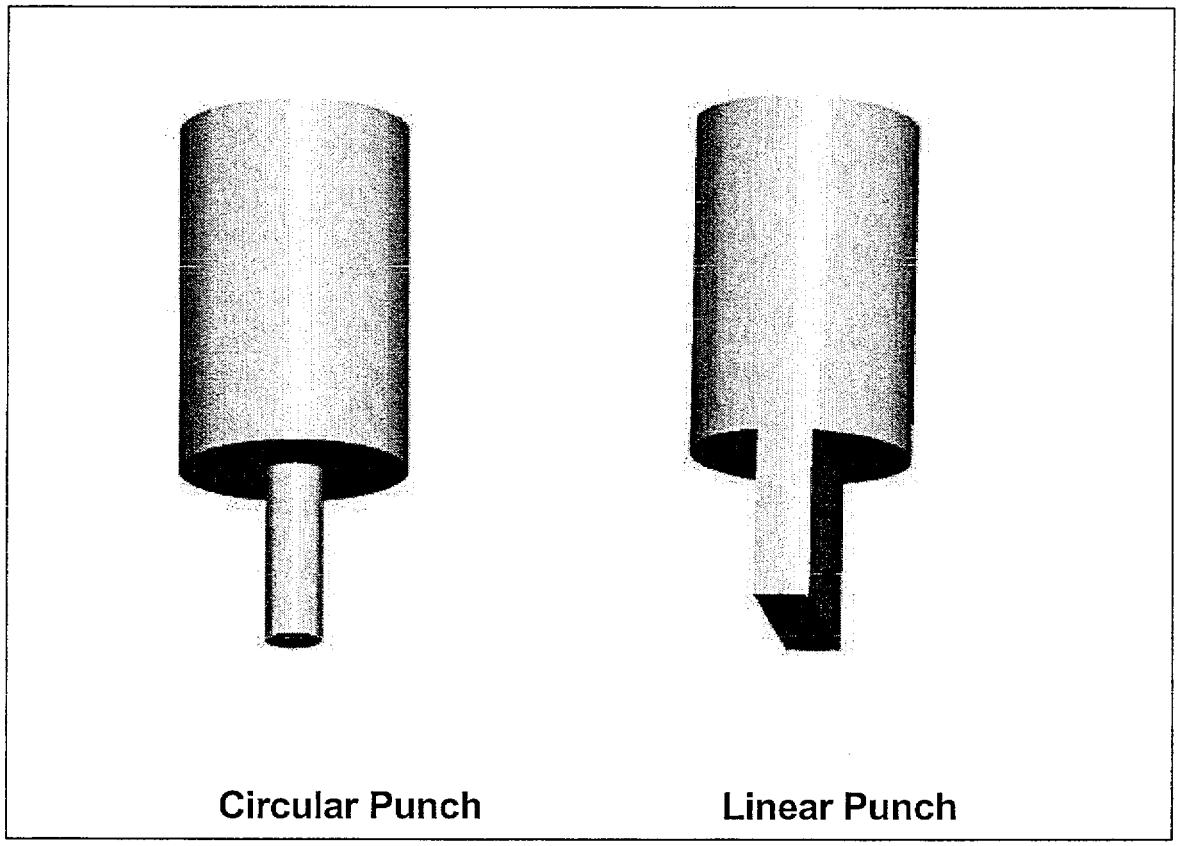

Figure 6-21. Two Types of Punches are Considered
For a circular punch, the focusing parameter is the ratio of the diameter of the punch to the diameter of the block. In a linear punch, two parallel chords of equal length and the two block-edge arcs that connect them define the outline of the punch. The focusing parameter is then defined as the ratio of the distance between the two chords to the diameter of the block.

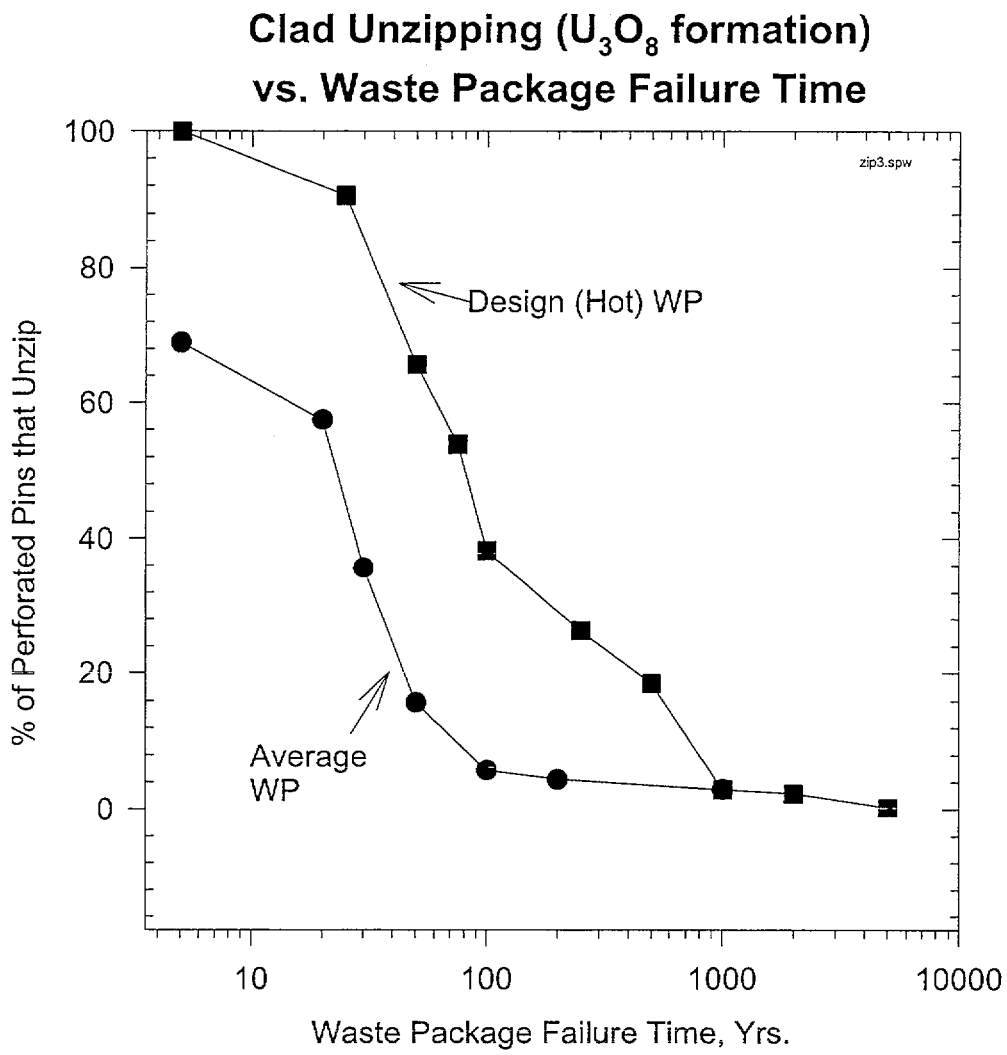

Figure 6-22. Clad Unzipping vs. Waste Package Failure Time

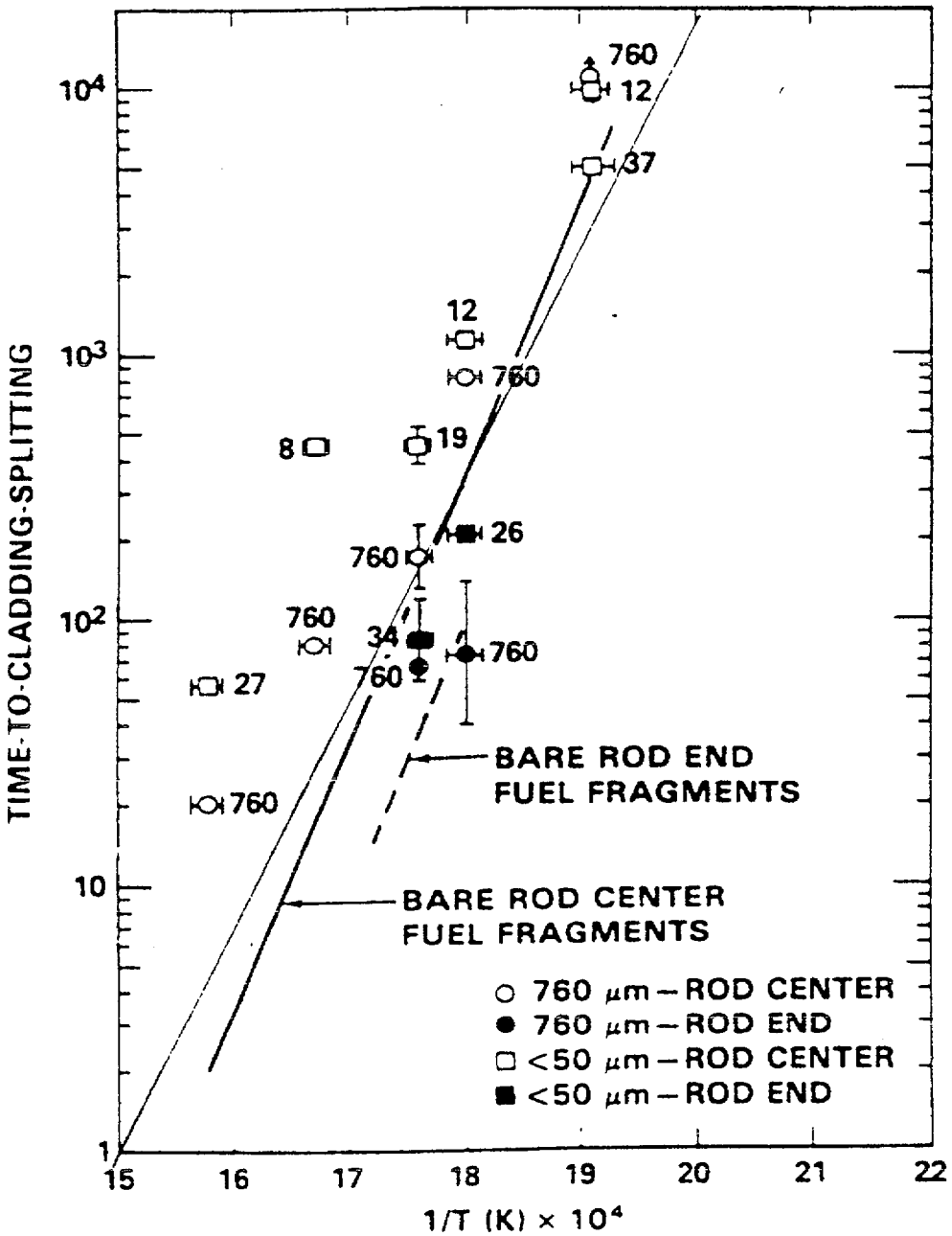

Figure 6-23. Time-to-Cladding-Splitting (in Hours) from Einziger and Strain (1986), with a More General Proposed Fit Added (the Longer, Lesser-Slope Line)
The new fit uses a Q value from other experiments, and is a best-estimate fit to both rod-end and rod-center data combined. The original fits (shorter lines) were intended to be lower-bound fits for the data sets, treating rod-end and rod-center data groups separately.

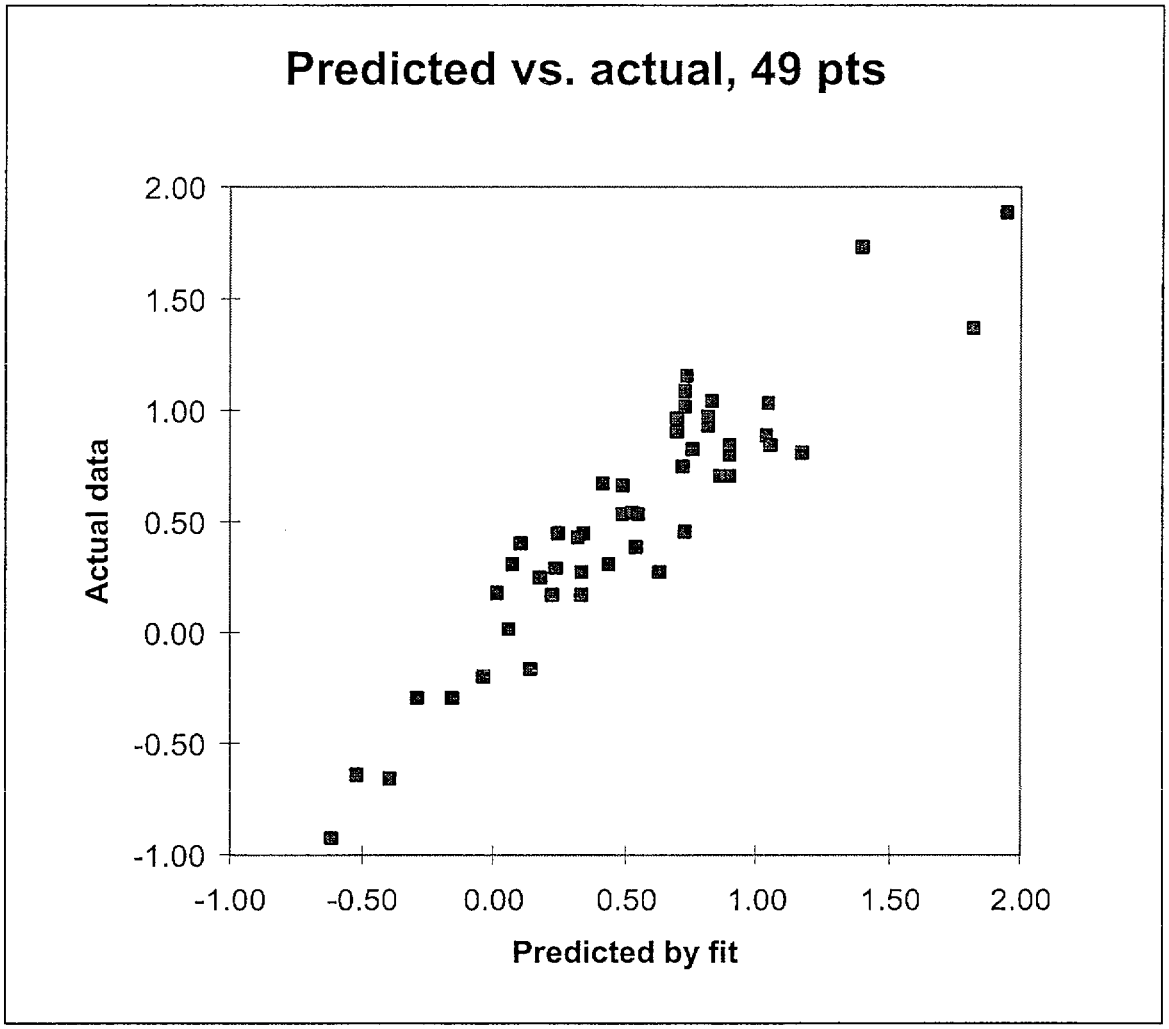

Figure 6-24. Log/Log Comparison of the CSNF Dissolution Rate Input Data (Experimentally Measured) with the Calculated Dissolution Rate Predicted by the Fitted Function, Using All the Spent Fuel and UO_2 Data

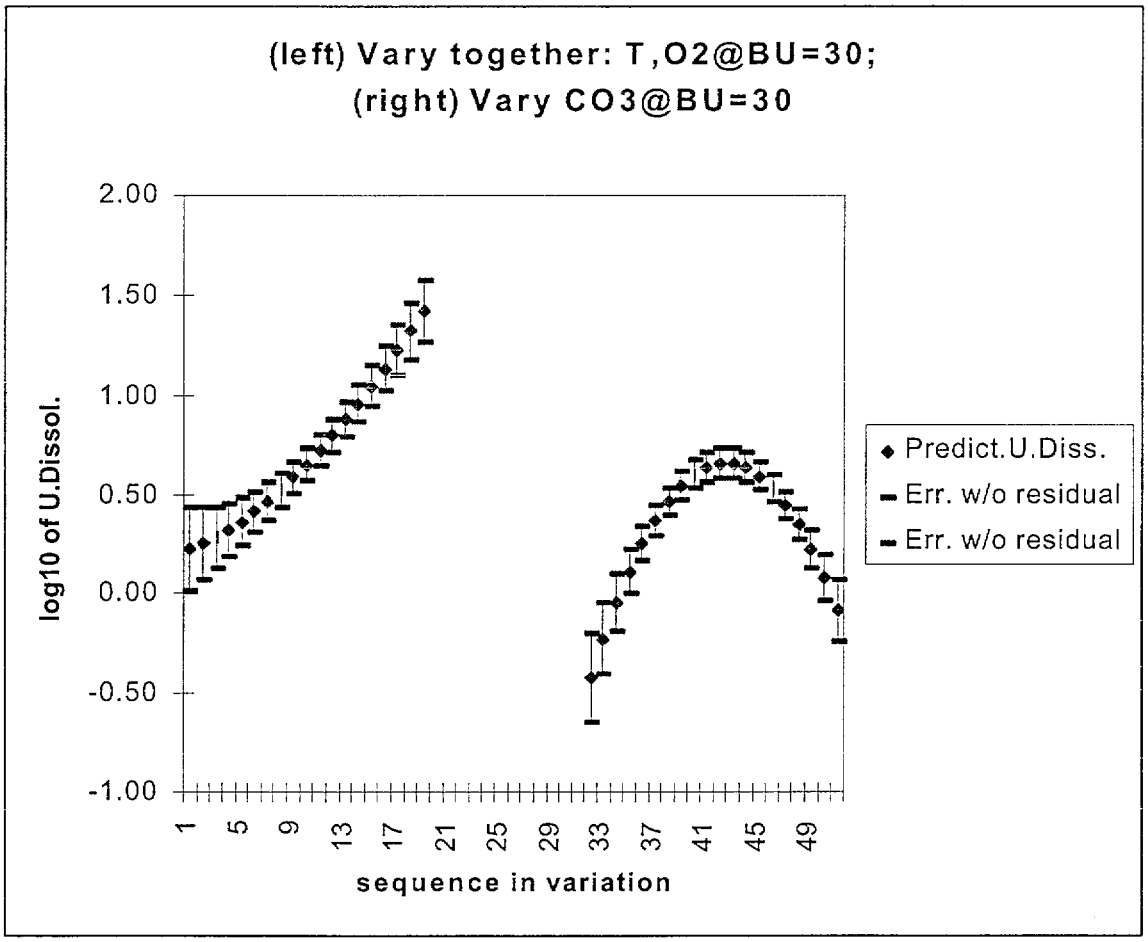

Figure 6-25. Error Bars for Two Typical Data Series Through the Span of Data Covered by the Fitting Data and Extending Beyond the Fitting Data; Errors in the Coefficients, i.e., Fitting Errors, Only
On the left: increasing temperature, range 5 to 95°C (experimental range 25 to 75°C); increasing O2, range 0.1% to 40% with a logarithmic spacing of intermediate values (experimental range 0.3% to 20%); burnup = 30 MW-days/kgU; other parameters near their logarithmic averages for the data set, specifically pH = 9, CO3 = 2 mmol/l. On the right: increasing CO3, range 0.05 to 80 mmol/l % with a logarithmic spacing of intermediate values (experimental range 0.2 to 20 mmol/l); burnup = 30 MW-days/kgU; other parameters near their logarithmic averages for the data set, specifically T = 50°C, pH = 9, O2 = 2%.

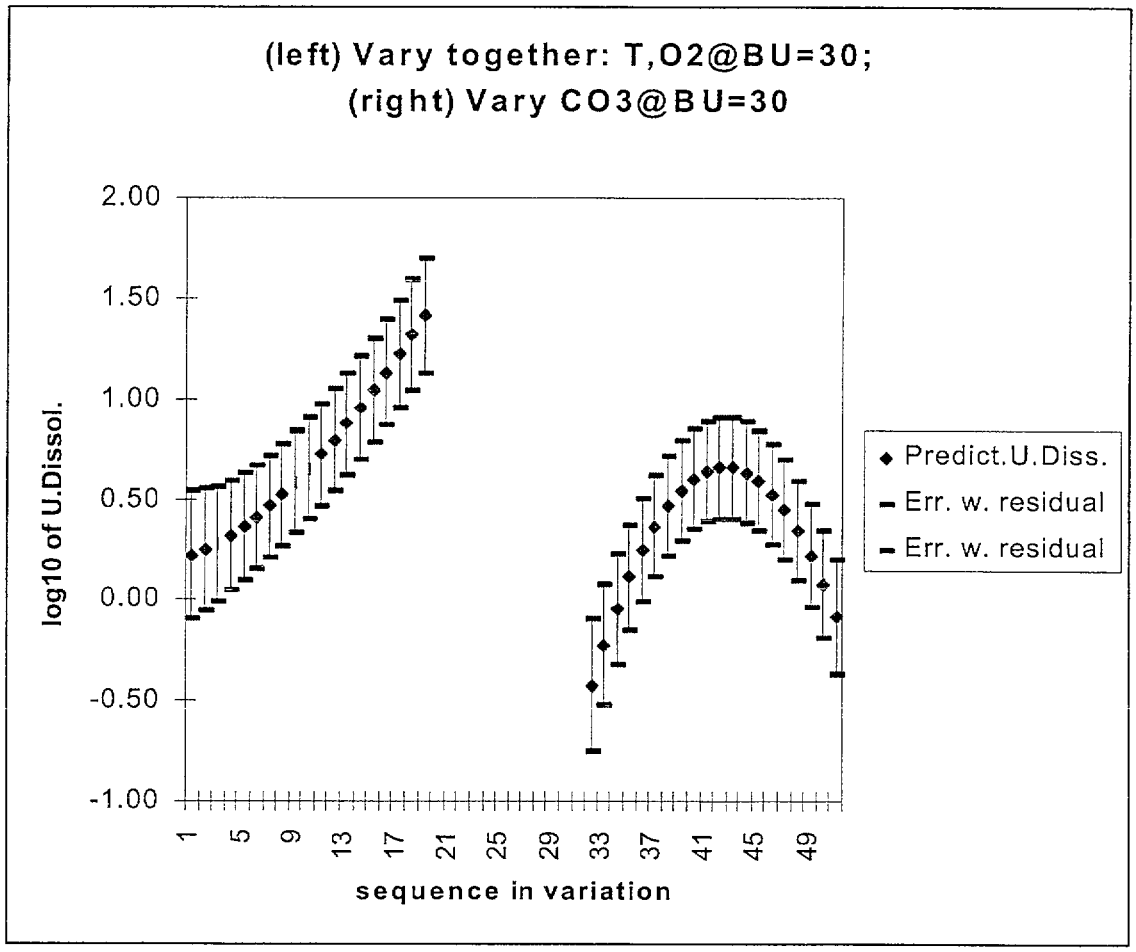

Figure 6-26. Error Bars for Two Typical Data Series Through the Span of Data Covered by the Fitting Data and Extending Beyond the Fitting Data; Same Data Series as in Fig. 6-25; Fitting Errors and Residual Error are Included

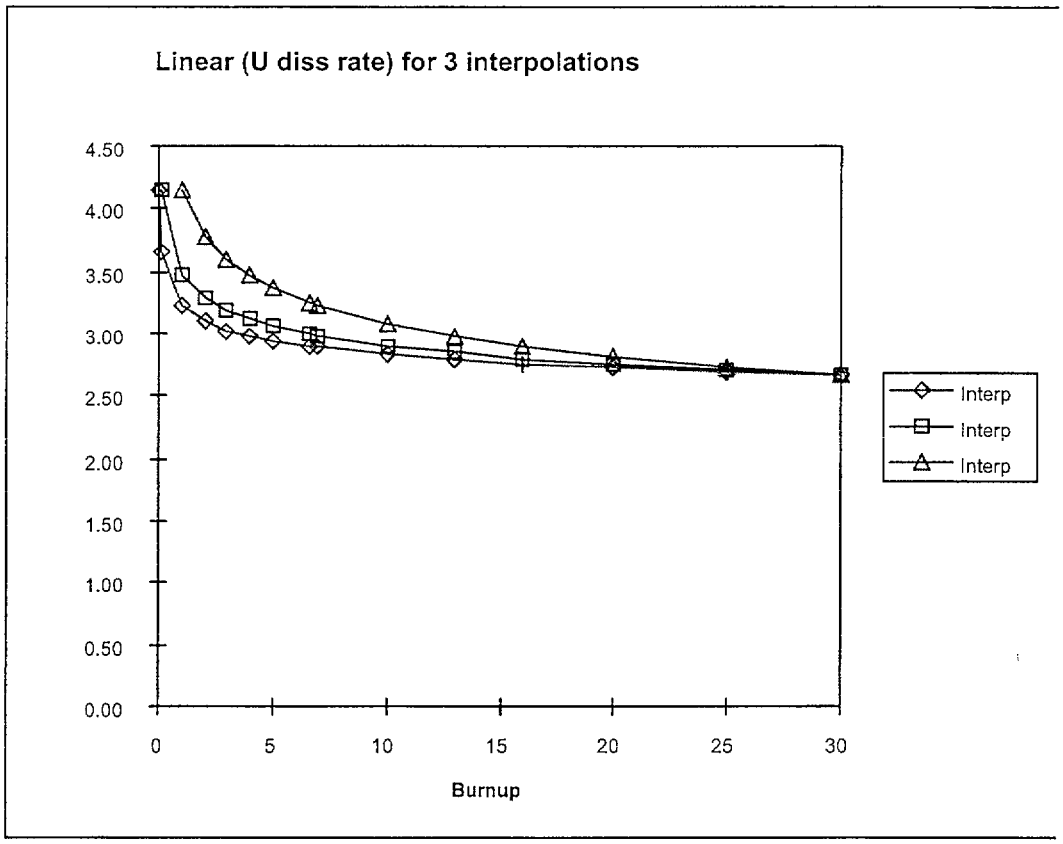

Figure 6-27. Different Logarithmic Interpolations from End Points Based on the Low-End and the 30 MW-Days/kgu Points of Equation 6-27
We vary the lower end x-value and keep the upper x-value of 30 MW-days/kgU. The difference is seen to be small for the higher burnup values within this burnup range.

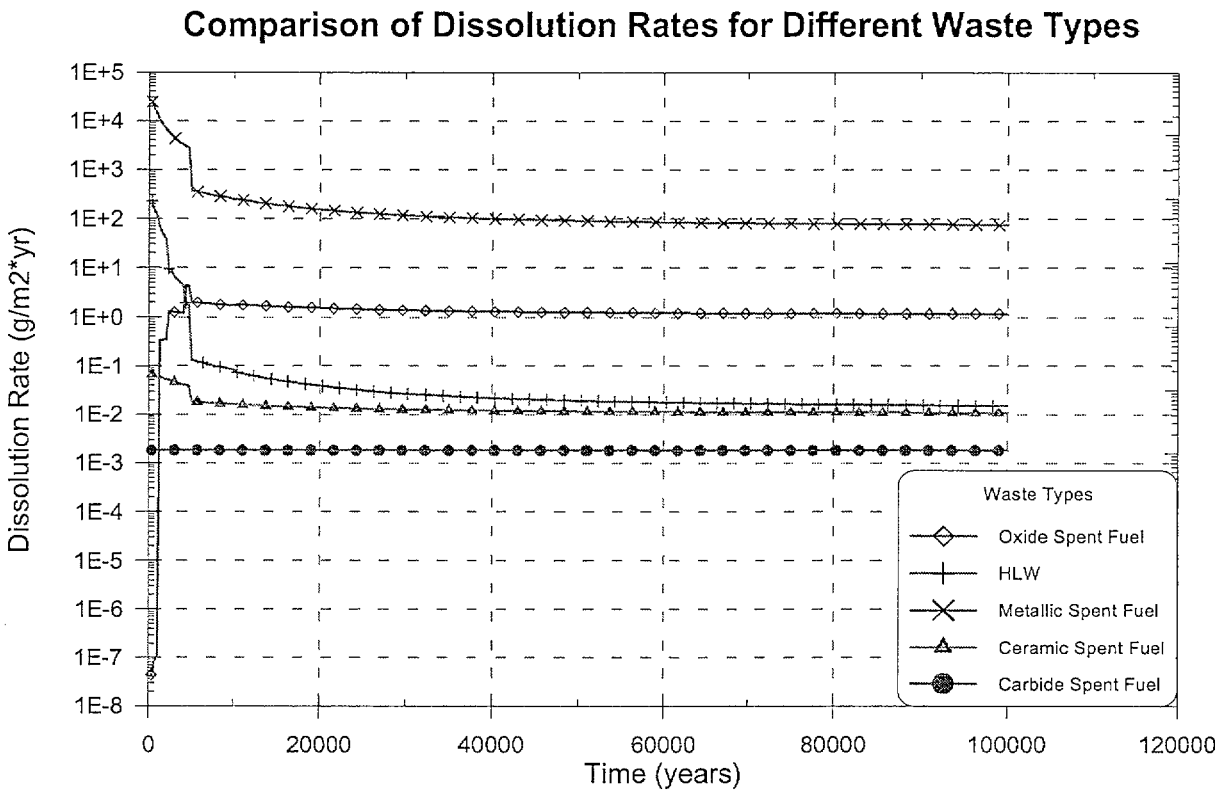

Figure 6-28. Comparison of Dissolution Rates for HLW, Metallic Spent Fuel, Oxide Spent Fuel, Carbide Spent Fuel, and Ceramic Spent Fuel

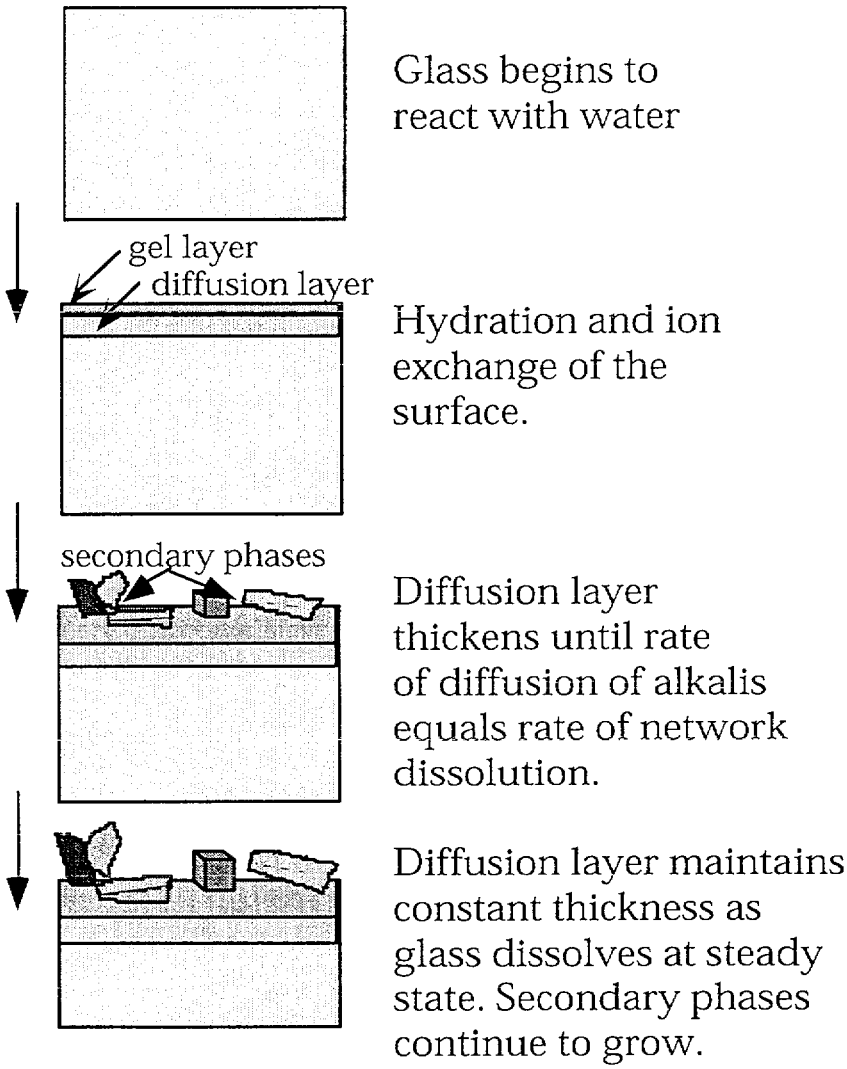

Figure 6-29. Glass Dissolution Mechanism (from Bourcier 1994).

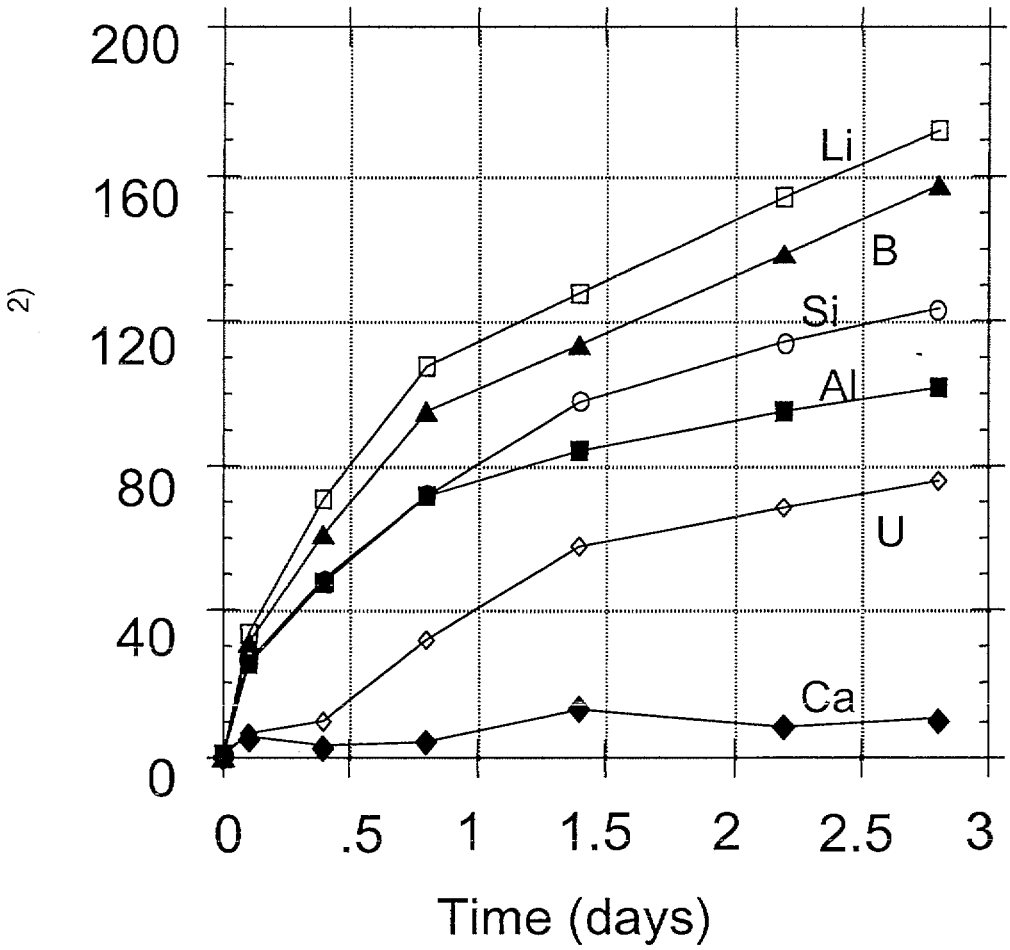

Figure 6-30. Normalized Elemental Release from SRL-165 Glass Reacted in 0.003M NaHCO3 at 150°C, SA/V 0.01cm^{-1}

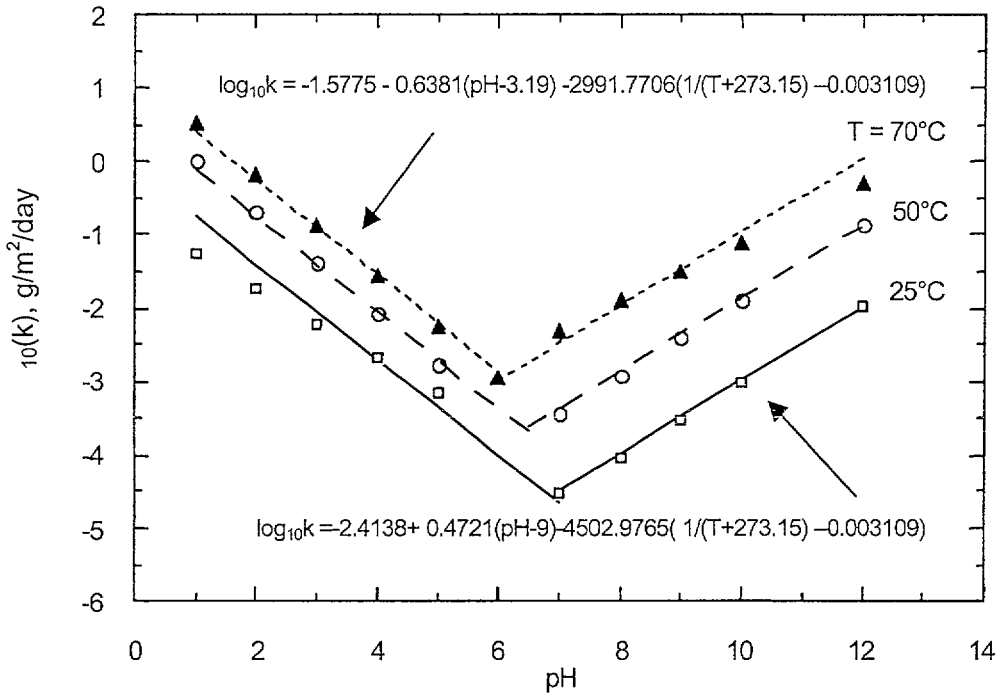

Figure 6-31. Log_{10} (Dissolution Rate, $g/m^2/day$) Versus Solution pH

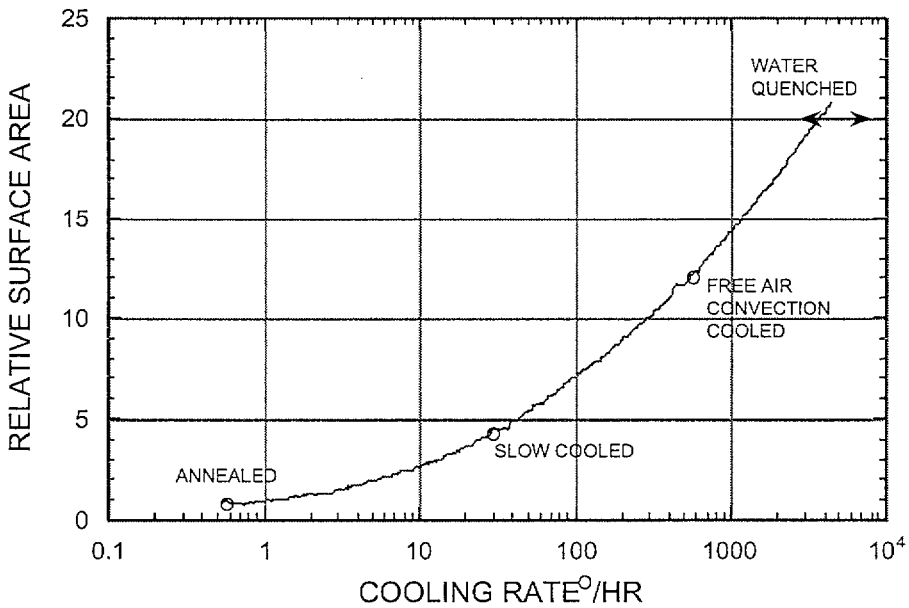

Figure 6-32. Area Increase of Thermally Shocked Simulated Nuclear Waste Glass
Values are relative to geometric area of glass cylinder with no surface roughness. Data from Ross and Mendel 1979.

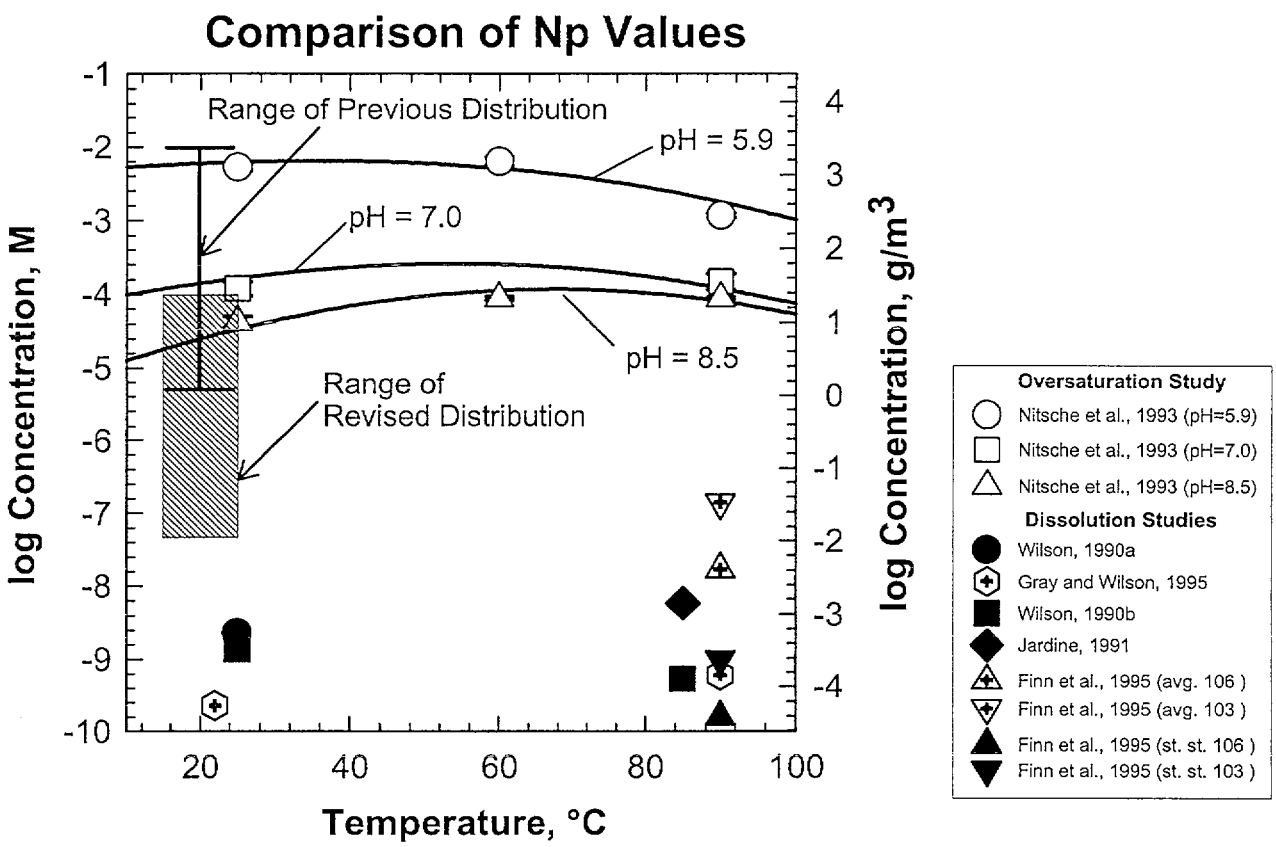

Figure 6-33. Range of Revised Solubility-Limited Np Concentration Distribution (Shading) for TSPA-VA (After Figure 3-1 CRWMS M&O 1998a)
Comparison of the previous range of project elicited values (bar) based on the oversaturation measurements of Nitsche et al. (1993) with the values derived from spent fuel dissolution studies starting from undersaturation and the range of the revised (shading) distribution (st. st. = steady state; avg. = average of whole test time for Finn et al. 1995 study).

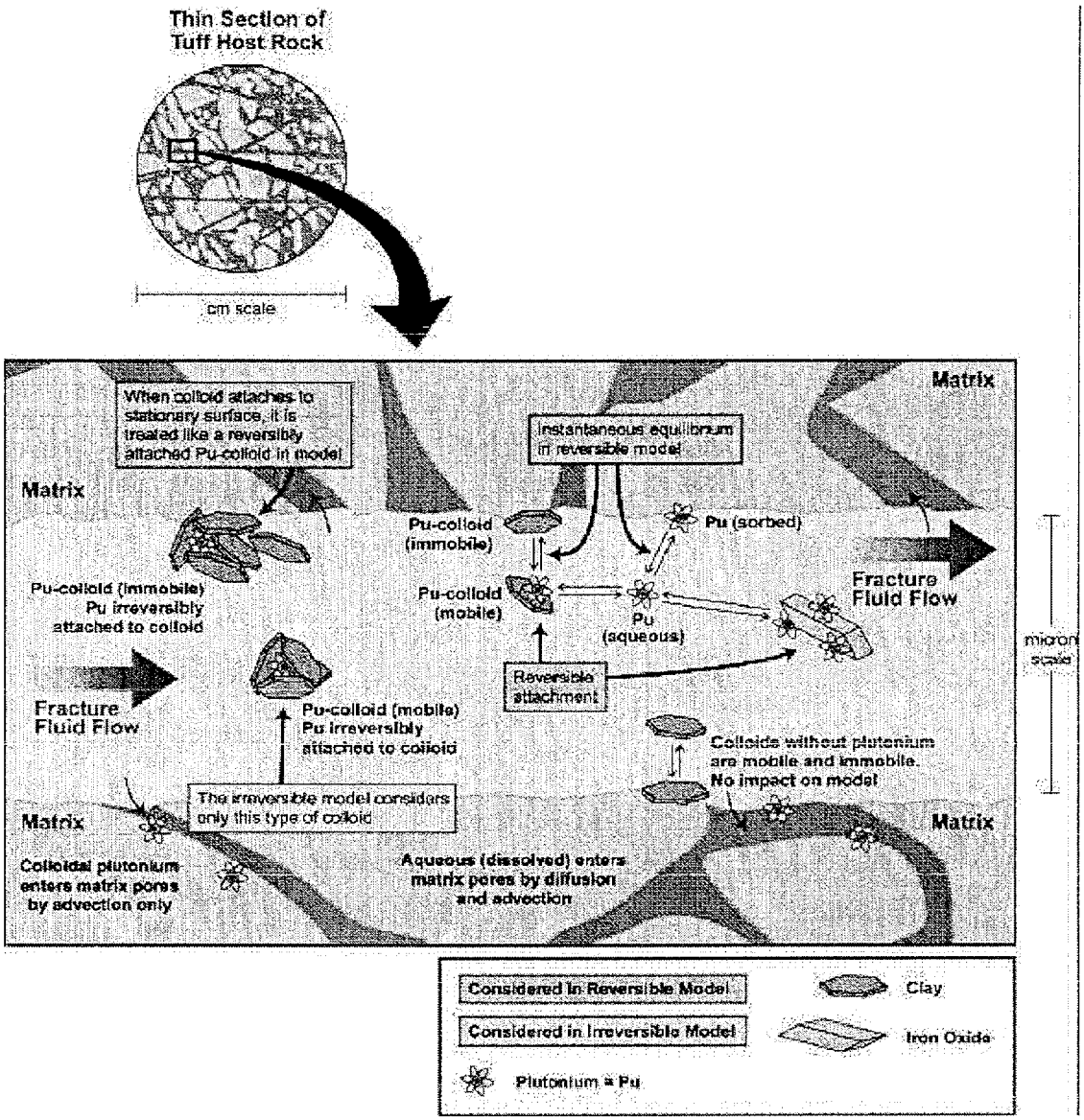

Figure 6-34. Colloidal Mobilization of Plutonium and Transport Through the EBS

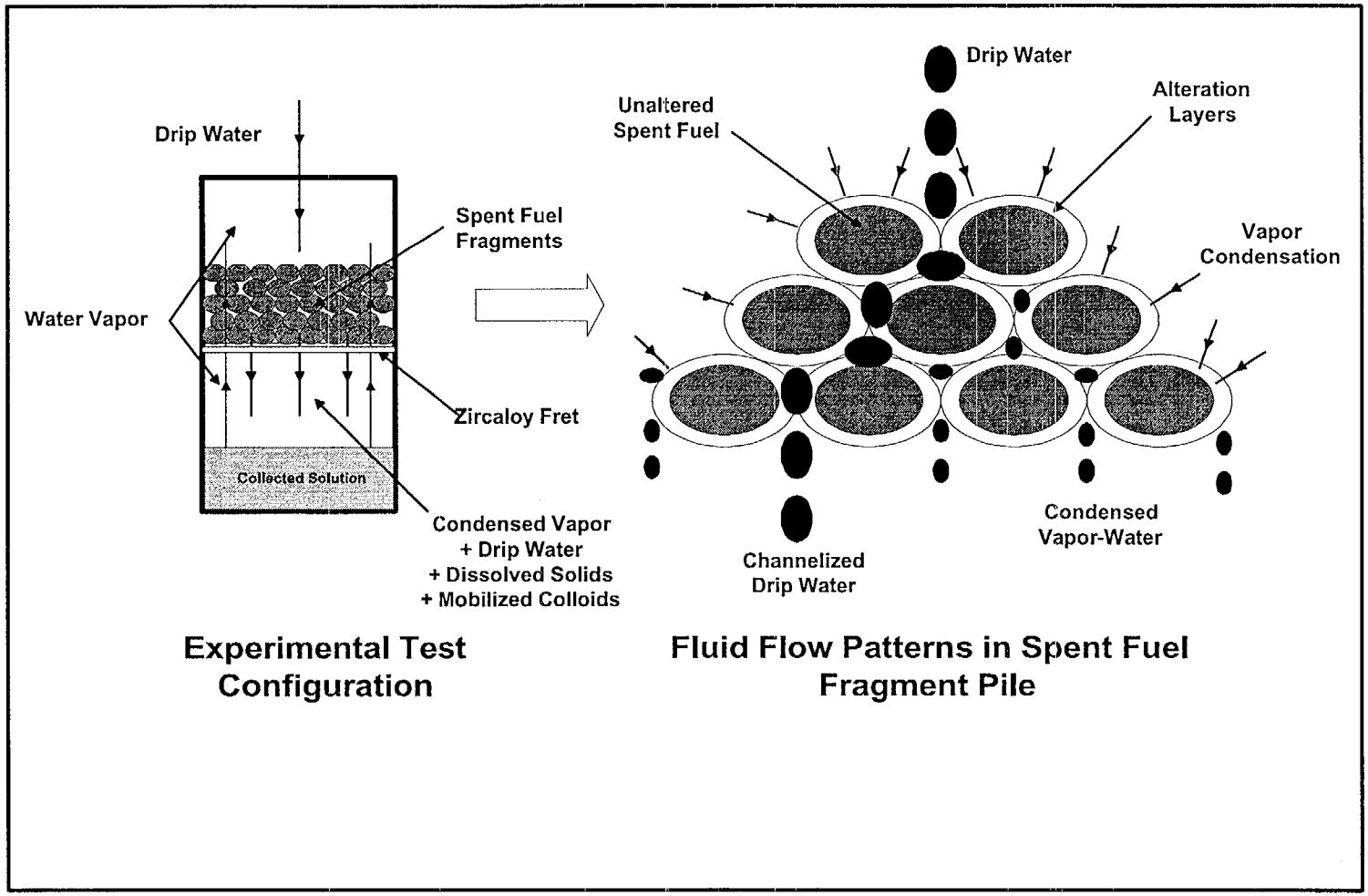

Figure 6-35. Experimental Test Configuration

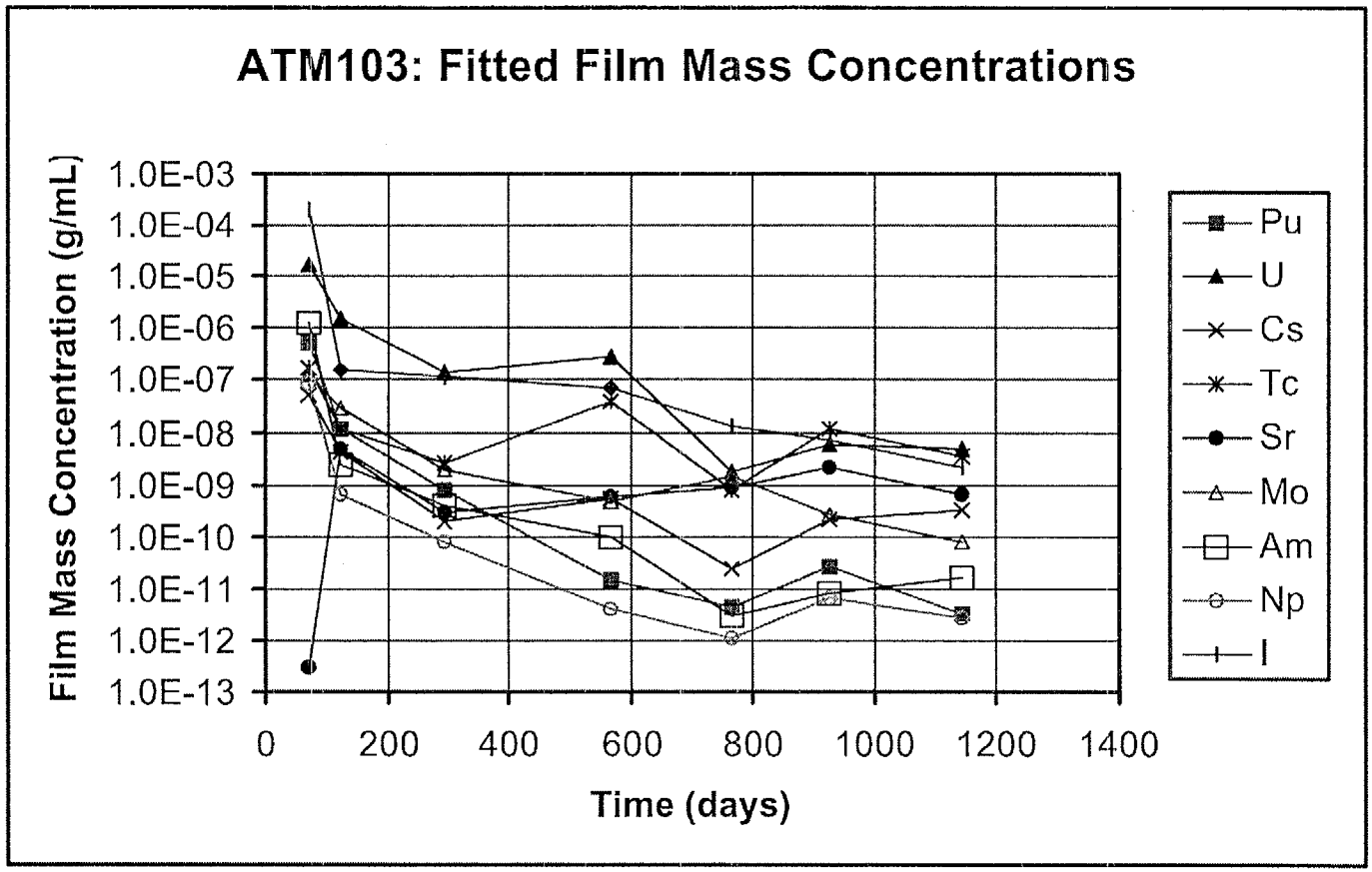

Figure 6-36. Equilibrium Film Mass Concentrations Fitted to ATM-103 Spent Fuel Vapor Test and Low-Drip Test Data Using Advective Transport Limited Approximate Model

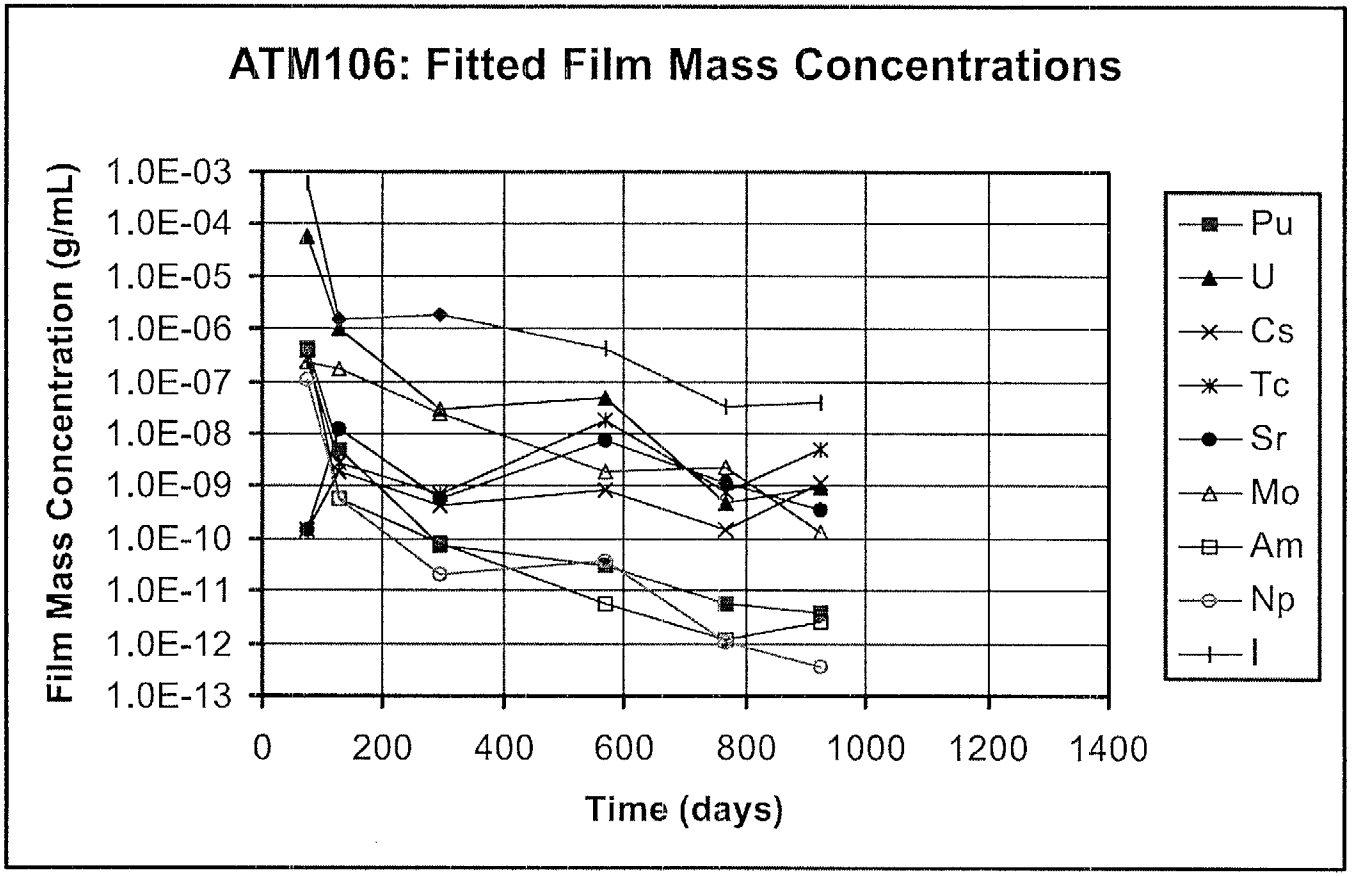

Figure 6-37. Equilibrium Film Mass Concentrations Fitted to ATM-106 Spent Fuel Vapor Test and Low-Drip Test Data Using Advective Transport Limited Approximate Model

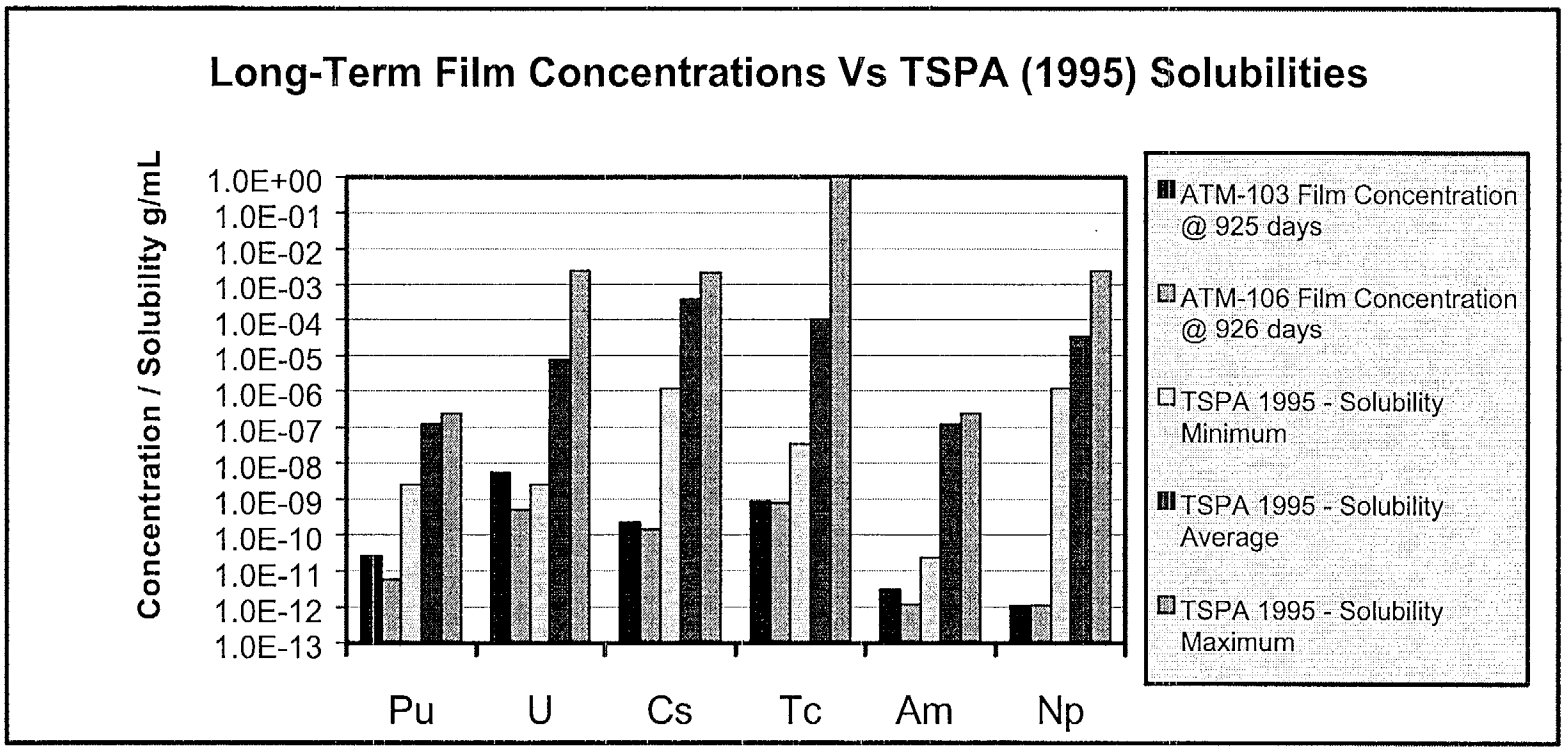

Figure 6-38. Comparison of Long-Term Equilibrium Film Mass Concentrations Fitted to Spent Fuel Vapor Test and Low-Drip Test Data Against TSPA 1995 Recommended Solubility Limits
Neptunium solubility limits have been reduced by two orders of magnitude in this analysis (TSPA-VA) from the values shown (Section 6.4.3.1.4).

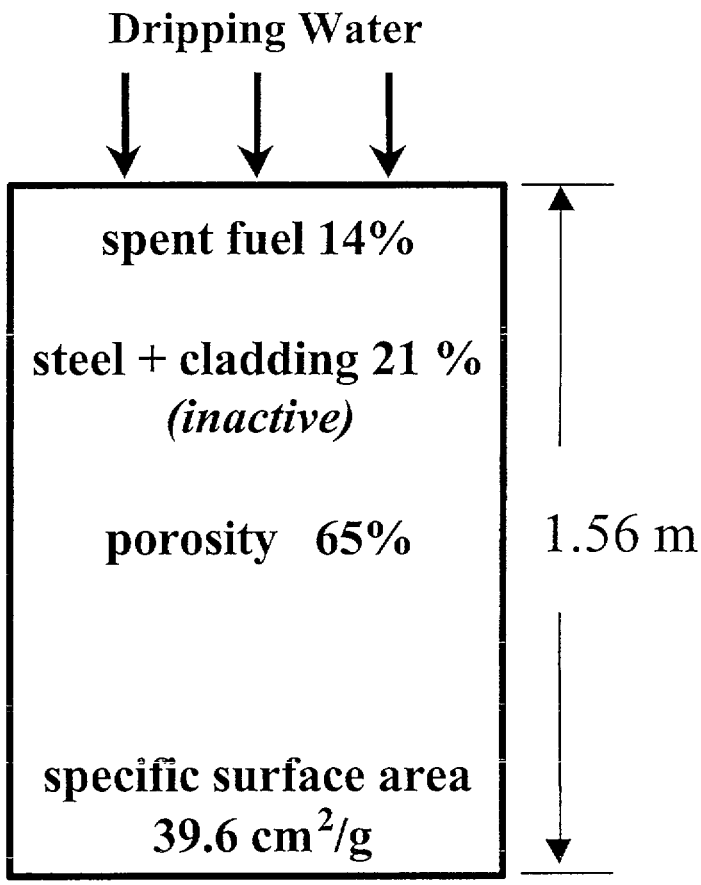

Figure 6-39. Schematic of AREST-CT Simulation Configurations for 1-D Reactive Transport Analysis of the Evolution of CSNF Under Low Water Flow Conditions

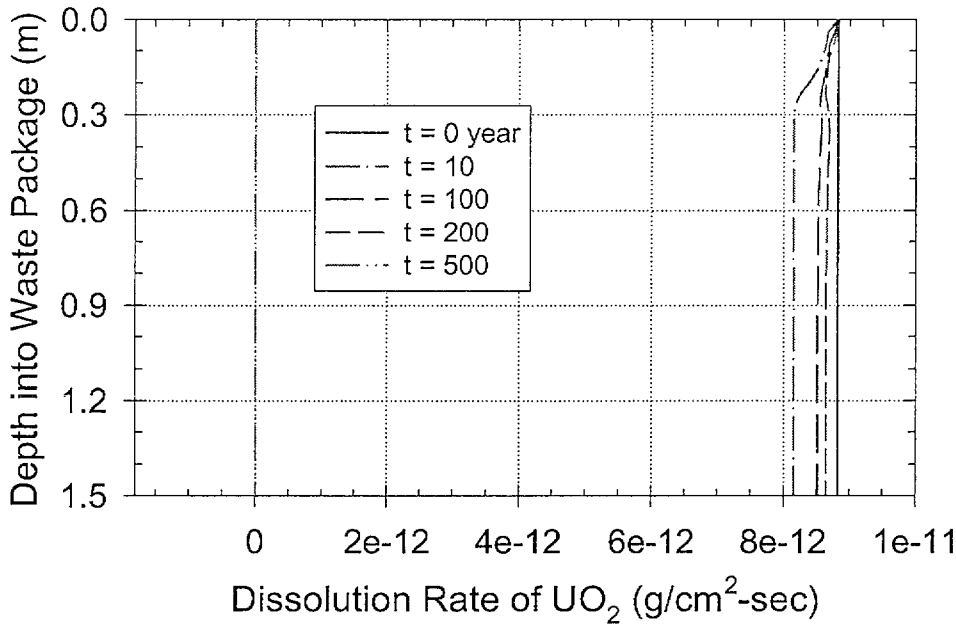

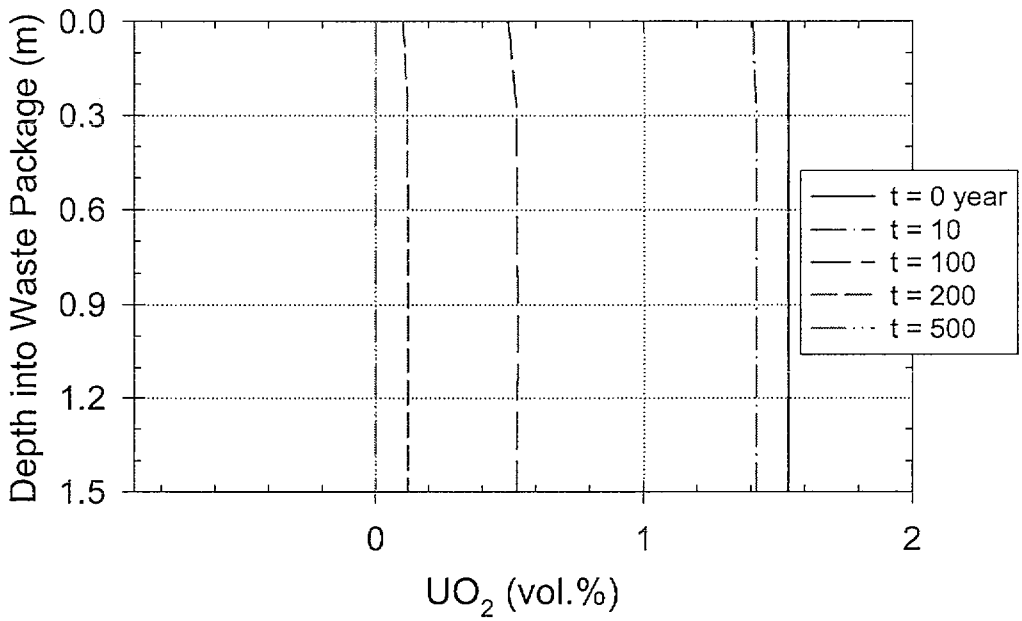

Figure 6-40. Profiles of Dissolution Rate
(a) and volume fractions (b) of spent fuel for Case A. The dissolution rate varies less than 15% with time and space. Available spent fuel is totally consumed after 500 years of dissolution.

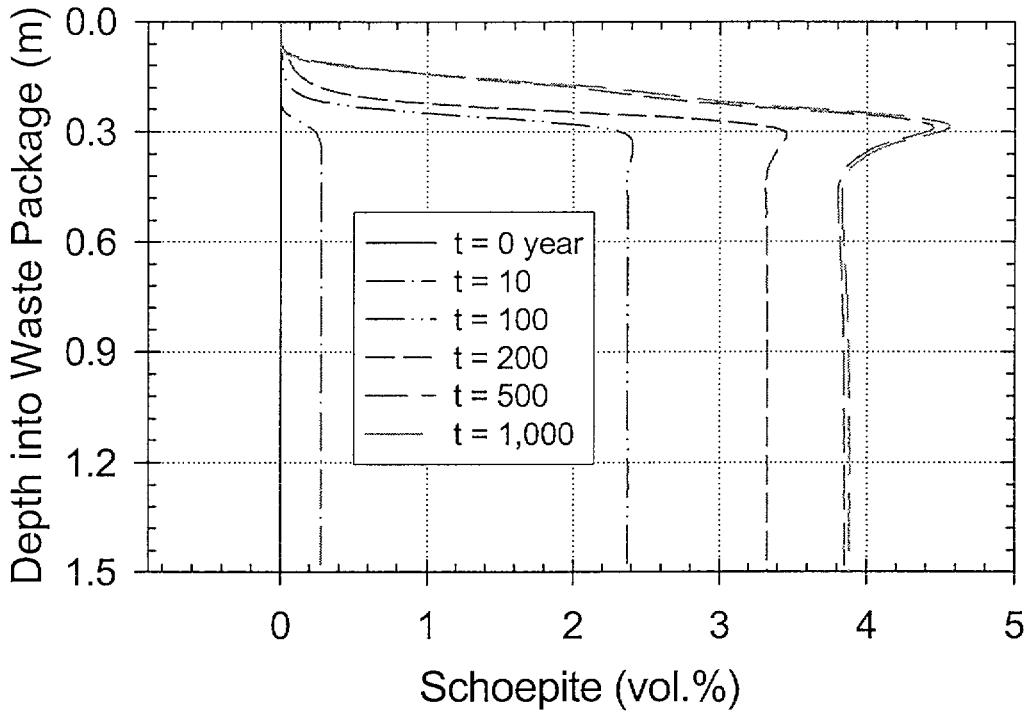

(a)

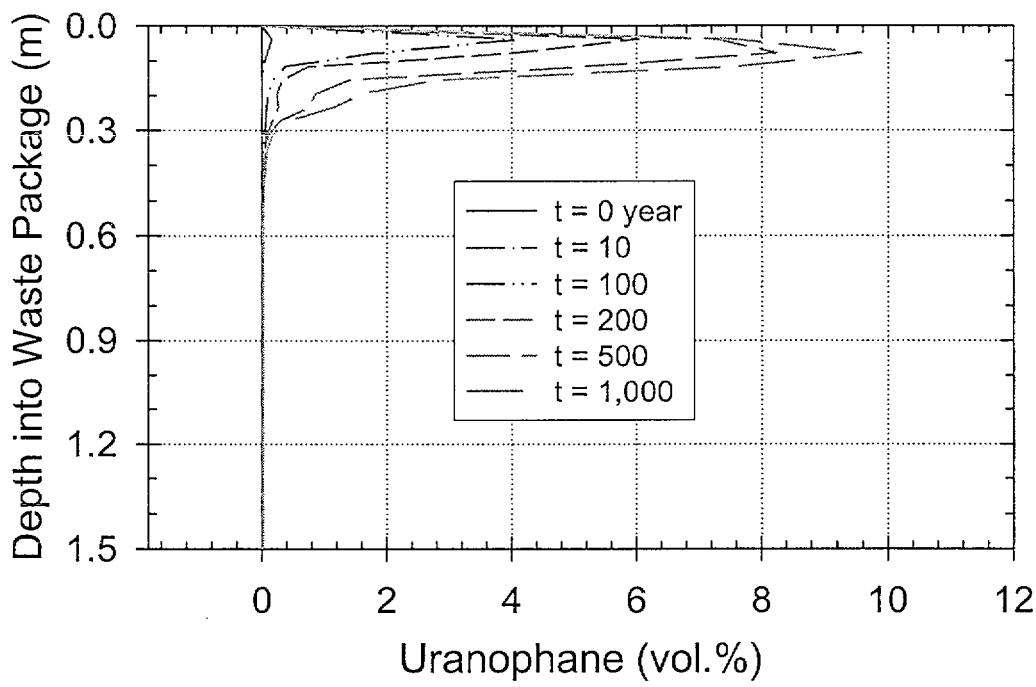

(b)

Figure 6-41. Volume Profiles of Secondary Minerals Precipitated when Spent Fuel Dissolves (a) schoepite, the major secondary minerals; (b) soddyite, precipitated at the top of WPs and re-dissolved after spent fuel is consumed; (c) uranophane, mainly precipitated at the top of WPs. Closely exam the movement of precipitation fronts reveals, though not very obvious, that the growth of uranophane is at the expense of schoepite and soddyite

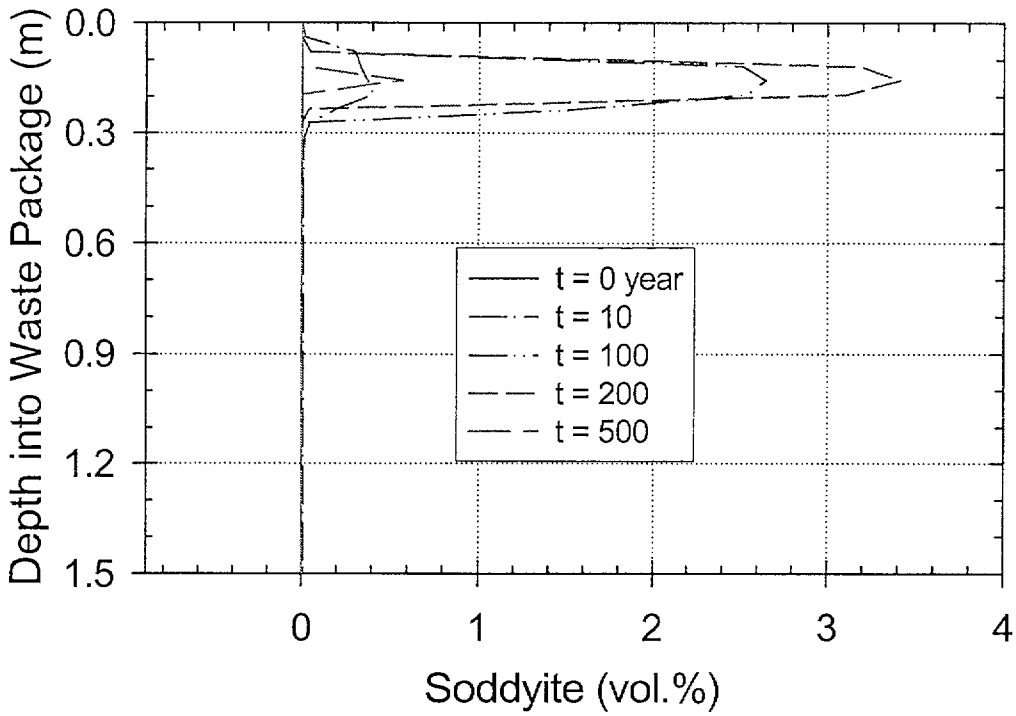

(c)

Figure 6-41. (continued)

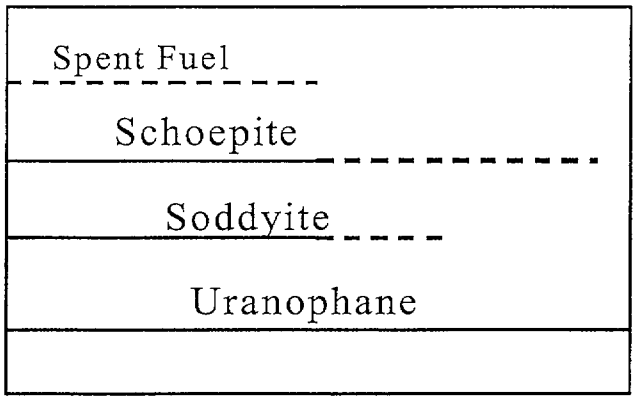

Figure 6-42. Paragenetic Sequence of Secondary Minerals Observed in the Simulation Results
Dashed line means meta-stable phases. Uranophane is the most stable uranyl mineral.

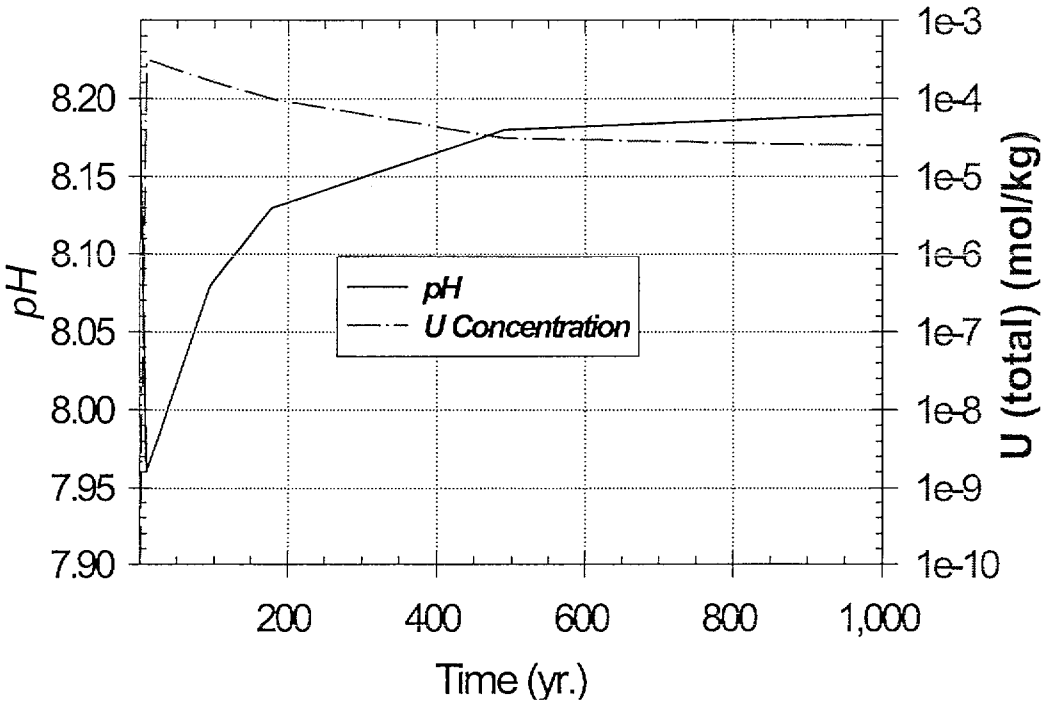

Figure 6-43. pH and U(Total) Concentration Changes for Case A
pH drops from its original value of 8.2 to 7.95 at 10 years and then reverses to its original value. U(total) increases first and then decreases.

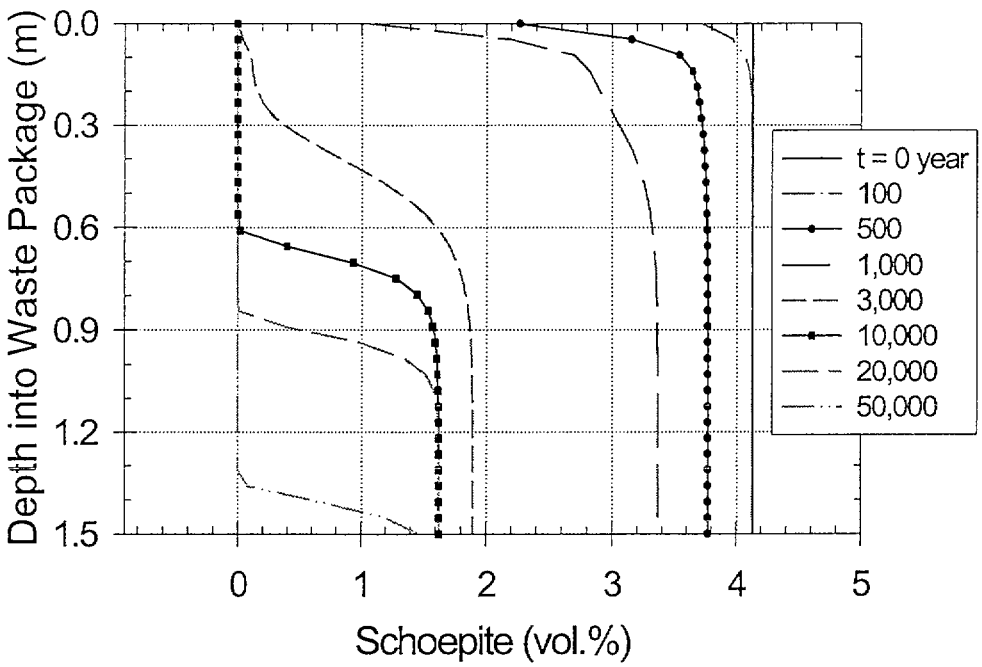

Figure 6-44. Simulated Schoepite Profiles for Case-1 at Different Time
Schoepite dissolves and disappears at 50,000 years. Before 10,000 years, the dissolution takes place across the whole WP. After that dissolution is localized to the dissolution front, which advances with time from upstream to down stream.

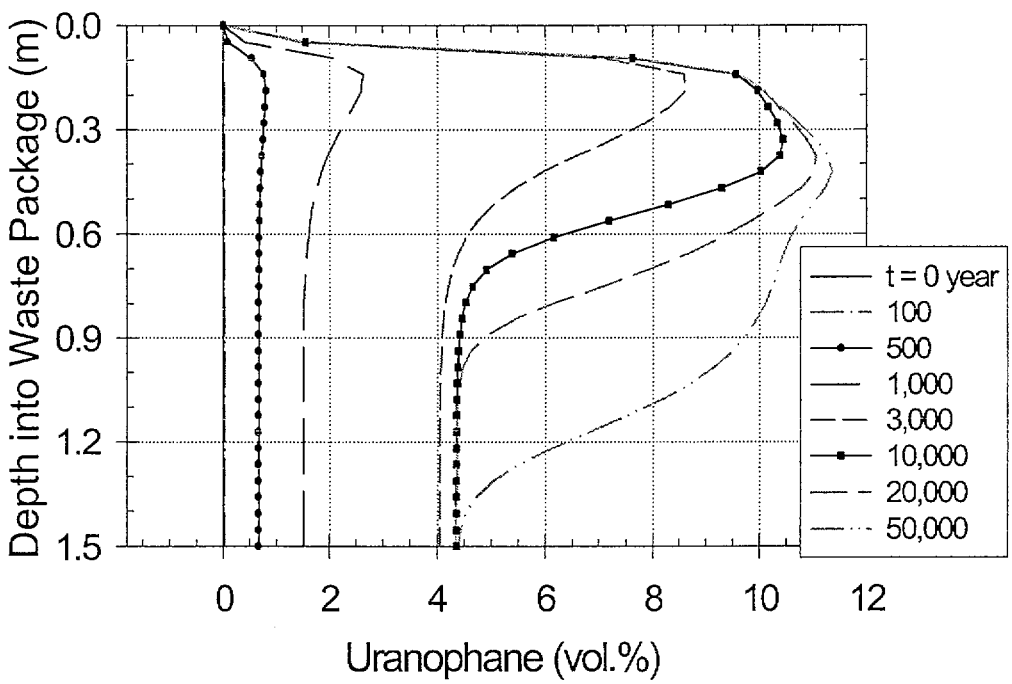

Figure 6-45. Simulated Uranophane Profiles for Case-1
Uranophane replaces schoepite. Before 10,000 years, it precipitates across the whole WP. After that time, the precipitation front advances from upstream to downstream.

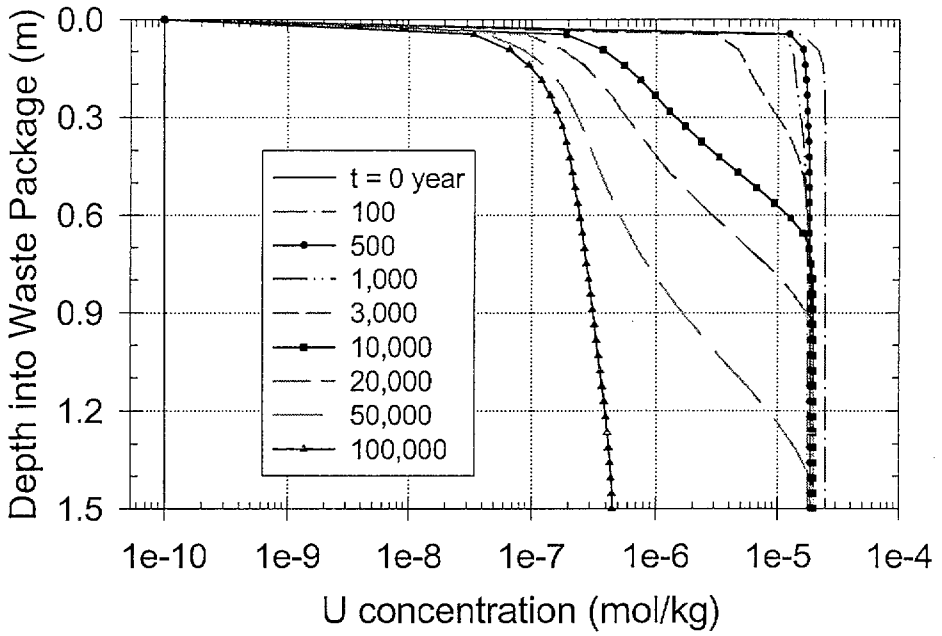

Figure 6-46. Simulated Concentrations of U
It increases with depth into WP and reaches its maximum at the bottom of WP. After 50,000 years, U concentration at the bottom decreases.

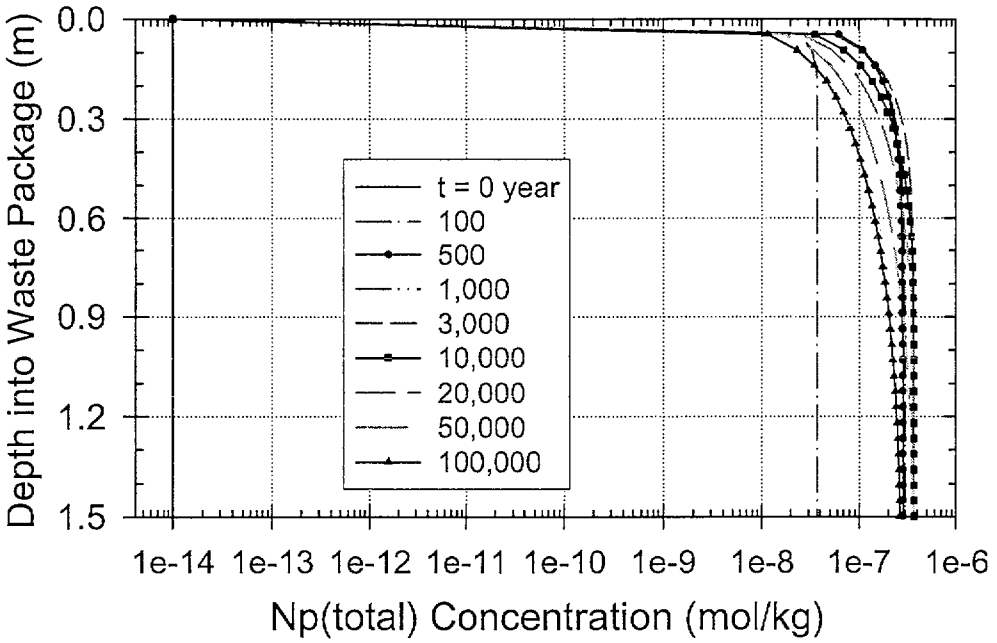

Figure 6-47. Simulated Concentrations of Np for Case-1
Similar to U, it increases with depth into WP and reaches its maximum at the bottom of WP. It starts decreasing after 50,000 years.

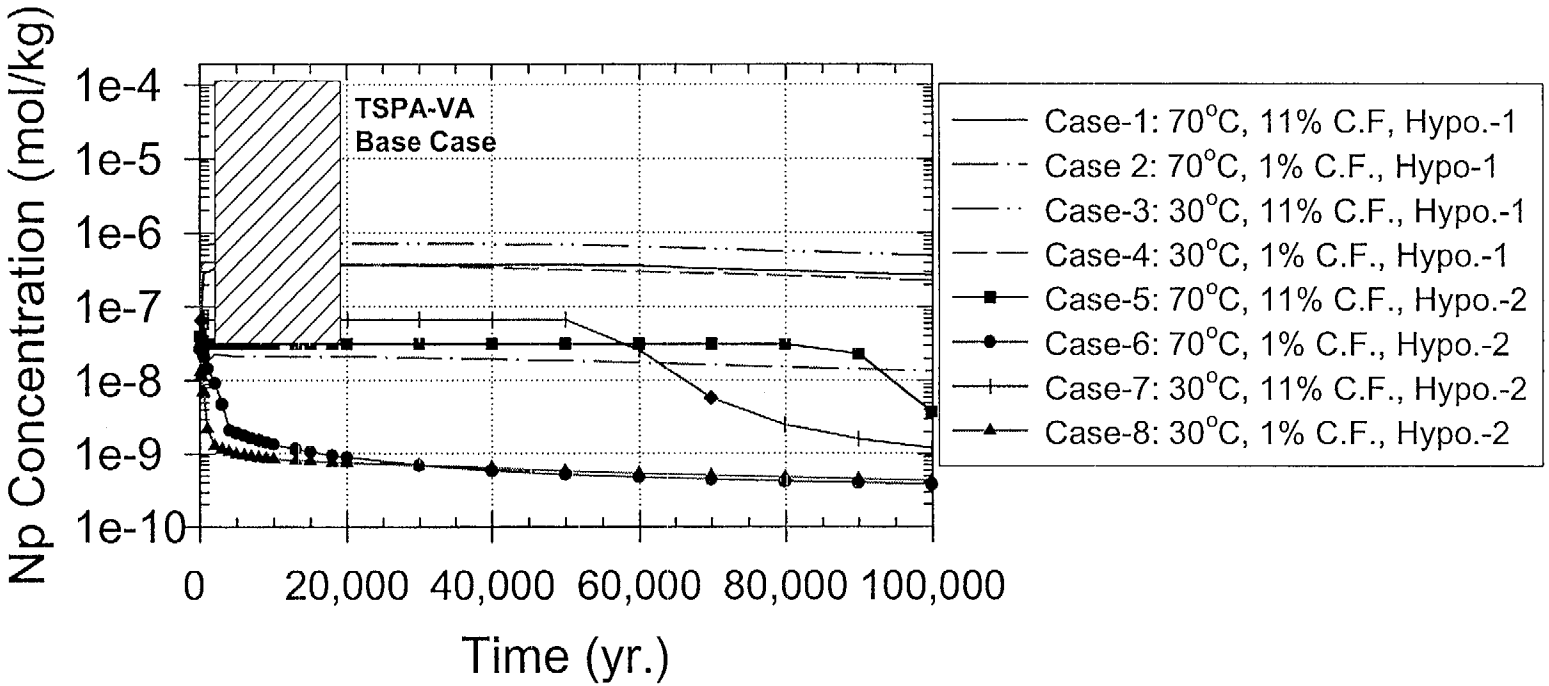

Figure 6-48. Calculated Np Concentrations at the Bottom of WP for the 8 Simulations
The cases of Hypothesis-1 (Cases 1-4) have no symbols, while the cases of Hypothesis-2 are denoted with symbols. The simulations go for 100,000 years. The shadowed rectangle is the range of Np distribution used in the TSPA-VA Base Case. The calculated Np concentrations are lower than that of the TSPA-VA Base Case value. The up-bound of Np concentration for Hypothesis-1 cases is 2 orders of magnitude lower than that of the TSPA-VA Base Case, and the lower-bound for Hypothesis-1 is about 5 time lower than that of the TSPA-VA Base Case. For the cases of Hypothesis-2, the up-bound is about 3 orders of magnitude lower, and the lower-bound is about 2 orders of magnitude lower.

Potential Water Flow in the EBS

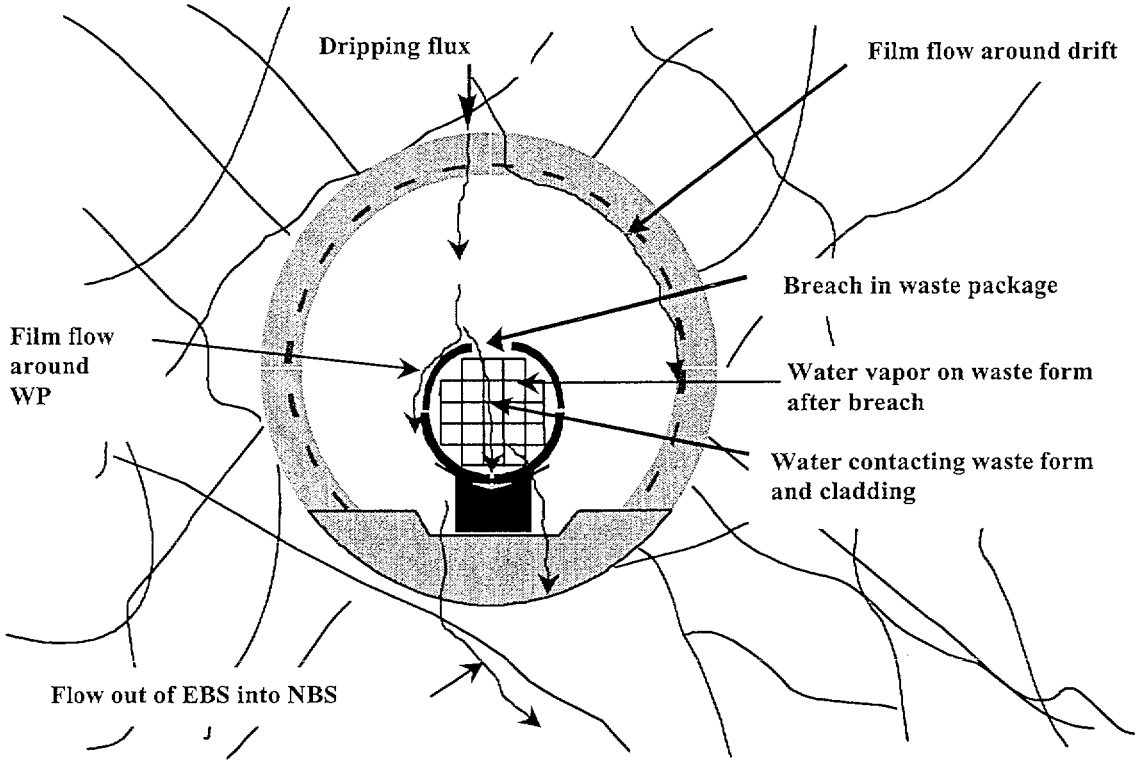

Figure 6-49. Potential Water Flow in EBS

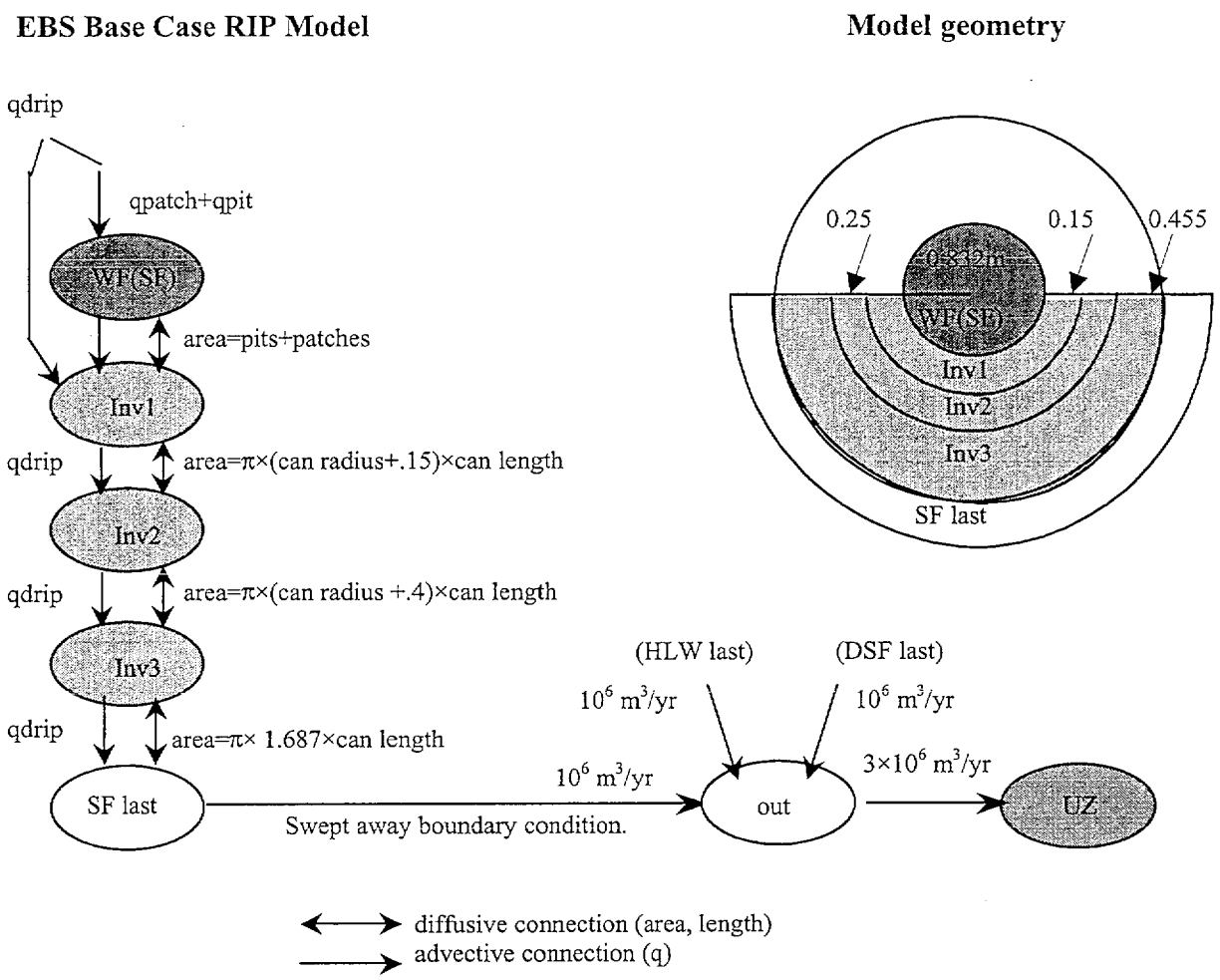

Figure 6-50. Schematic Representation of the Implementation of the EBS Model Showing the Reaction Cells used in RIP

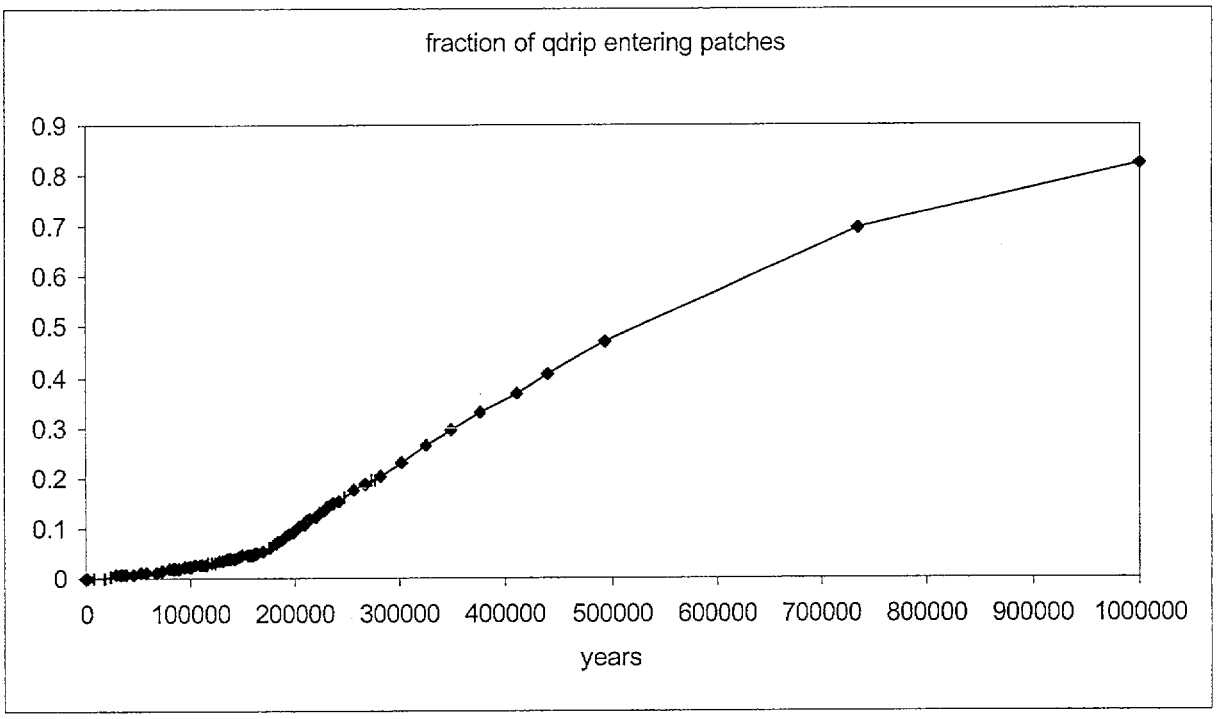

(a)

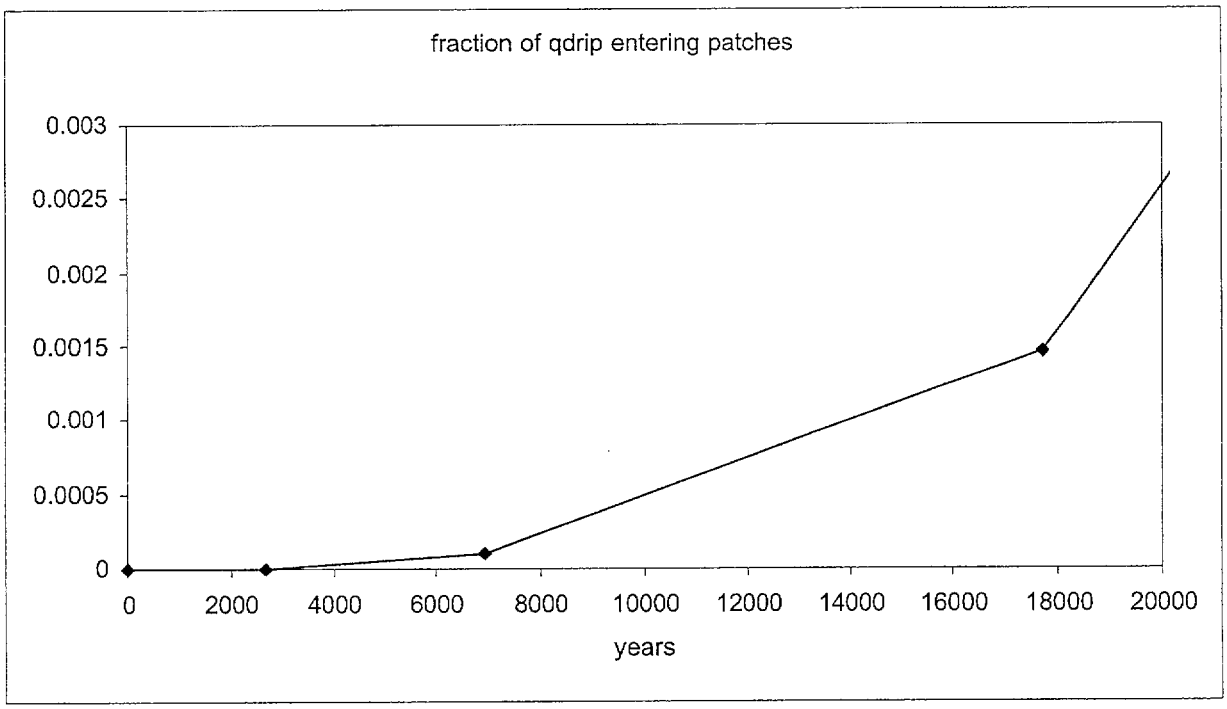

(b)

Figure 6-51. Fraction of Seep Entering Package Through Patches, Expected Value Case

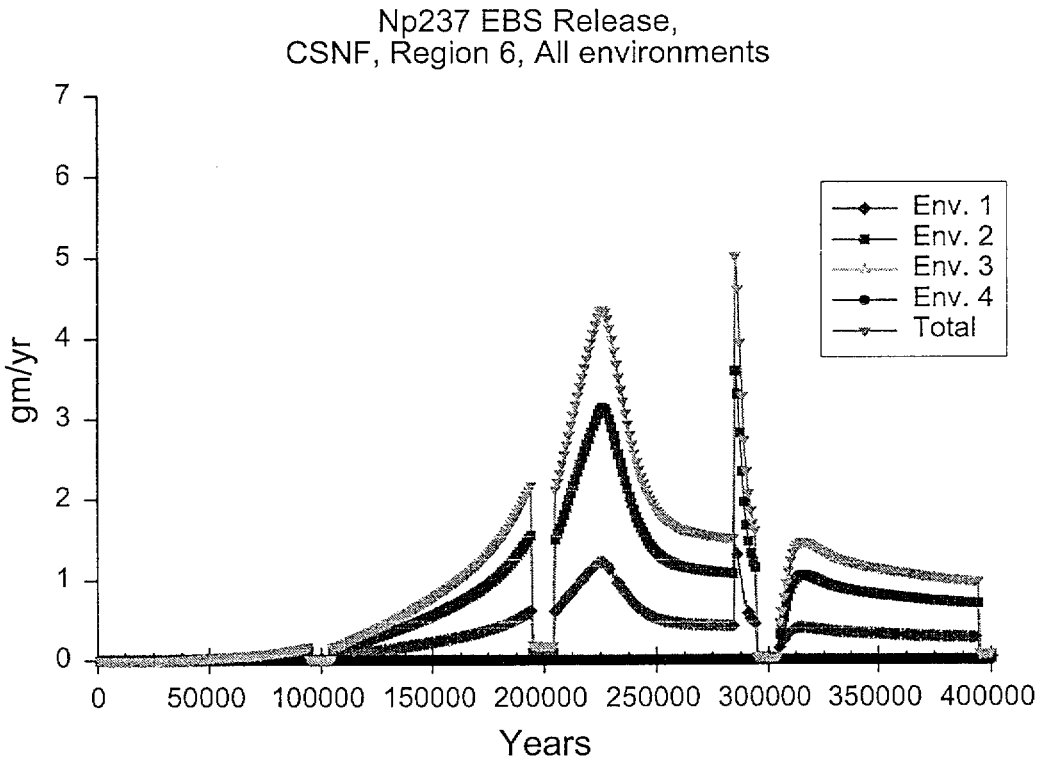

Figure 6-52. EBS Release of ^{237}Np from four Four Environments

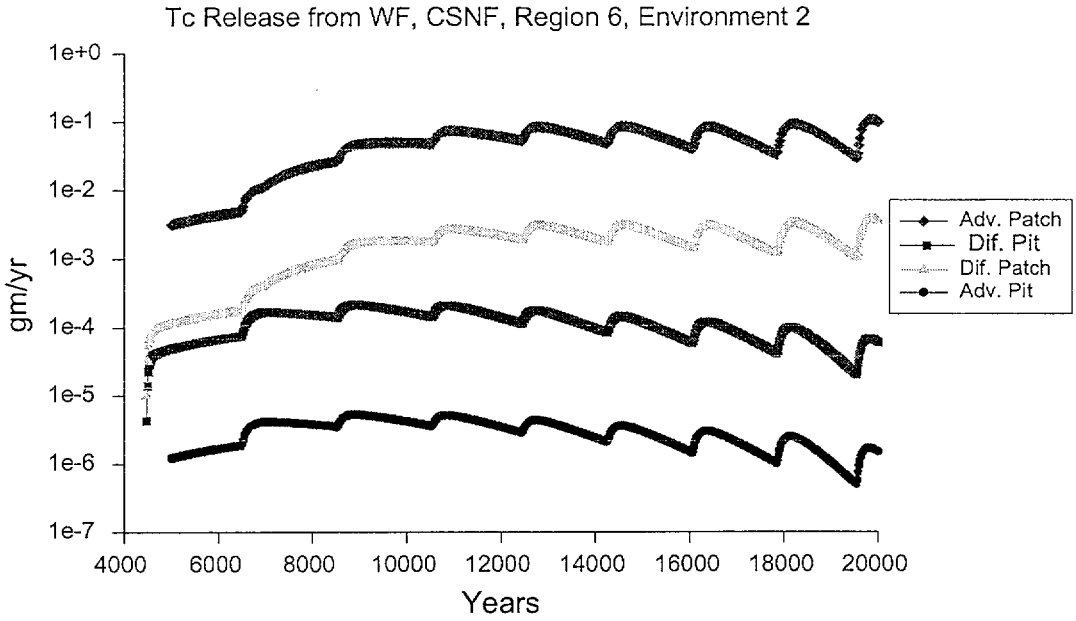

(a)

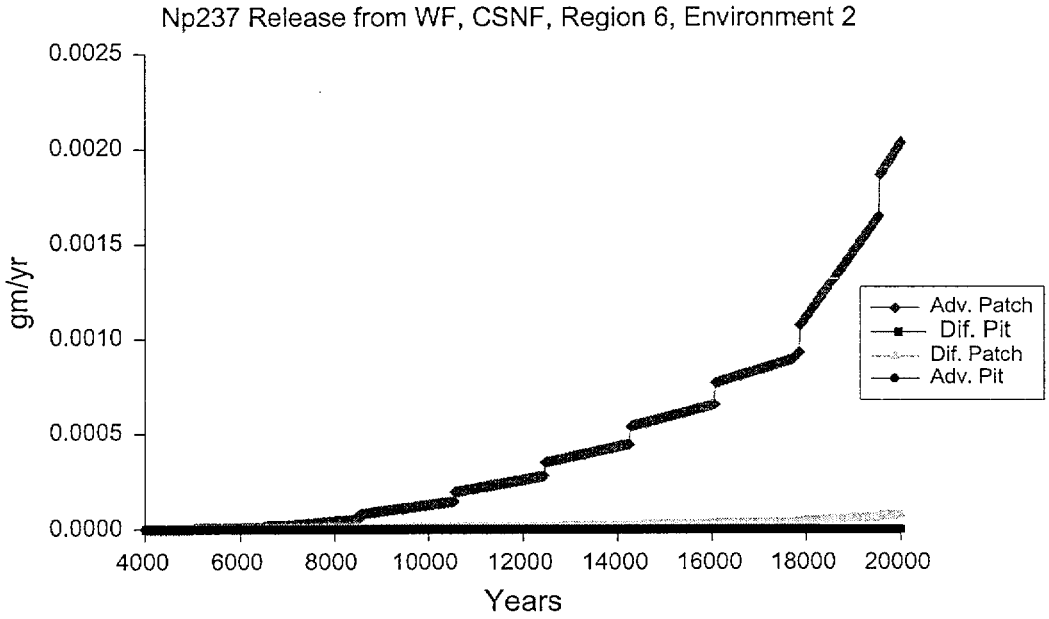

(b)

Figure 6-53. Release from Waste Form, Expected Value Case, Commercial Spent Fuel, Region 6, Environment 2, 20,000 Years

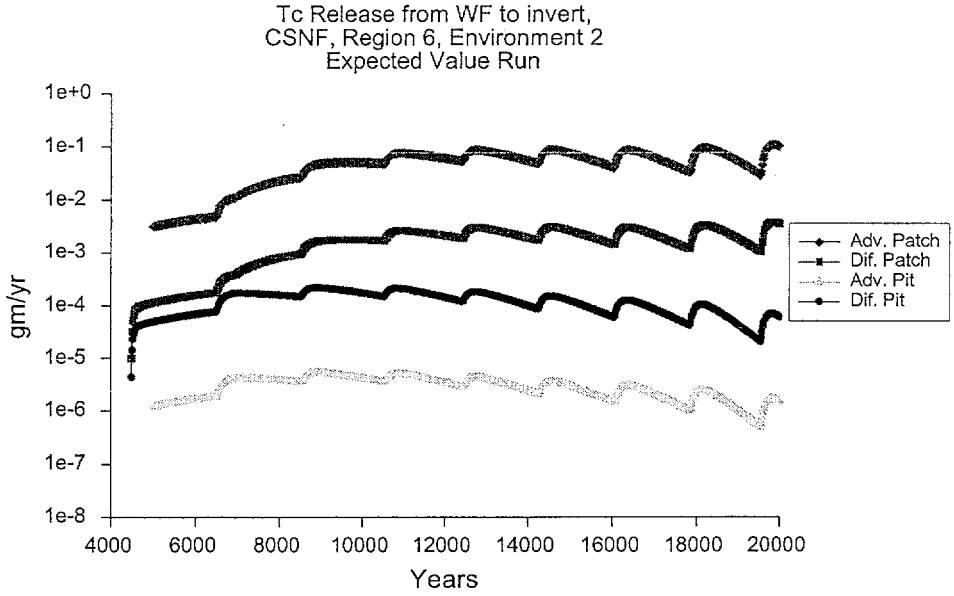

(a)

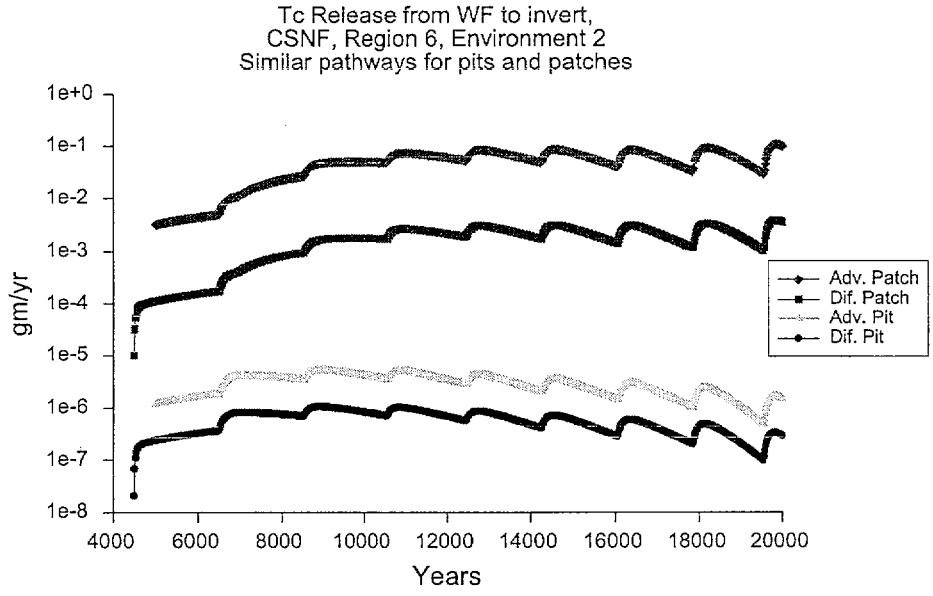

(b)

Figure 6-54. Comparison of Tc Releases from the WF Using Different Diffusive Pathway Definitions

BEHAVIOR OF ZIRCALOY-4 AND ZIRCONIUM LINER ZIRCALOY-4 CLADDING AT HIGH BURNUP

L. F. Van Swam
Siemens Power Corporation
P. O. Box 130
Richland, Washington 99352-0130
(509) 375-8100

A. A. Strasser
Aquarius Services Corporation
17 Pokahoe Drive
North Tarrytown, NY 10591
(914) 366-8875

J. D. Cook
Rochester Gas and Electric Corporation
49 East Avenue
Rochester, NY 14609
(315) 524-4446

J. M. Burger
Empire State Electric Energy Research Corporation
1515 Broadway
New York, NY 10036-5701
(212) 302-1212

ABSTRACT

Fuel rods with different combinations of solid and annular pellets and through-wall and zirconium liner Zircaloy-4 cladding have been irradiated in the R. E. Ginna pressurized water reactor for four and five cycles, reaching burnups of approximately 57 MWd/kgU. Extensive poolside and hot cell examinations were performed to determine cladding oxidation, fuel rod diameter changes, cladding hydrogen pick-up and hydride distribution, and cladding strength and ductility at fast fluences (E > 1 MeV) of 7 x 10^{25} and 8.9 x 10^{25} n/m^2. Different behavior of the through-wall cladding compared to the liner cladding was observed and is discussed in the paper.

I. INTRODUCTION

The Empire State Electric Energy Research Corporation (ESEERCo), Rochester Gas and Electric Corporation (RG&E), and Siemens have carried out a program to fabricate, irradiate, and examine advanced PWR fuel rod designs containing annular fuel pellets, through-wall Zircaloy-4 cladding, and Zircaloy-4-zirconium liner cladding. Included for comparison were fuel rods with solid pellets and through-wall Zircaloy-4 cladding. The objectives of the program were to develop a fuel design with increased margin to failure and increased high burnup potential and to obtain performance data up to high burnup for use in fuel modeling.

Four demonstration test assemblies (DTAs) were designed and fabricated by Siemens. Irradiation and poolside examinations at RG&E's R.E. Ginna plant in New York State were completed after exposure of segmented fuel rods to 47 MWd/kgU after four cycles and to 57 MWd/kgU after five cycles. Hot cell examinations of four-cycle and five-cycle segmented fuel rods were carried out at the laboratories of Commissariat à l'Energie Atomique (CEA) in Grenoble, France.

This paper discusses the high-burnup behavior of standard through-wall Zircaloy-4 cladding and Zircaloy-4-zirconium liner cladding.

II. PROGRAM DESCRIPTION

A. Assembly and Fuel Rod Design

Each of the four 14x14 rod array assemblies fabricated for the program contained 179 fuel rods, 16 Zircaloy-4 guide tubes, and one instrument tube. The egg crate type spacers were of Zircaloy-4 with Inconel spacer springs. The assemblies had removable upper tie plates with Inconel leaf springs of standard design. The assemblies contained fuel rods 0.417 inch (10.59 mm) in diameter and 149 inches (3785 mm) long, with annular pellets and sponge zirconium liner-Zircaloy-4 cladding. Two of the DTAs contained 11 segmented rods each. The segmented rod consisted of four segments, the center two of which were characterized and examined in detail after irradiation. Figure 1 shows the axial locations of the characterized center two segments within the assembly. These segments are referred to in this paper as upper and lower segments, respectively. The characterized segments are approximately 25 inches (650 mm) long, with a 21.3 inch (540 mm) long fuel column and a 2.8 inch (71 mm) long plenum. Three combinations of pellet design (annular and solid) and cladding type (Zircaloy-4 with sponge zirconium liner and through-wall Zircaloy-4) were used in the fabrication of the segmented rodlets. The size of the diametral pellet-to-cladding gap, varying from 160

to 220 microns, was another test variable. Other dimensional data of the segmented rods are provided in Table 1. The chemical composition of the cladding is given in Table 2.

Table 1 Description of Segmented Fuel Rods

Feature	Dimension inches	mm
Segment Length	25.71	653.0
Cladding OD	0.417	10.59
Cladding Wall Thickness	0.0295	0.75
Active Fuel Length	21.33	541.8
Fuel Pellet Height	0.419	10.64
Nominal Fuel Pellet OD	0.3505	8.90
Fuel Pellet ID (Annular Pellet)	0.1108	2.81

Table 2 Fuel Cladding Chemical Analysis (Percent and ppm)

	Composition							
	Percent				ppm			
	Zr	Sn	Fe	Cr	O	Si	C	N
Through-wall Cladding, Zry-4	bal	1.50	0.21	0.11	1210	37	142	24
Liner Cladding, Zircaloy-4	bal	1.49	0.21	0.11	1265	82	130	41
Liner Cladding, Zr Liner*	bal	<10	440	<50	515	<25	40	14

* Sn, Fe, and Cr values are in ppm

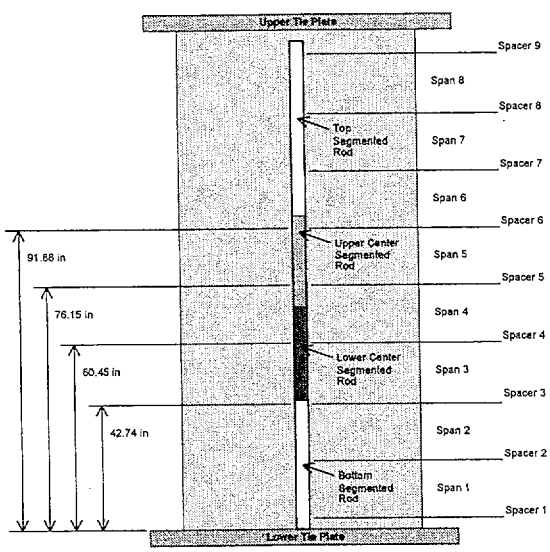

Figure 1 Axial Locations of Upper and Lower Segmented Rods within an Assembly

B. Irradiation and Power Histories

The demonstration test assemblies were irradiated for four yearly cycles to an assembly average burnup of 42.7 MWd/kgU. One of the DTAs containing segmented rods was irradiated for a fifth cycle to an average burnup of 52.1 MWd/kgU. The segmented rodlets with annular pellets reached average burnups of 47 and 57 MWd/kgU after four and five cycles of irradiation, respectively. The burnup of the solid pellet rodlets was somewhat lower due to their lower initial enrichment. The average linear heat generation rates (LHGRs) of the rodlets during the five consecutive cycles are provided in Table 3. There were no failures in any of the rods throughout the irradiation program. After five consecutive cycles of irradiation, the high-burnup assembly was still in excellent condition with no signs of bow, unusual rod-to-rod gap closure, or fuel rod fretting wear.

Table 3 Fuel Rodlet Power History, Cycle Length, and Burnup

Cycle	LHGR kW/ft (W/cm) BOC	EOC	Cycle Length, Days	Effective Full-Power Days	Assembly Burnup, MWd/kgU
1	6.4 (210)	5.7 (185)	307	285	8.9
2	9.9 (325)	8.5 (280)	322	311	23.9
3	7.9 (255)	7.4 (240)	331	319	37.0
4	3.1 (100)	3.3 (105)	355	343	42.5
5	6.5 (210)	6.8 (225)	309	271	52.1

III. PROGRAM SCOPE OF WORK

A. Poolside Examinations

The fuel assemblies were inspected after each of the first three irradiation cycles. Comprehensive poolside examinations were carried out after the fourth and fifth irradiation cycles. Fuel rods were withdrawn from the assemblies in order to determine the fuel rod length, plenum length, diameter profile, and oxide thickness along the length of the rod. Fission gas release was measured nondestructively in full-length rods and in segmented rods during the final poolside examination. Segmented rods were separated at poolside for shipment to the hot cell laboratory.

B. Hot Cell Examinations

Seventeen segmented rodlets were shipped to the CEA hot cells in Grenoble, France. Three pairs of rods with four and five cycles of irradiation were examined in detail. Less extensive examinations were performed on some of the other rods. The rods that underwent detailed examinations were numbered 1 through 6. Table 4 lists the main characteristics of these rods.

Table 4 Main Characteristics of Segmented Rods Examined at Hot Cells

Rod	Pellet Design	Cladding Type	Number of Cycles Irradiated	Rod Burnup, MWd/kgU	Axial Location*
1	Solid	Zry-4	4	43	Lower
2	Solid	Zry-4	5	52	Lower
3	Annular	Zry-4	4	47	Upper
4	Annular	Zry-4	5	57	Upper
5	Annular	Liner	4	47	Upper
6	Annular	Liner	5	57	Upper

* See Figure 1 for axial locations of upper and lower segments.

IV. RESULTS AND DISCUSSION

The results of poolside and hot cell oxide thickness and profilometry measurements are presented and discussed. Hydrogen pick-up was measured at the hot cells; hydride distribution was determined by metallographic examination. Cladding tensile tests were performed at room temperature and at 350°C.

A. Oxide Thickness

Fuel cladding oxide thickness was measured at poolside with an eddy current probe by performing a single linear scan along the length of a rod after the rod had been withdrawn from the assembly. At end-of-life, at an assembly average burnup of 52 MWd/kgU, the maximum oxide thickness of full-length rods (all with liner cladding) averaged approximately 40 microns. The maximum oxide thickness always occurred in Span 7 of the assembly. A comparison of the oxide thickness of segmented rods with through-wall Zircaloy-4 cladding and liner Zircaloy-4 cladding indicated that the liner cladding had a lower corrosion rate than the through-wall cladding. This was confirmed by hot cell measurements.

In the hot cells, four linear scans 90 degrees apart were made along each of the six rods listed in Table 4. The circumferential average oxide thickness, determined from the four linear traces, is shown in Figure 2. Indicated on the plots are the positions of spacers, the location of the rods in relation to the assembly lower tie plate, and the nominal (core average) coolant temperature along the rods. The traces of Rods 1 and 3 and of Rods 2 and 4 have been combined in single plots because these pairs of rods have identical cladding and exposure times. The average oxide thickness in the fuel rod plenum areas, the areas where a rod passes through spacers, and the maximum oxide thickness in each span (region between spacers) are listed in Table 5.

Table 5 Average Oxide Thickness at Selected Locations

	Oxide Thickness, μm			
	Through-Wall Zry-4		Zr Liner-Zircaloy-4	
Location*	End of Cycle 4	End of Cycle 5	End of Cycle 4	End of Cycle 5
Plenum 4	6	12	---	---
Plenum 6	11	16	8	12
Spacer 4	10	15	---	---
Spacer 5	12	17	12	16
Spacer 6	14	19	13	17
Span 3	18	42	---	---
Span 5	38	40	17	23

* See Figures 1 and 2 for plenum, spacer, and span locations.

As indicated in Table 5, the measurements show that with increasing height in the assembly, and hence increasing coolant and cladding temperature, the oxide thickness in spacer areas increases by approximately 2 microns per span for the through-wall Zircaloy-4 cladding and approximately 1 micron per span for the liner cladding in both the four and five cycle rods. For the plenum areas of Zircaloy-4 cladding, the increase is 4 to 5 microns per rodlet length. There are no comparable plenum area data for rods with liner cladding.

Observed increases in oxide thickness with increasing cladding temperatures are in fair agreement with an activation temperature of 14,080 K for in-reactor Zircaloy-4 corrosion as given in MATPRO.[1] Depending on the initial oxide thickness in a given spacer area, increases of 1.7 to 2.5 microns between Spacers 4 and 5 and of 1.9 to 2.8 microns between Spacers 5 and 6 are calculated. The calculated increase of the oxide thickness in the plenum areas between lower and upper rods is 2.5 microns for four-cycle and 3.8 microns for five-cycle rods.

The corrosion rate of the through-wall cladding appears to be higher than the corrosion rate of the liner cladding. This is most clearly observed in the non-heat transfer plenum area, where there is no thermal feedback effect that could account for the differences in oxide thickness after four and after five cycles.

From End of Cycle (EOC) 4 to EOC 5 (i.e., during Cycle 5), the oxide thickness in the plenum areas and in the spacer areas increased approximately 4 to 6 microns. This is slightly higher than would be indicated by a post-transition corrosion rate that is linear with time. This indicates that there may have been an increase in the corrosion rate in the plenum areas (non-heat transfer surface) and the spacer regions during the last irradiation cycle.

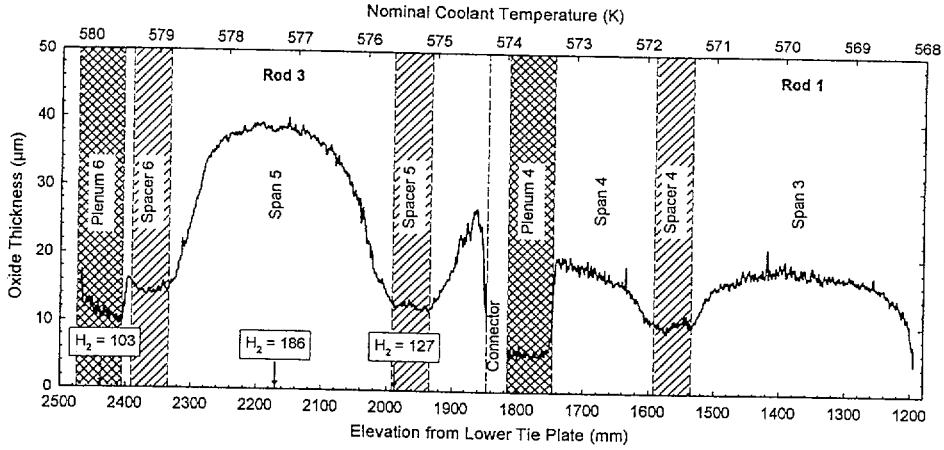

Rods No. 1 and 3, Through-Wall Zircaloy-4 Cladding, Four Cycles of Irradiation

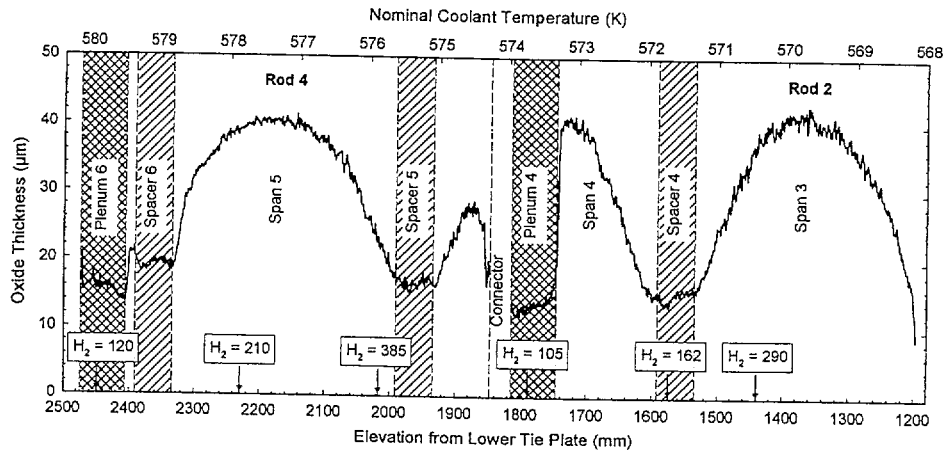

Rods No. 2 and 4, Through-Wall Zircaloy-4 Cladding, Five Cycles of Irradiation

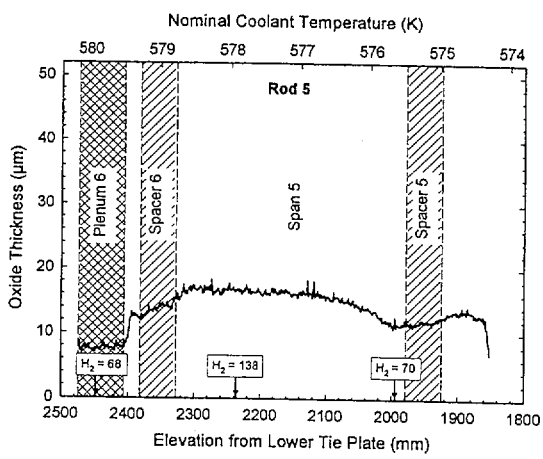

Rod No. 5, Liner Zircaloy-4 Cladding,
Four Cycles of Irradiation

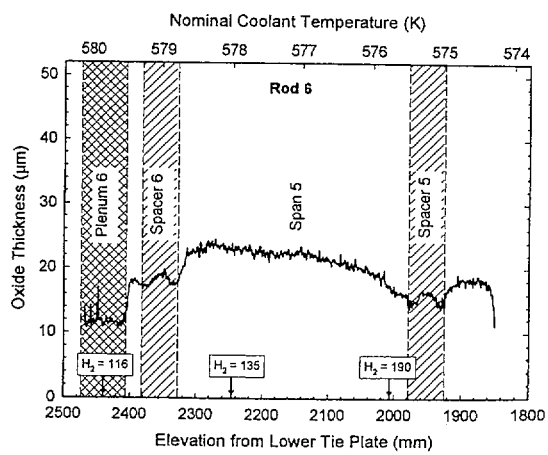

Rod No. 6, Liner Zircaloy-4 Cladding,
Five Cycles of Irradiation

Figure 2 Oxide Thickness Profiles (Circumferential Average) of Four-Cycle and Five-Cycle Rods with Through-Wall and Liner Zircaloy-4 Cladding. Hydrogen concentrations at the positions indicated are ppm values.

The behavior of the cladding in the fueled sections outside the spacer areas depends on power history, which affects the cladding temperature, and cladding type. The through-wall Zircaloy-4 cladding had a larger oxide thickness accumulation at an equivalent in-reactor residence time than the Zircaloy-4 liner cladding. This is readily observed by comparing the oxide thickness of Rod 3 to Rod 5 (four cycles of irradiation, same axial location) and of Rod 4 to Rod 6 (five cycles each). This comparison is shown in Figures 3a and 3b. In both cases, the rods with the through-wall Zircaloy-4 cladding show significant corrosion whereas the liner cladding has much lower corrosion. A comparison of the oxide thickness of Rod 1 and Rod 2 (Figure 3c) indicates that for a lower segment with through-wall Zircaloy-4 cladding, a large part of the oxide growth occurred during the fifth cycle.

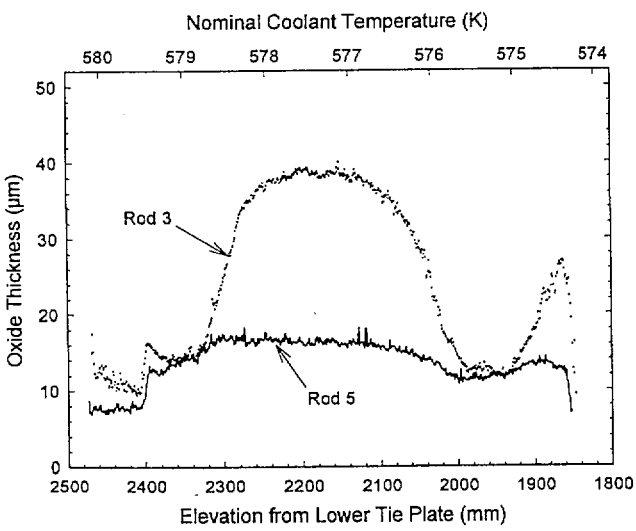

Figure 3a Oxide Thickness Profiles of Four-Cycle Rods 3 and 5 with Through-Wall (Rod 3) and Liner (Rod 5) Zircaloy-4 Cladding

Figure 3d compares the corrosion profiles of Rod 3 (four-cycle through-wall cladding) and Rod 6 (five-cycle liner cladding). In the plenum and spacer areas, the oxide thickness of the four-cycle through-wall cladding is, as expected, less than that of the five-cycle liner cladding. In the main span of the rod, however, the corrosion of the through-wall cladding is much higher than that of the liner cladding. This indicates that the corrosion rate of the through-wall cladding has accelerated whereas the corrosion rate of the liner cladding has remained constant or increased only slightly.

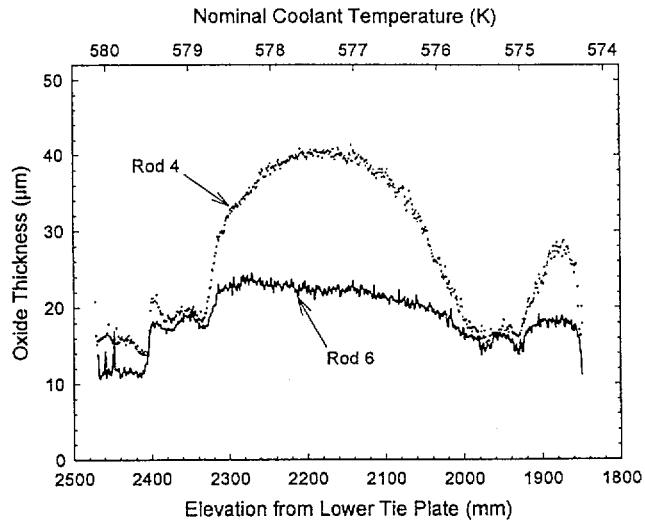

Figure 3b Oxide Thickness Profiles of Five-Cycle Rods 4 and 6 with Through-Wall (Rod 4) and Liner (Rod 6) Zircaloy-4 Cladding

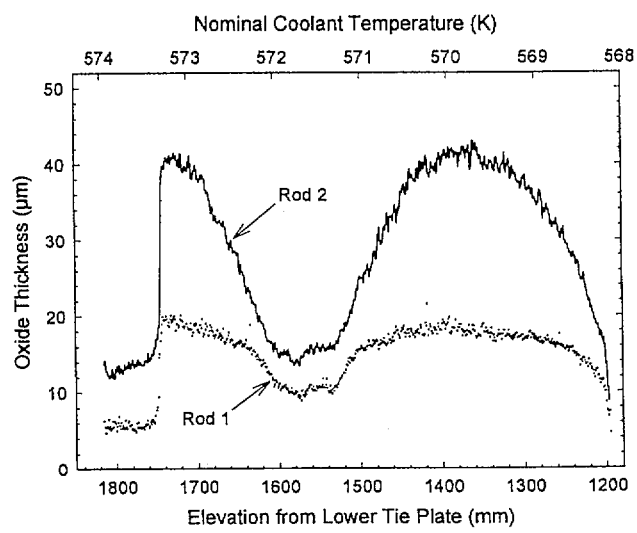

Figure 3c Oxide Thickness Profiles of Four-Cycle Rod 1 and Five-Cycle Rod 2 with Through-Wall Zircaloy-4 Cladding

In summary, it may be stated that the initial corrosion rate of the through-wall cladding appears to be higher than that of the liner cladding and that the through-wall cladding appears to be much more susceptible to accelerated corrosion at high burnup than the liner cladding. The acceleration seems to be influenced by temperature, occurring earlier and being more pronounced at higher temperature. The root cause of this difference in behavior has not been fully determined. Small differences in composition (silicon content), fabrication processes, or

differences in hydrogen pick-up and hydride distribution (see also below) could be possible causes.

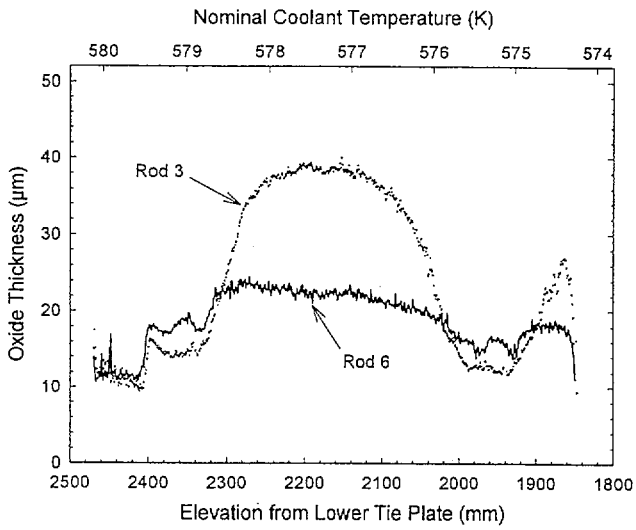

Figure 3d Oxide Thickness Profiles of Four-Cycle Rod 3 and Five-Cycle Rod 6 with Through-Wall (Rod 3) and Liner (Rod 6) Zircaloy-4 Cladding

B. Profilometry

Poolside measurements indicated that the fuel rods attained their maximum creepdown during the fourth cycle of irradiation. The amount of creepdown depended on the initial fuel-to-cladding gap size, rods with the largest gap showing the largest creepdown. Creepdown data, corrected for oxide accumulation, are shown in Figure 4. There was no noticeable difference in the creepdown behavior between rods with through-wall Zircaloy-4 cladding and rods with liner cladding. During the fifth cycle of irradiation, all rod diameters, regardless of initial gap size, increased by approximately 0.15%, indicating fuel-to-cladding contact during the last cycle and fuel pellet swelling of approximately 0.5 volume percent per 10 MWd/kgU burnup.

Six axial profilometry scans, each 30 degrees apart, were made in the hot cells on each of the six segmented rods listed in Table 4. Rod average diameter, rod ovality, and clad ridging were determined from the scans. All profilometry data were corrected for oxide accumulation. Figure 5 shows the rod average diameter before and after correction for oxide thickness. Uniform creepdown and a uniform diameter along the rod length are expected, since the fast fluence and pellet swelling along the length of the rod are close to uniform.

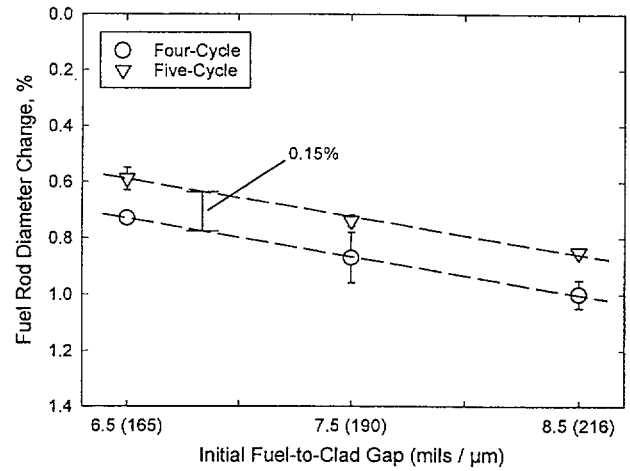

Figure 4 Fuel Rod Diameter Change from Beginning-of-Life Diameter as a Function of Initial Pellet-to-Cladding Gap Size

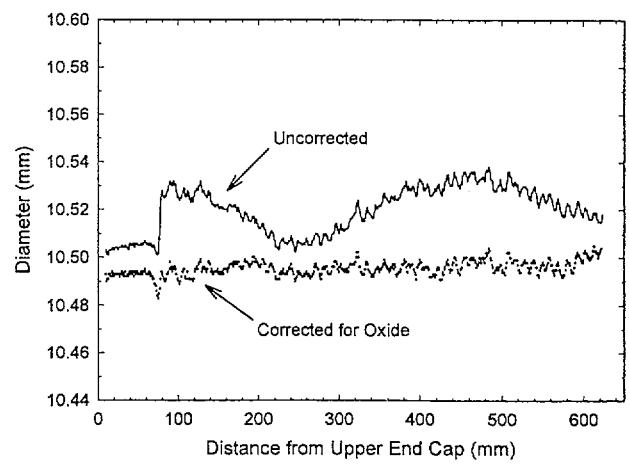

Figure 5 Diameter Profile of Rod 2 Before and After Correction for Oxide Accumulation

A Pilling-Bedworth factor of 1.75 was used to correct for oxide thickness accumulation; this resulted in uniform diameter profiles for all the rods measured. It indicates that the bulk oxide is approximately 89-90% dense. Metallographic observations also indicate that the oxide of the fuel rod cladding is not fully dense.

Figure 6 compares the oxide-thickness-corrected diameter traces of Rods 1 and 2. Whereas the cladding continues to creep down in the plenum area, the rod diameter has increased (outward creep) in the fueled section of the rod during the fifth (final) irradiation cycle. This was observed for other pairs of rods as well and

agrees with the findings from the poolside examination. The outward creep is due to fuel pellet swelling.

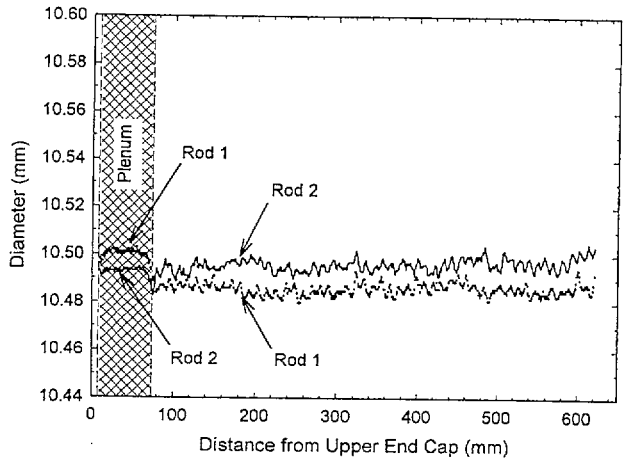

Figure 6 Diameter Profile of Four-Cycle Rod 1 Compared to Profile of Five-Cycle Rod 2. During Cycle 5, there was continued creepdown in the plenum area, whereas pellet swelling caused a diameter increase in the fueled section of the rod.

At 22 microns, cladding ovality (half the difference between smallest and largest diameter measured at any axial location) in the plenum area was typically much higher than in the fueled sections of the rods, where the cladding is supported by the fuel pellets, and where ovality averaged 5 microns.

Ridge height, at 2 to 3 microns, was small in all rods. There was no difference in ridge height between rods with solid pellets and rods with annular pellets. The presence of ridges is another indication of pellet-to-cladding contact.

C. Hydrogen Pick-up

The hydrogen concentration of the cladding was determined by vacuum extraction in the plenum region, the fuel region (at highest oxide thickness), and in the spacer region of the fuel rods. The data are shown in Figure 3 and are tabulated in Table 6. The hydrogen concentration reported includes the initial hydrogen level of the cladding, which was 10 to 15 ppm. Hydrogen pick-up ratios were calculated, taking into account the initial hydrogen level of the cladding. In the calculations, a Pilling-Bedworth ratio of 1.75 is assumed. The hydrogen pick-up fractions are given in Table 6. The pick-up ratio is plotted as a function of oxide thickness in Figure 7. No systematic differences between the pick-up ratios in different regions of the fuel rods (plenum region, spacer region, span region) were noted, nor were there significant differences between the through-wall Zircaloy-4 and the liner Zircaloy-4 cladding. At lower oxide thickness values, the pick-up ratio was higher than at higher oxide thickness values. The very high value observed near one of the spacer regions (Rod 4) may be due to a faulty measurement (perhaps moisture in the oxide) or could be due to migration of hydrogen to the cooler spacer region. The latter would result in a high apparent pick-up ratio.

Table 6 Hydrogen Concentration and Pick-up Fraction

	Hydrogen Concentration* (ppm)			Pick-up Fraction**		
Rod	Plenum	Spacer	Span	Plenum	Spacer	Span
2	105	162	290	0.213	0.275	0.181
3	103	127	186	0.230	0.244	0.125
4	120	385	210	0.185	0.512	0.135
5	68	70	138	0.198	0.137	0.207
6	116	190	135	0.243	0.310	0.149

* Includes 10-15 ppm hydrogen initially present in the cladding.

** Corrected for initial hydrogen in the cladding; assumes Pilling-Bedworth ratio of 1.75.

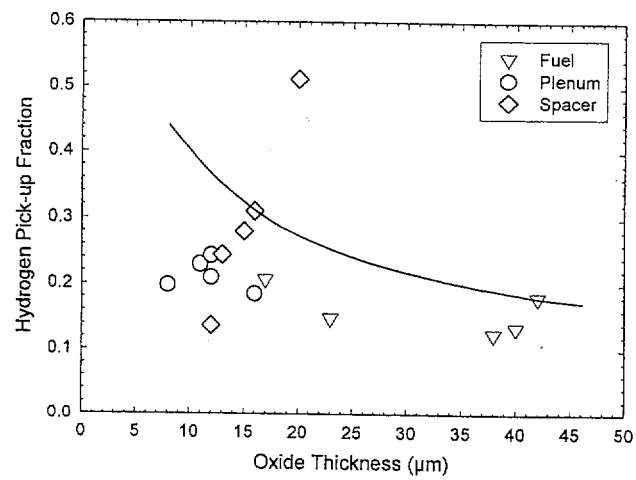

Figure 7 Hydrogen Pick-up Fraction as a Function of Oxide Thickness

D. Hydrogen/Hydride Distribution

Fuel rods were sectioned in the transverse and longitudinal directions. Metallographic specimens were polished and etched to reveal the zirconium hydrides. Representative photographs are shown in Figure 8.

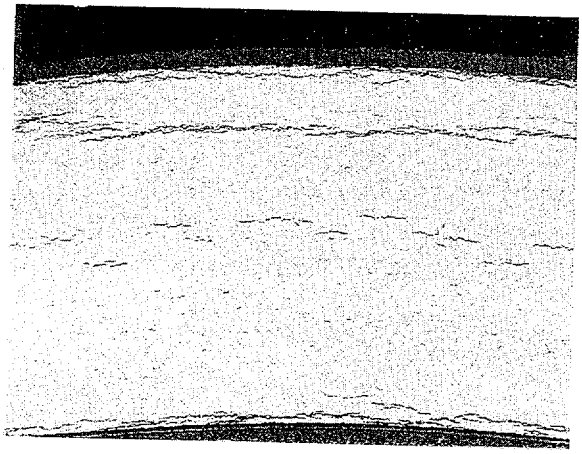

8a Through-Wall Zircaloy-4 Cladding (100X)

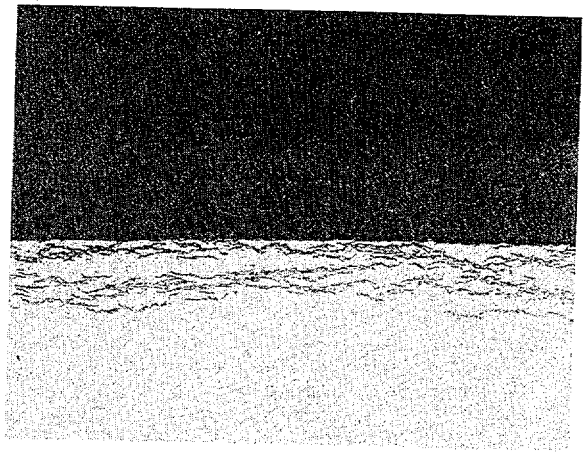

8b Outside Surface of Through-Wall Zircaloy-4 Cladding; Oxide Thickness: 42 μm (500X)

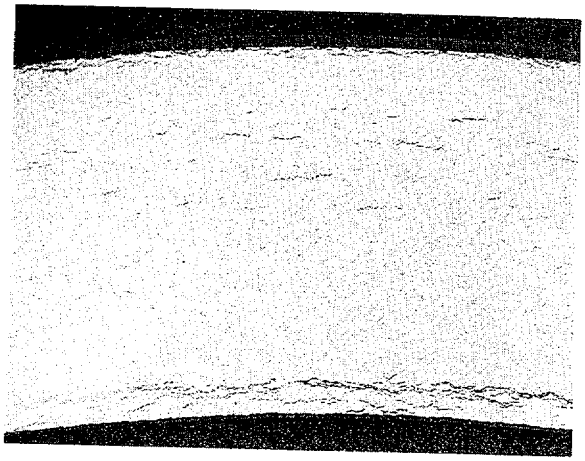

8c Zirconium Liner-Zircaloy-4 Cladding (100X)

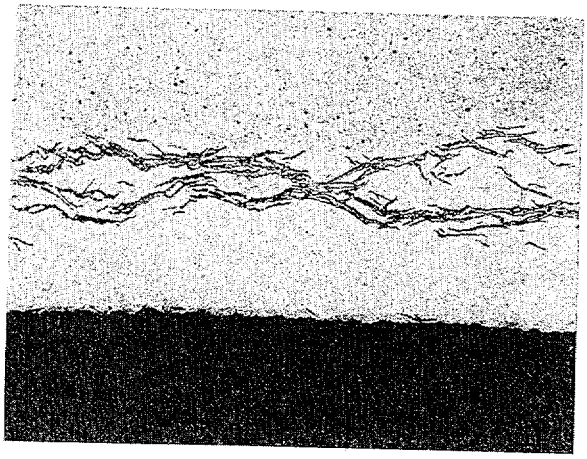

8d Inside Surface of Liner Zircaloy-4 Cladding; Liner Thickness: ~75 μm (500X)

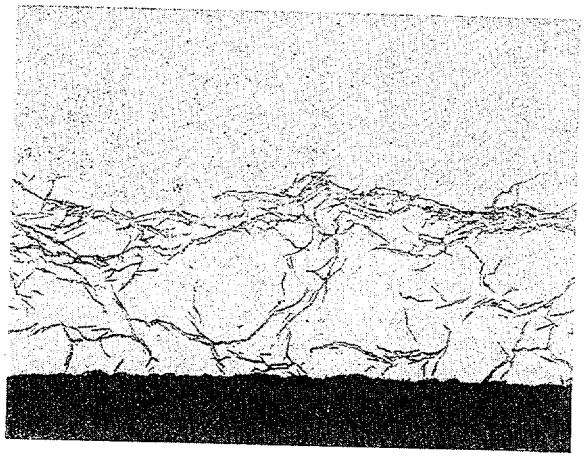

8e Inside Surface of Liner Zircaloy-4 Cladding; (500X)

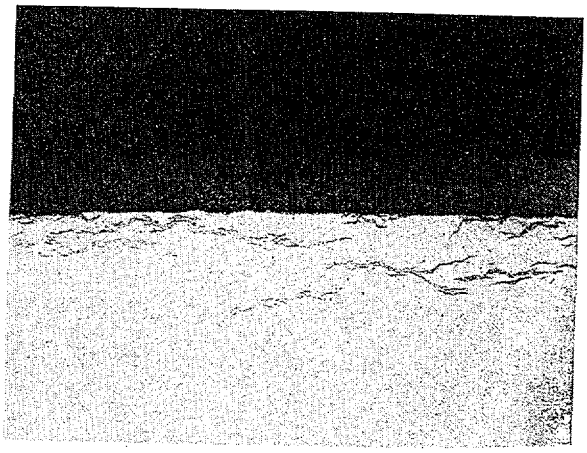

8f Outside Surface of Liner Zircaloy-4 Cladding; Oxide Thickness: 23 μm (500X)

Figure 8 Distribution of Hydrides in Zircaloy-4 and Zirconium Liner-Zircaloy-4 Cladding after Five Cycles of Irradiation

The hydride platelets are oriented in the tangential (and axial) direction of the cladding. This is shown for five-cycle through-wall cladding in Figure 8a. Figure 8b, at higher magnification, shows the hydrides in the vicinity of the cladding OD, where the hydride concentration is highest. Few of the hydrides are at the surface of the metal or appear to penetrate the surface. It appears unlikely that zirconium hydride near the cladding OD (shown in Figure 8b) could have been the cause of accelerated corrosion as observed in this specimen (oxide thickness 42 microns). Figures 8c through 8f show the distribution of hydrides in five-cycle irradiated liner cladding. The bulk of the Zircaloy-4 part of the liner cladding contains few hydrides. The total amount of hydrogen in the sample is approximately 135 ppm. In the liner cladding, the bulk of the hydrides precipitated in the zirconium liner close to, but not at, the interface with the Zircaloy. This is clearly shown in Figure 8d. In some cases, hydrides are present throughout the liner material and close to the ID. of the cladding. A representative view is shown in Figure 8e. There is a small concentration of hydride near the cladding OD, as shown in Figure 8f. These hydrides precipitated during fuel rod cool down.

The precipitation of hydrides in a temperature gradient in a cladding tube of uniform composition has been described by, among others, Asher and Trowse.[2] The zirconium hydrides precipitate preferentially near the relatively cooler cladding OD. At this location the concentration of hydrogen in solution is highest and the terminal solid solubility (t.s.s.) of hydrogen is lowest. Hydrides may precipitate at other locations away from the cladding OD due to other favorable conditions for precipitation.

The presence of zirconium liner at the cladding ID modifies the distribution of hydrogen and hydrides. The solubility of hydrogen in the lower-oxygen (400-600 ppm) zirconium liner is less than that in the higher-oxygen (1000-1400 ppm) Zircaloy.[3,4] At the prevailing temperatures and the small difference in oxygen concentration between Zircaloy-4 and liner, the difference is not large. The lower oxygen level in the liner compared to Zircaloy affects the terminal solid solubility more strongly. The terminal solid solubility of hydrogen in zirconium in Zircaloy-4 has recently been determined by Kodama and Anada[4] and earlier by Erickson and Hardie.[5] Kodama et al. found that upon cooling hydrogen-charged samples, when non-equilibrium gamma-phase hydride is formed, the t.s.s. in zirconium is lower than the t.s.s. in Zircaloy. At a temperature of approximately 350°C this difference is some 100 ppm. Upon heating, and the formation of stable delta-phase, the difference is smaller, probably on the order of 50 ppm at a temperature of approximately 350°C. This is also the temperature of the Zircaloy-zirconium interface temperature at an LHGR of approximately 6 kW/ft (~200 W/cm). At modest heat ratings, and hence moderate temperature gradients through the cladding wall thickness, zirconium hydride precipitates would, therefore, be expected to form in the liner near the Zircaloy-zirconium interface. This was observed in the fuel cladding examined here, and is schematically indicated in Figure 9a. At much higher heat ratings, and steeper temperature gradients, hydrides would be expected to precipitate near the cladding OD as is normally observed in single-composition through-wall cladding, and as indicated in Figure 9b.

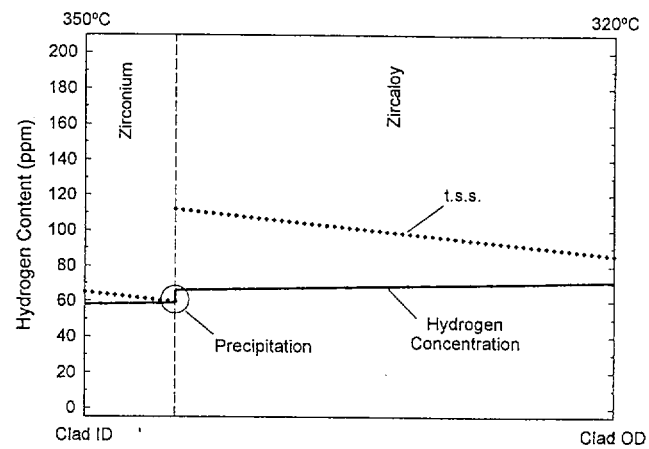

Figure 9a Schematic Illustration of Hydride Precipitation in the Liner at Moderate Heat Rating

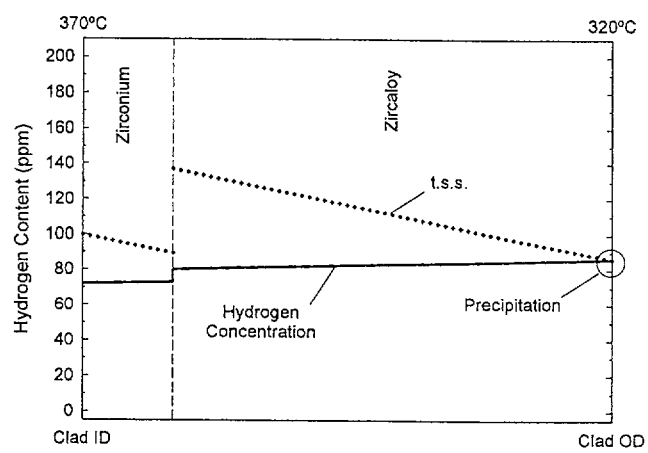

Figure 9b Schematic Illustration of Hydride Precipitation Near the Cladding OD at High Heat Rating and a Steep Temperature Gradient in the Cladding

The formation of a high concentration of hydrides in the liner could be expected to affect the effectiveness of the liner in preventing PCI failures. The tendency of hydrides to form in the liner rather than in the Zircaloy

part of the cladding may also play a role in secondary failure mechanisms and the formation of long cladding splits. The formation of hydrides near the cladding ID would, due to the volume increase, set up a tangential stress in the Zircaloy part of the cladding, which could lead to or aid in the formation of cracks.

E. Tensile Tests

Tensile tests at room temperature (RT) and at 350°C were performed on 5 mm wide rings cut from the plenum and fueled sections of the fuel rods. D-shaped specimen "grips" were used to load the rings in the circumferential direction. Due to the specimen width (5 mm) to gage length (~1-2 mm) ratio, quasi-plane strain conditions prevailed in the test section.

Unirradiated ring type specimens and conventional hourglass specimens (axial direction) were tested at room temperature. The values for ultimate tensile strength (u.t.s), uniform elongation (ε_u), and total elongation (ε_t) for the two types of specimens were compared. Hourglass specimens showed a higher u.t.s value (740 compared to 685 MPa) and a higher ε_u value (8% compared to approximately 4-6%) than the ring specimens. ε_t was approximately the same for both types of specimens. These differences are mainly due to the different test direction (axial versus circumferential) and the effects of texture.

Table 7 provides an overview of the data obtained along with a listing of the specimen oxide thickness and approximate hydrogen content. The difference in u.t.s. between through-wall cladding and liner cladding, which was approximately 50 MPa in the unirradiated condition of both RT and 350°C, was maintained for specimens from the plenum sections (low hydrogen concentration) of the rods but was largely absent for specimens from the fueled sections (higher hydrogen concentration in the through-wall cladding).

At room temperature, the u.t.s. increased by 180-200 MPa for four-cycle rods and 220-250 MPa for five-cycle rods for both types of cladding. At 350°C, the u.t.s. increased approximately 200-230 MPa for both four- and five-cycle rods of both cladding types. These increases appear to be mainly the result of irradiation hardening.

Table 7 Results of Ring Tensile Tests

Clad Type	Fluence 10^{25} n/m^2 E>1 MeV	Oxide µm	H_2 ppm	Room Temperature u.t.s.	ε_u	ε_t	350°C u.t.s.	ε_u	ε_t
Zry-4	0	0	11	710	5	25	417	4.5	24
Liner	0	0	13	660	4	27	376	4.5	30
Zry-4	7	14	104	910	1.5	1.5	666	4	21
Zry-4	7	36	186	883	2	2	611	4	5
Liner	7	7	68	857	5	15	591	4	19
Liner	7	16	138	840	6	12	586	4	19
Zry-4	8.9	13	105	956	4	6	652	4	17
Zry-4	8.9	40	290	775*	2	2	602	3	8
Liner	8.9	11	116	911	4	10	614	4	18
Liner	8.9	22	135	878	5	12	598	4	19

* Fractured before u.t.s. was reached.

Uniform elongation (plastic deformation at maximum specimen load) was affected by irradiation and hydrogen pick-up, but the effects appeared to be relatively small. At room temperature, it remained constant at about 5% (before and after irradiation) for the liner cladding (bulk of cladding free of hydrides) and was reduced from 5% to 2-4% for the through-wall cladding. At 350°C, the uniform elongation of all specimens went from 4.5% before irradiation to 4% after irradiation.

The most notable differences were observed in the values for total elongation. For through-wall cladding with high concentrations of hydrides, the total elongation decreased from 25% before irradiation to 2-4% after irradiation when tested at RT, and from 24% to 5-8% when tested at 350°C. At low hydrogen values the decrease in total elongation, when tested at 350°C, was much less pronounced: 24% before irradiation compared to 17-21% after irradiation. For liner cladding specimens with an absence of hydrides in the Zircaloy-4 part of the cladding, total elongation reductions were much smaller than those observed for through-wall cladding with hydrides. At RT, total elongation in the liner specimens was still 10-15% (27% before irradiation). At 350°C, the total elongation was 18-19% for the irradiated material, compared to 30% for the unirradiated cladding.

In summary, it may be concluded that the u.t.s. of the stress-relieved cladding, when tested in the circumferential direction, is increased mainly due to irradiation hardening; the total elongation, as measured in the ring type specimens, is decreased mainly due to the presence of hydrides. The uniform elongation was not strongly affected by either irradiation or hydrides.

V. CONCLUSIONS

Poolside and hot cell examinations of through-wall 1.5% Sn Zircaloy-4 cladding and zirconium liner-Zircaloy-4 cladding have led to the following conclusions:

The initial corrosion rate of the through-wall Zircaloy-4 cladding (~1.5% Sn) irradiated during the program appears to be higher than the corrosion rate of liner Zircaloy-4 cladding. The through-wall cladding also appears to be more susceptible to accelerated corrosion at high burnup than the liner cladding. Small differences in composition and/or fabrication processing or differences in hydrogen pick-up and hydride distribution could be possible causes.

The density of the oxide formed on the fuel rod cladding is approximately 89-90% of the theoretical density of zirconium oxide.

Hydrogen pick-up ratios for both types of cladding were similar. The pick-up ratio is found to be higher at low oxide thickness and approaches approximately 15% at an oxide thickness of 50 microns.

Hydrides preferentially precipitate near the cooler cladding outside surface in single-composition through-wall Zircaloy-4 cladding. In the pure zirconium liner-Zircaloy-4 cladding, hydrides accumulate in the liner.

The tensile strength of fuel rod cladding is increased due to irradiation, and total elongation at fracture is decreased, mainly due to hydrides that are present in the matrix. The uniform elongation was not as strongly affected by irradiation and hydride precipitation as the total elongation. The liner cladding maintained a high degree of ductility at room temperature due to the absence of hydrides in the Zircaloy-4 part of the cladding.

ACKNOWLEDGMENTS

The authors are grateful to ESEERCo, RG&E, and Siemens for permission to publish this paper. They are also indebted to Mr. C. Lemaignan and Mr. R. Gillet of the CEA laboratories in Grenoble, France for ably guiding all hot cell activities and to the hot cell laboratory personnel for performing the examinations.

REFERENCES

1. SCDAP/RELAPS/MOD 3.1 Code Manual Volume IV: MATPRO, P. T. Hagrman, editor, NUREG/CR-6150, EGG-2720.

2. R. C. Asher and F. W. Trowse, "The Distribution of Hydrogen in Zirconium Alloy Fuel Cladding: The Effects of Heat Flux," *Journal of Nuclear Materials*, 35 (1970), p. 115-121.

3. S. Yamanaka, T. Tanaka, M. Miyake, "Effect of Oxygen on Hydrogen Solubility in Zirconium," *Journal of Nuclear Materials*, 167 (1989), p. 231-237.

4. T. Kodama, H. Anada, "Study of Inhomogeneous Distribution of Hydrides in Zirc Liner Tubing," *Japanese Nuclear Society Proceedings*, October 23-26, 1984.

5. W. H Erickson and D. Hardie, "The Influence of Allowing Elements of the Terminal Solubility of Hydrogen in α-Zirconium," *Journal of Nuclear Materials*, 13 No. 2 (1964), p. 254.

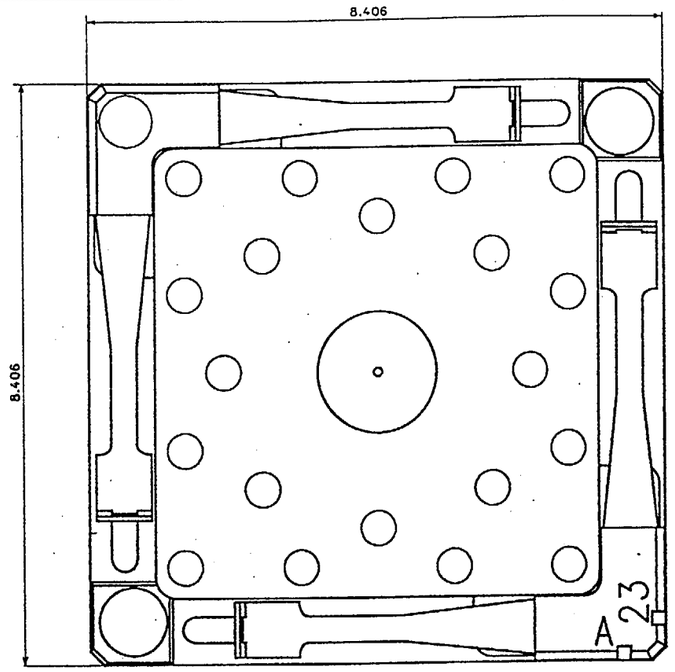

A SH 1

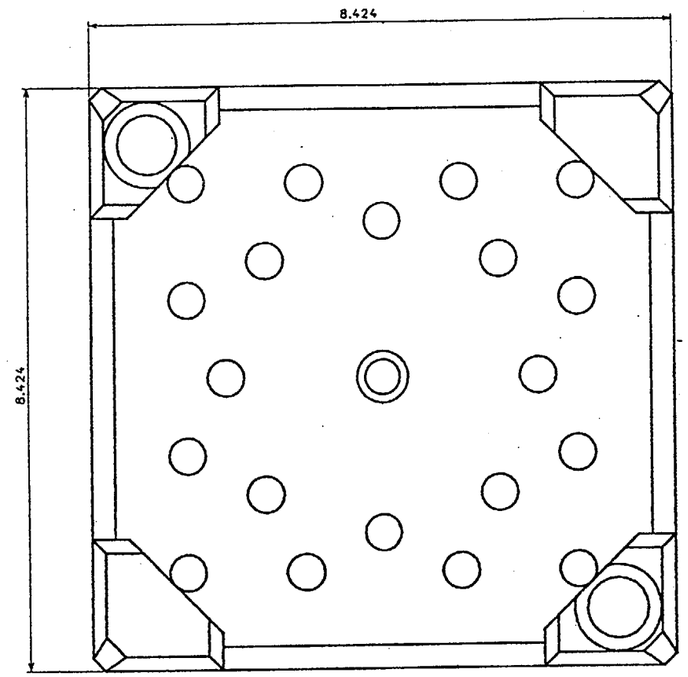

C SH 1

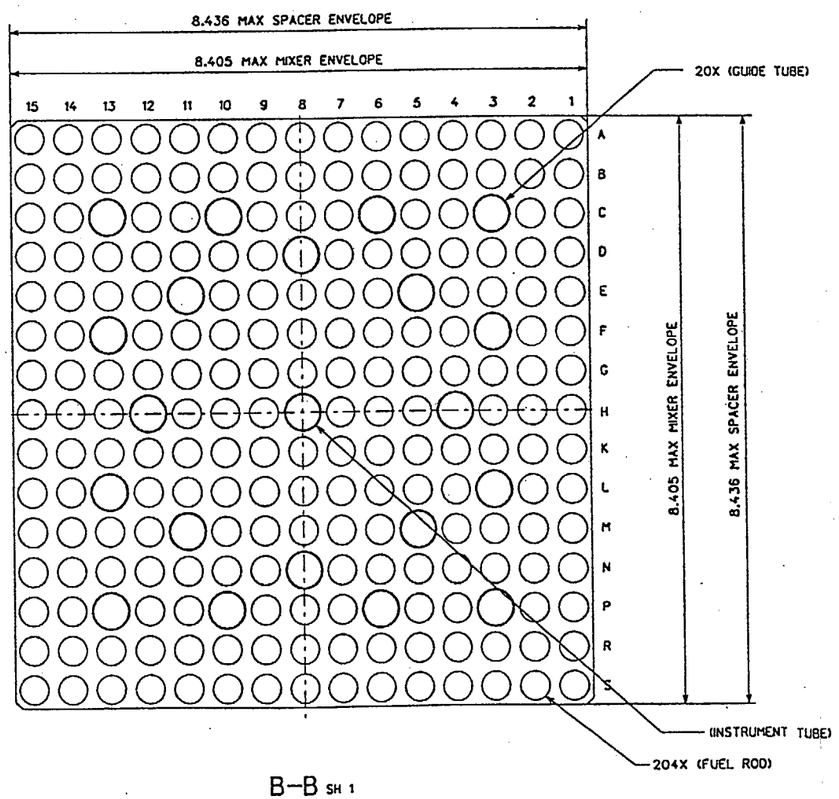

B–B SH 1

FOR GENERAL NOTES SEE SHEET 1

VIEW ORIENTATION
3RD ANGLE PROJECTION

INTERGRAPH (CADD)

Siemens Power Corporation – ND

SCALE: 1 : 1

Information herein is proprietary to the corporations listed above. It is tol submitted in confidence; tbl not to be reproduced or disclosed or used other than for the purpose for which it is furnished without the written authorization of the corporations and tol to be returned upon request.

	DATE	NAME
DRAWN BY	7-23-96	CLS
CHECKED BY		
APPROVED		
APPROVED		
APPROVED		

TITLE

FUEL BUNDLE ASSEMBLY

DRAWING NO. SK-EMF-303,260 R-1

SH NO. 2 SHEETS 2

APPROVED	REV	REVISIONS

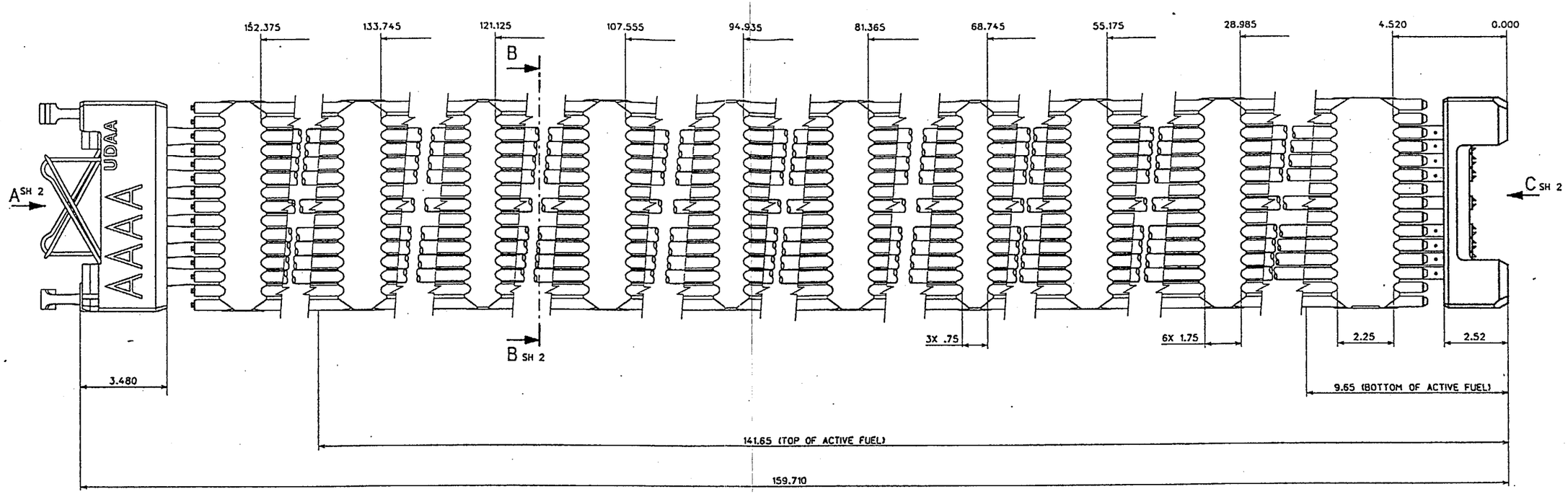

General Notes: UNLESS OTHERWISE SPECIFIED

1. DIMENSIONING AND TOLERANCING PER ISO 1101. ALL DIMENSIONS ARE IN INCHES.
2. ASSEMBLY WEIGHT APPROXIMATELY 1440 LBS.
3. THE NOTED SPACER LOCATIONS AND HEIGHTS REFLECT THE INTERNAL GRID RATHER THAN THE OUTER STRAP.

VIEW ORIENTATION
3RD ANGLE PROJECTION

APPROVED	REV	REVISIONS

INTERGRAPH (CADD)

Siemens Power Corporation – ND

SCALE: 1:2

Information herein is proprietary to the corporations listed above. It is (a) submitted in confidence; (b) not to be reproduced or disclosed or used other than for the purpose for which it is furnished without the written authorization of the corporations; and (c) to be returned upon request.

	DATE	NAME
DRAWN BY	7-23-96	CLS
CHECKED BY		
APPROVED		
APPROVED		
APPROVED		

TITLE

FUEL BUNDLE ASSEMBLY

DRAWING NO. SK-EMF-303,260 R-1

SH NO. 1 SHEETS 2

ATTACHMENT 2
AFFIDAVITS

AFFIDAVIT

STATE OF WASHINGTON)
) ss.
COUNTY OF BENTON)

1. My name is Jerald S. Holm. I am Manager, Product Licensing, for Framatome ANP ("FRA-ANP"), and as such I am authorized to execute this Affidavit.

2. I am familiar with the criteria applied by FRA-ANP to determine whether certain FRA-ANP information is proprietary. I am familiar with the policies established by FRA-ANP to ensure the proper application of these criteria.

3. I am familiar with the FRA-ANP information contained in the attachment to the letter VNG:00:294, dated October 31, 2000, and referred to herein as "Document." Information contained in this Document has been classified by FRA-ANP as proprietary in accordance with the policies established by FRA-ANP for the control and protection of proprietary and confidential information.

4. This Document contains information of a proprietary and confidential nature and is of the type customarily held in confidence by FRA-ANP and not made available to the public. Based on my experience, I am aware that other companies regard information of the kind contained in this Document as proprietary and confidential.

5. This Document has been made available to the U.S. Nuclear Regulatory Commission in confidence with the request that the information contained in the Document be withheld from public disclosure.

6. The following criteria are customarily applied by FRA-ANP to determine whether information should be classified as proprietary:

(a) The information reveals details of FRA-ANP's research and development plans and programs or their results.

(b) Use of the information by a competitor would permit the competitor to significantly reduce its expenditures, in time or resources, to design, produce, or market a similar product or service.

(c) The information includes test data or analytical techniques concerning a process, methodology, or component, the application of which results in a competitive advantage for FRA-ANP.

(d) The information reveals certain distinguishing aspects of a process, methodology, or component, the exclusive use of which provides a competitive advantage for FRA-ANP in product optimization or marketability.

(e) The information is vital to a competitive advantage held by FRA-ANP, would be helpful to competitors to FRA-ANP, and would likely cause substantial harm to the competitive position of FRA-ANP.

7. In accordance with FRA-ANP's policies governing the protection and control of information, proprietary information contained in this Document has been made available, on a limited basis, to others outside FRA-ANP only as required and under suitable agreement providing for nondisclosure and limited use of the information.

8. FRA-ANP policy requires that proprietary information be kept in a secured file or area and distributed on a need-to-know basis.

9. The foregoing statements are true and correct to the best of my knowledge, information, and belief.

SUBSCRIBED before me this 13th day of August, 2001.

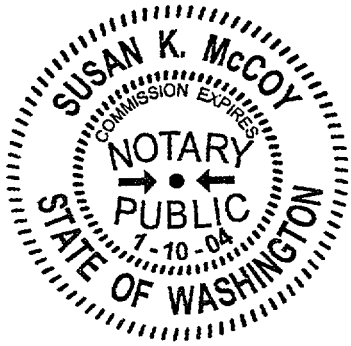

Susan K. McCoy
NOTARY PUBLIC, STATE OF WASHINGTON
MY COMMISSION EXPIRES: 1/10/04